Controlling Light-Matter Interaction in Semiconductors with Hybrid Nano-Structures

by
Michael R. Gehl

A Dissertation Submitted to the Faculty of the

College of Optical Sciences

In Partial Fulfillment of the Requirements
For the Degree of

Doctor of Philosophy

In the Graduate College

The University of Arizona

2 0 1 5

The University of Arizona
Graduate College

As members of the dissertation committee, we certify that we have read the dissertation prepared by Michael R. Gehl entitled:

Controlling Light-Matter Interaction in Semiconductors with Hybrid Nano-Structures

and recommend that it be accepted as fulfilling the dissertation requirement for the degree of Doctor of Philosophy.

	9/25/2015
Galina Khitrova	Date
	9/25/2015
Brian Anderson	Date
	9/25/2015
Khanh Kieu	Date

Final approval and acceptance of this dissertation is contingent upon the candidate's submission of the final copies of the dissertation to the Graduate College.

I hereby certify that I have read this dissertation prepared under my direction and recommend that it be accepted as fulfilling the dissertation requirement.

	9/25/2015
Dissertation Director: Galina Khitrova	Date

Statement by Author

This dissertation has been submitted in partial fulfillment of the requirements for an advanced degree at the University of Arizona and is deposited in the University Library to be made available to borrowers under rules of the Library.

Brief quotations from this dissertation are allowable without special permission, provided that accurate acknowledgment of source is made. Requests for permission for extended quotation from or reproduction of this manuscript in whole or in part may be granted by the head of the major department or the Dean of the Graduate College when in his or her judgment the proposed use of the material is in the interests of scholarship. In all other instances, however, permission must be obtained from the author.

SIGNED: Michael Gehl

_____

Acknowledgments

First and foremost I would like to express my gratitude to my adviser Galina Khitrova for her guidance and support. Being a part of her research group has provided me with amazing opportunities. Not only have I had the freedom to explore fundamental quantum optics but I've also been able to present at prominent scientific conferences and travel to work with other leading research groups. I'd also like to acknowledge Hyatt Gibbs. Although I only had the opportunity to work with him for a few years he had a big impact on me. I will never forget learning MBE growth with Hyatt & Galina and the "Herd".

I'd like to thank Prof. Martin Wegener and Muriel Béchu for the opportunity to work with their group at Karlsruhe Institute of Technology. Their guidance and training in nanofabrication was invaluable to completing my research. This work would have been impossible if not for Prof. Wegener's trusting me with his electron beam lithography system.

I'd also like to thank Dr. Alexandre Arnoult for hosting me in his lab at the Laboratory for Analysis and Architecture of Systems – CNRS in Toulouse, France. It was a great joy to work with state-of-the-art molecular beam epitaxy equipment and learn techniques from an expert in the field. The ability to perform high-resolution X-Ray diffraction was a life-saver when we ran into trouble with our semiconductor growth.

During my graduate studies I have been afforded many opportunities as a result of my involvement with the NSF Center for Integrated Access Networks (CIAN). I have been able to interact with students and industry members from across the country and internationally.

I'd like to thank the members of my defense committee, Brian Anderson and Khanh Kieu. They have been excellent educators and mentors and I appreciate their support of my dissertation.

None of this research would have been possible without the help of my fellow students, Ricky Gibson, Sander Zandbergen, Jasmine Sears and Patrick Keiffer. Coming into the research group I received excellent training from the senior students, Joshua Hendrickson, Ben Richards, Julian Sweet and JD Olitzky. It's also been a pleasure to continue collaborating with Joshua Hendrickson since his graduation.

Last but not least, I'd like to thank my family for their love and support throughout. My parents, John & Linda, George & Elly, my siblings, Jenna & Brad, Sherry & Robert, Stacey & Corey, Scott & Becky, Carrie, Nicole & Andrew, and my fiancé Amanda.

Dedication

To my sister, Jenna Gehl-Jones, for her advice and never-ending patience.

To my beautiful fiancé, Amanda Dudek, for her unconditional love and support.

Table of Contents

Table of Contents—*Continued*

List of Figures

List of Figures—*Continued*

List of Figures—*Continued*

List of Tables

List of Publications

B. C. Richards, J. Hendrickson, J. D. Olitzky, R. Gibson, M. Gehl, K. Kieu, U. K. Khankhoje, A. Homyk, A. Scherer, J.-Y. Kim, Y.-H. Lee, G. Khitrova, and H. M. Gibbs, "Characterization of 1D photonic crystal nanobeam cavities using curved microfiber," *Optics Express*, vol. 18, no. 20, pp. 20558-20564, 2010.

J. Hendrickson, M. Helfrich, M. Gehl, D. Hu, D. Schaadt, S. Linden, M. Wegener, B. Richards, H. M. Gibbs, and G. Khitrova, "InAs quantum dot site-selective growth on GaAs substrates," *Physica Status Solidi (c)*, vol. 8, no. 4, pp. 1242-1245, 2011.

B. C. Richards, J. Hendrickson, J. D. Olitzky, R. Gibson, M. Gehl, K. Kieu, P. Polynkin, G. Khitrova, H. M. Gibbs, U. K. Khankhoje, A. Homyk, A. Scherer, J.-Y. Kim, and Y.-H. Lee, "Progress in growth, fabrication, and characterization of semiconductor photonic crystal nanocavities," *Physica Status Solidi (b)*, vol. 248, no. 4, pp. 892-896, 2011.

M. Helfrich, D. Hu, J. Hendrickson, M. Gehl, D. Rülke, R. Gröger, D. Litvinov, S. Linden, M. Wegener, D. Gerthsen, T. Schimmel, M. Hetterich, H. Kalt, G. Khitrova, H. M. Gibbs, and D. M. Schaadt, "Growth and annealing of InAs quantum dots on pre-structured GaAs substrates," *Journal of Crystal Growth*, vol. 323, no. 1, pp. 187-190, 2011.

M. Gehl, R. Gibson, J. Hendrickson, A. Homyk, A. Säynätjoki, T. Alasaarela, L. Karvonen, A. Tervonen, S. Honkanen, S. Zandbergen, B. C. Richards, J. D. Olitzky, A. Scherer, G. Khitrova, H. M. Gibbs, J.-Y. Kim, and Y.-H. Lee, "Effect of atomic layer deposition on the quality factor of silicon nanobeam cavities," *JOSA B*, vol. 29, no. 2, pp. A55-A59, 2012.

M. Gehl, S. Zandbergen, R. Gibson, M. Béchu, N. Nader, J. Hendrickson, J. Sears, P. Keiffer, M. Wegener, and G. Khitrova, "Spectroscopic studies of resonant coupling of silver optical antenna arrays to a near-surface quantum well," *Journal of Optics*, vol. 16, no. 11, p. 114016, 2014.

R. Gibson, M. Gehl, J. Sears, S. Zandbergen, N. Nader, P. Keiffer, J. Hendrickson, A. Arnoult, and G. Khitrova, "Molecular beam epitaxy grown indium self-assembled plasmonic nanostructures," *Journal of Crystal Growth*, vol. 425, pp. 307-311, 2015.

B. L. Wilmer, F. Passmann, M. Gehl, G. Khitrova, and A. D. Bristow, "Multidimensional coherent spectroscopy of a semiconductor microcavity," *Physical Review B*, vol. 91, no. 20, p. 201304(R), 2015.

Abstract

Nano-structures, such as photonic crystal cavities and metallic antennas, allow one to focus and store optical energy into very small volumes, greatly increasing light-matter interactions. These structures produce resonances which are typically characterized by how well they confine energy both temporally (quality factor - Q) and spatially (mode volume - V). In order to observe non-linear effects, modified spontaneous emission (e.g. Purcell enhancement), or quantum effects (e.g. vacuum Rabi splitting), one needs to maximize the ratio of Q/V while also maximizing the coupling between the resonance and the active medium. In this dissertation I will discuss several projects related by the goal of controlling light-matter interactions using such nano-structures.

In the first portion of this dissertation I will discuss the deterministic placement of self-assembled InAs quantum dots, which would allow one to precisely position an optically-active material, for maximum interaction, inside of a photonic crystal cavity. Additionally, I will discuss the use of atomic layer deposition to tune and improve both the resonance wavelength and quality factor of silicon based photonic crystal cavities.

Moving from dielectric materials to metals allows one to achieve mode-volumes well below the diffraction limit. The quality factor of these resonators is severely limited by Ohmic loss in the metal; however, the small mode-volume still allows for greatly enhanced light-matter interaction. In the second portion of this dissertation I will investigate the coupling between an array of metallic resonators (antennas) and a nearby semiconductor quantum well. Using time-resolved pump-probe measurements I study the properties of the coupled system and compare the results to a model which allows one to quantitatively compare various antenna geometries.

Controlling Light-Matter Interaction in Semiconductors with Hybrid Nano-Structures

Michael R. Gehl, Ph.D.
The University of Arizona, 2015

Director: Galina Khitrova

Nano-structures, such as photonic crystal cavities and metallic antennas, allow one to focus and store optical energy into very small volumes, greatly increasing light-matter interactions. These structures produce resonances which are typically characterized by how well they confine energy both temporally (quality factor - Q) and spatially (mode volume - V). In order to observe non-linear effects, modified spontaneous emission (e.g. Purcell enhancement), or quantum effects (e.g. vacuum Rabi splitting), one needs to maximize the ratio of Q/V while also maximizing the coupling between the resonance and the active medium. In this dissertation I will discuss several projects related by the goal of controlling light-matter interactions using such nano-structures.

In the first portion of this dissertation I will discuss the deterministic placement of self-assembled InAs quantum dots, which would allow one to precisely position an optically-active material, for maximum interaction, inside of a photonic crystal cavity. Additionally, I will discuss the use of atomic layer deposition to tune and improve both the resonance wavelength and quality factor of silicon based photonic crystal cavities.

Moving from dielectric materials to metals allows one to achieve mode-volumes well below the diffraction limit. The quality factor of these resonators is severely limited by Ohmic loss in the metal; however, the small mode-volume still allows for greatly enhanced light-matter interaction. In the second portion of this dissertation I will investigate the coupling between an array of metallic resonators (antennas) and a nearby semiconductor quantum well. Using time-resolved pump-probe measurements I study the properties of the coupled system and compare the results to a model which allows one to quantitatively compare various antenna geometries.

Chapter 1
Introduction and Motivation

Understanding the nature of light and its interaction with matter has always been an area of great interest in physics. While we have been controlling light since the time of the ancient Egyptians, physicists only began to unravel the nature of light within the last 150 years. This understanding began with the unification of electro-magnetic theory by James C. Maxwell in 1865 [1] and culminated in the field of quantum electro-dynamics in the mid 1900's. While the quantum description of light and matter has been extremely successful, truly controlling the interaction of light and matter has remained challenging due to the scale of optical wavelengths. With the amazing improvements in nano-fabrication of the last few decades, we are finally at a point where we can fabricate structures with sub-wavelength dimensions, allowing a new level of control over light. This has opened up entirely new possibilities in the fields of photonic crystals [2], meta-materials [3] and plasmonics [4].

1.1 Basics of Light-Matter Interactions

In the formal quantum mechanical treatment of N charged particles in an electro-magnetic field, one must consider the vector ($\mathbf{A}(\mathbf{r})$) and scalar ($\phi(\mathbf{r})$) potentials. This leads to the general Hamiltonian

$$H = \sum_{i=1}^{N} \frac{1}{2m_i}[\mathbf{p_i} - q_i\mathbf{A}(\mathbf{r_i})]^2 + q_i\phi(\mathbf{r_i}) \tag{1.1}$$

where $\mathbf{A}(\mathbf{r})$ and $\phi(\mathbf{r})$ include both external fields as well as those generated by the charges q_i.

In practice we are typically concerned with two bound particles (e.g. an electron and proton or an electron and hole) interacting with propagating electro-magnetic fields. In this case the Coulomb interactions between the two particles (a result of the longitudinal electro-magnetic fields) are treated separately, resulting in a spectrum of bound states with discrete energies. One then deals only with the transverse electro-magnetic fields, which in most cases have a spatial variation significantly larger than the separation of the two

charged particles. In this situation it benefits us to use the dipole approximation in which the interaction Hamiltonian is given by

$$H_I = -d \cdot E \tag{1.2}$$

where d is the dipole moment operator acting between bound states of our system and E is the electric field which can be treated either as a classical field or as a quantum mechanical operator.

A second assumption that we commonly make is that we are only dealing with two of the bound states of our charged particles. This is possible by operating in a narrow frequency (energy) range which is near the transition frequency (energy) of these two states, but greatly detuned from all other transitions. We consider the system to have only two states, an excited state $|e\rangle$ and a ground state $|g\rangle$.

1.1.1 Weak Coupling

In the weak coupling regime the interaction between the two-level transition and the electromagnetic field can be treated as a perturbation using Fermi's Golden Rule

$$\Gamma_{i\to f} = \frac{2\pi}{\hbar} \langle i|H'|f\rangle^2 \rho \tag{1.3}$$

describing the transition rate between an initial $|i\rangle$ and final state $|f\rangle$. In this equation H' is a perturbation (e.g. the dipole interaction from equation 1.2) and ρ is the density of final states. From this we see that in the perturbative (weak coupling) regime the transition rate is largely determined by the density of states. In an optical cavity we assume that we have a single mode with a Lorentzian lineshape, characterized by it's resonance frequency (ω_{cav}) and damping frequency (κ). The density of states is then found by dividing the normalized lineshape by the effective mode-volume (V)

$$\rho_{cav}(\omega) = \frac{\kappa}{2\pi V} \frac{1}{(\frac{\kappa}{2})^2 + (\omega - \omega_{cav})^2} \tag{1.4}$$

Taking the ratio of the density of states of the cavity to that of free space one then finds the well known resonant ($\omega = \omega_{cav}$) enhancement first predicted by Purcell [5]

$$F_p = \frac{\Gamma_{cav}}{\Gamma_{free}} = \frac{3\lambda^3}{4n^3\pi^2}\frac{Q}{V} \tag{1.5}$$

where Q is defined as ω_{cav}/κ.

1.1.2 Strong Coupling

If the losses in our system (γ, κ) are low enough we enter a regime where energy can coherently transfer between the cavity mode and the two-level system. In this regime we must treat the cavity mode quantum mechanically. This is accomplished by replacing E in eq. 1.2 with the electric field operator which leads to the well known Jaynes-Cummings model [6]. A mode of the bare cavity will have discrete levels $|n\rangle$ with energy $E_n = \hbar\omega_{cav}\,(n + 1/2)$, where n is the number of photons in the cavity mode. When the cavity and two-level system interact and are resonant with each other, the dipole interaction leads to new Eigenstates of the system which are now an entangled mixture of light and matter (given by eq. 1.6a and 1.6b) where the energy is both in the two-level system and in the cavity at the same time. Each of the $|n\rangle$ levels is now split in two with an energy separation of $2g\sqrt{n+1}$, where $\hbar g = \langle g|d|e\rangle\, E_{vac}$.

$$|n, +\rangle = \frac{1}{\sqrt{2}}\left(|n, e\rangle + |n+1, g\rangle\right) \tag{1.6a}$$

$$|n, -\rangle = \frac{1}{\sqrt{2}}\left(|n, e\rangle - |n+1, g\rangle\right) \tag{1.6b}$$

We see that even in the case of $n = 0$ the system has two levels $|0, +\rangle$ and $|0, -\rangle$, with separation $2g$, known as vacuum Rabi splitting [7, 8].

1.1.3 Dipole-Dipole Interaction

For much of the work described in this dissertation, we will not be concerned with dielectric optical cavities, but rather metallic resonators. In this case the metallic resonator produces a strongly enhanced near-field (longitudinal field) associated with the dipole moment of the structure. Instead of dealing with the near-field, we can consider the dipole moment of

the metallic oscillator and try to understand the coupling to other nearby oscillators as a direct dipole-dipole interaction. This idea is developed in a semi-classical model described in sec. 3.1.3.

While the quality-factor of dielectric cavities can be very high, the mode-volume is inherently limited by diffraction to approximately $(\lambda/2n)^3$. However, if we begin to incorporate metal into the cavity we find that we can reduce the mode-volume by several orders of magnitude, albeit at the cost of introducing considerable loss [9]. These subwavelength metallic resonators, (also known as optical antennas, plasmonic nanoparticles, meta-materials, etc.) have found a host of potential applications in high-resolution microscopy, single-photon sources, photo-voltaics, optical switching, meta-materials, Purcell enhancement and more [10–19]. It is tempting to treat these metallic resonators much like a dielectric cavity and classify them in terms of quality-factor and mode-volume; however, there are several key differences of which one must be careful.

The most important difference is the way in which energy is stored by a metallic resonator. In a dielectric cavity energy oscillates back and forth between the electric and magnetic fields. In a metallic resonator, the energy instead oscillates largely between the electric field and the kinetic energy of electrons in the metal [9].

An unfortunate result of this is the large amount of Ohmic loss associated with the resonator. The electrons in the metal are heavily damped due to electron-electron and electron-phonon scattering which leads to Ohmic losses (heating). This brings about the low quality factor of the resonator. At optical frequencies metallic resonators typically have quality factors on the order of 10. That is, if the resonance is centered at a wavelength of 1 μm, the spectral width of the resonance is on the order of 100 nm. This is compared to a photonic crystal cavity which may have a spectral width of less than 0.1 nm ($Q = 10000$).

At the same time, the ability to store energy in the kinetic movement of electrons leads to the fact that the mode-volume of the cavity can be extremely sub-wavelength. The electrons are oscillating in a metallic structure with dimensions on the order of 10-100 nm. Even when the energy is in the electric field, the fields are largely longitudinal fields which decay exponentially as you move away from the resonator. As a result the mode-volumes of these cavities can be nearly 1000 times smaller than the diffraction limit.

One major issue with classifying metallic resonators in terms of mode-volume is understanding the exact definition of this term. Due to the lossy nature of the mode, the mode is not truly localized; that is if you simulate the field surrounding the resonator one finds that the calculated mode-volume increases with the size of the simulation volume. One way to deal with this is shown in ref. [20]. The mode-volume is seen to diverge linearly as a function of the simulation size as a result of radiating fields. By fitting this linear divergence and substracting it from the mode-volume one ends up with a constant mode-volume which quantifies the localized portion of the field.

A second issue is the fact that a significant portion of the mode exists within the metal, a region with a negative value of permittivity. In the standard definition of mode-volume (eq. 1.7) we see that the permittivity is directly multiplied by the electric field magnitude inside of the integral. Inside of the metallic regions the field would actually make a negative contribution to the calculated mode-volume leading to values much less than expected. Reference [21] proposes the modification of eq. 1.7 to that of eq. 1.8 using the definition of electric field energy density in a highly dispersive, lossy medium [22]. This assumes a Drude model for the metal.

$$V = \int \frac{\epsilon |E|^2}{\max\left(\epsilon |E|^2\right)} \partial V \tag{1.7}$$

$$V^{lossy} = \int \frac{\left(\mathrm{Re}\left(\epsilon\right) + \frac{2\omega \mathrm{Im}(\epsilon)}{\gamma}\right) |E|^2}{\max\left[\left(\mathrm{Re}\left(\epsilon\right) + \frac{2\omega \mathrm{Im}(\epsilon)}{\gamma}\right) |E|^2\right]} \partial V \tag{1.8}$$

1.2 Previous Work

A large portion of this dissertation (Ch. 3) deals with the interaction of metallic resonators with a semiconductor quantum well. The origins of this pursuit lie in the field of meta-materials. This field aims to engineer materials with unnatural optical properties through the use of sub-wavelength features. This typically relies on the use of materials with negative permittivity (i.e. metals). Because of this, meta-materials inherently suffer from large Ohmic losses, limiting practical applications. The natural solution to this seems to be to introduce

a material which produces sufficient optical gain to compensate for this loss.

This was the goal of original investigations of the coupling of metallic resonators (in this case split-ring resonators) to a near surface quantum well [23]. Arrays of split-ring resonators were fabricated on the surface of a quantum well and analyzed in terms of loss compensation. It was found that the system was unable to compensate the losses (fig. 1.1), but a factor of three to four improvement in either the dipole moments, the damping frequencies, coupling constant or some combination of all of these could result in a system where the loss was completely compensated.

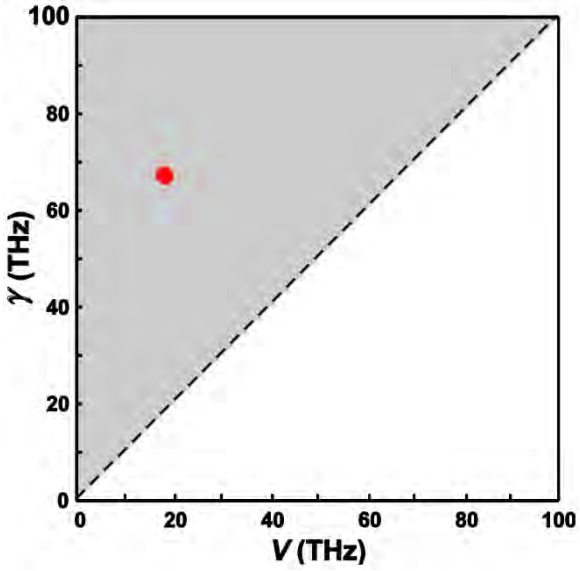

Figure 1.1: A plot of the effective damping frequency (γ) versus the effective coupling frequency (V) for an array of split-ring resonators coupled to a quantum well from ref. [23]. The red dot represents the experimentally measured system, the white region corresponds to complete loss compensation.

At the same time as the investigation of loss compensation, work was being done to measure the extinction cross-section of an individual metallic resonator [24, 25]. This is an important characterization of a metallic resonator which can reveal both the dipole moment and the damping frequency. The cross-section of a metallic resonator can be split into two contributions, scattering and absorption. The scattering cross-section is a measure of how much of an incident optical field will be scattered by the resonator into different propagating modes. That is, light which interacts with the dipole moment of the resonator, causing the

electrons to oscillate and is then re-radiated into free space. The second contribution is the absorption cross-section. This is related to the Ohmic losses of the resonator, and provides a measure of how much of the incident optical field is turned into heat. This is seen in fig. 1.2a-b where the absorption (red), scattering (green) and total (black) cross-sections of a split-ring resonator are plotted.

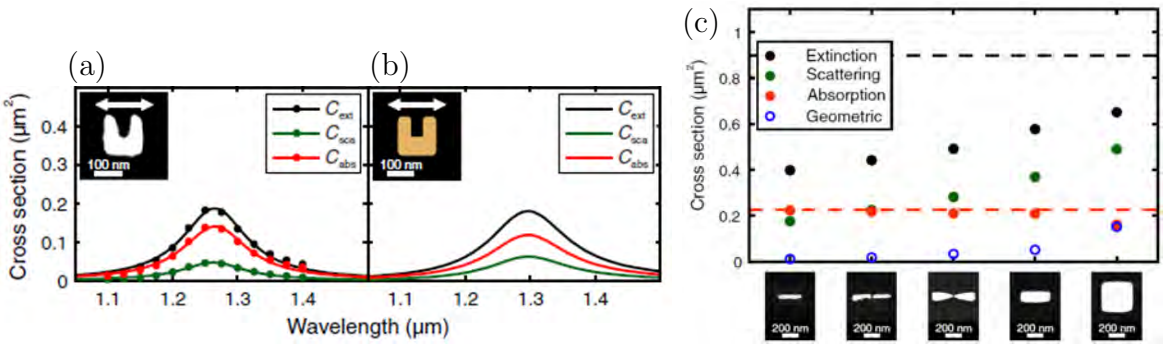

Figure 1.2: Example of measured (a) and simulated (b) cross-section of a split-ring resonator from ref. [25], and (c) comparison of cross-sections of various resonator shapes from ref. [26].

An important motivation for the current work was the measurement of the cross-sections of various resonator shapes (fig. 1.2c) [26]. It was shown that by changing the shape of the individual resonators the ratio of the scattering cross-section to the absorption cross-section can be increased. We can understand this intuitively by taking the split-ring resonator as an example. In fig. 1.2a we see that the absorption cross-section (red) is significantly larger than the scattering cross-section (green). If we were to deform the split-ring resonator by unfolding it into a dipole resonator, we see in fig. 1.2c that the scattering and absorption cross-sections are nearly equal. As we unfold the split-ring resonator we are moving the ends of the resonator further apart. The ends of the resonator are what define the dipole moment of the structure; as electrons oscillate within the structure there is a net charge that forms at the ends of the resonator. Unfolding the split-ring resonator therefore creates a larger dipole moment ($d = q \cdot x$), which in turn leads to a larger interaction with an incident electro-magnetic field and therefore a larger scattering cross-section. At the same time, if we treat the resonator as a wire, neither the length nor the cross-sectional area of the wire is changed significantly as we unfold it. Therefore, the resistance ($R = \rho l/A$) that an electron sees as it travels through the resonator is not changing and we would expect similar Ohmic

losses for both structures. This is in fact the case, and looking at fig. 1.2c we see that even as we change the shape in more significant ways the Ohmic losses (red) stay nearly constant, but the scattering cross-section (dipole moment) can be greatly increased.

With this in mind it was natural to ask how this variation of dipole moment could effect the coupling of the antenna to an active material (quantum well). As will be explained in sec. 3.1.3 the interaction is described as a dipole-dipole interaction resulting from the near-field of the metallic resonator. Therefore, it seems natural to assume that a larger dipole moment would lead to a larger interaction and possibly even loss compensation as speculated in ref. [23]. It will be shown in sec. 3.3.3 that this is, unfortunately, not the case, and there seems to be an inherent limitation to the coupling in this type of system.

1.3 Layout of Dissertation

This dissertation covers several of the main topics of my research during my time as a graduate student. The main results of this research are published in several journal publications which are included as appendices at the end of the dissertation. For the purposes of clarity, the work has been combined into a coherent story for the main body of this work. The dissertation is divided into four chapters, beginning with the introduction.

Chapter two focuses on the research conducted at the beginning of my doctoral degree which aimed to improve the coupling of photonic crystal based cavity-emitter systems. This includes work on the deterministic placement of semiconductor quantum dots (QD) [27, 28] as well as efforts to decrease loss and tune the resonance of minimum mode-volume photonic crystal cavities [29–31]. While I was not involved in the fabrication of the samples studied in this work I took a lead role in the measurement and analysis of these samples.

Chapter 3 discusses the primary work of my doctoral degree pertaining to the study of the coupling between metallic resonators (optical antennas) to a near-surface semiconductor quantum well (QW) [32]. This chapter includes an overview of basic semiconductor theory as well as the coupled oscillator model which was used to analyze data. The experimental aspects, including semiconductor growth, antenna fabrication and optical measurements are reported in detail. Finally, the results of optical measurements on these systems are presented. This includes low-temperature photo-luminescence (PL), Fourier transform infra-red

(FTIR) transmission spectra and transient pump-probe measurements.

In the fourth and final chapter I discuss the current direction of research in the Quantum Nano-Optics of Semiconductors (QNOS) group, including self-assembled plasmonic structures [33] and hybrid semiconductor/superconductor devices. Much of this work is just beginning and is very theoretical. Therefore I will cover the current understanding of the theory that is available in the literature, as well as how it applies to the systems under study in the QNOS group.

Chapter 2
Improving Quantum Dot - Photonic Crystal Structures

2.1 Deterministic Placement of Quantum Dots

The electro-magnetic field inside of an optical cavity forms a standing wave, meaning the field contains both nodes and anti-nodes (fig. 2.1b). At the location of nodes, the field magnitude is zero at all times, and as such a quantum dot placed at this location would experience zero interaction with the cavity mode. It is clearly important to make sure that the quantum dot is placed at an anti-node of the field. This is easier said than done as the formation of quantum dots happens through a random self-assembly process [34]. In practice the optimal placement of a quantum dot happens by fabricating many hundreds of photonic crystal cavities and then conducting a search to find the ideal cavity which has a dot located correctly, both spatially and spectrally. While this is challenging enough, once located, it is likely that the cavity will contain more than one dot. As long as only one dot is resonant with the cavity it may be possible to observe coupling, however, the extra dots in the cavity provide additional absorption and scattering losses which can lead to a broadening of the cavity linewidth. The ability to place one and only one quantum dot at the anti-node of a photonic crystal cavity would be a huge advantage to conducting cavity quantum electrodynamic (cQED) experiments with these systems. Not only would this open the door for interesting experiments involving more than a single cavity and dot [35], but it is essential for scalability if one wanted to create single or entangled photon sources [36–38].

The quantum dots studied in our lab are grown using molecular beam epitaxy (MBE). This technique is an ultra-high vacuum method which allows one to deposit extremely pure crystalline material in very precise amounts onto crystal substrates. This technique is described in more detail in section 3.2.1 in regards to the growth of quantum wells. Typically, one wants the lattice constant of the deposited material to be nearly identical to that of the underlying substrate. This minimizes strain in the deposited layers, leading to fewer

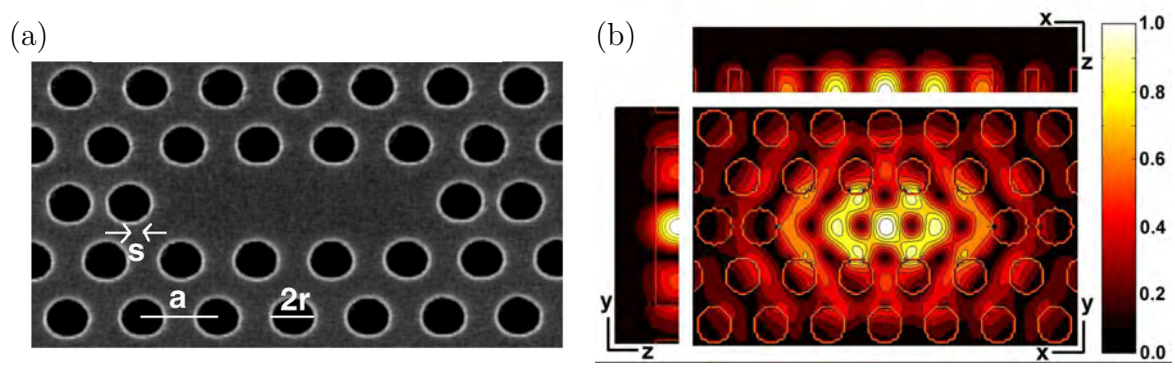

Figure 2.1: (a) SEM image of a GaAs-slab photonic crystal cavity and (b) simulated mode distribution, clearly showing locations of nodes and anti-nodes [7].

defects. As the material is deposited, atoms adsorb to the surface and move about. The mobility of these atoms allows for the formation of atomically smooth layers which build up, one by one. This mode of crystal growth is known as Frank van der Merwe (FM) growth. When forming quantum dots, (e.g. InAs deposited on GaAs), the growth proceeds by a very different method, known as the Stranski-Krastanov (SK) mode. This is a result of the large mismatch in lattice constants of InAs and GaAs (7.2% at room temperature). As InAs is deposited the first atomic layer, commonly referred to as the wetting layer, forms much like FM growth. This layer has a significant amount of strain and as more InAs is deposited, rather than forming a second atomic layer, it begins to nucleate into small islands. The formation of these islands (quantum dots) allows the crystal lattice to relax; however, the islands retain a crystalline structure. This is an important fact as it means the islands still retain a band-gap. Over-coating the islands with more GaAs completes the quantum dot by surrounding the island with a higher band-gap material. The InAs island now forms a 0-dimensional potential well which is able to confine charge carriers (electrons and holes).

The nucleation process of InAs quantum dots is random; however, we may hope to control this process by introducing locations at which nucleation will be preferential. For the samples we studied, this was accomplished by pre-patterning GaAs substrates with arrays of nano-scale indentations. GaAs substrates were first coated by a layer of polymethyl methacrylate/methacrylate (PMMA/MA) and arrays of holes were written into this layer using electron beam lithography (EBL) on a Raith e-line system. The pattern of holes was

developed and the substrate was then etched for 30 s in H_2SO_4:H_2O_2:H_2O (1:8:800). This resulted in indents with a depth of 20 nm in the substrate. The resist was removed using a series of baths consisting of acetone, methanol and isopropanol (IPA).

For growth of InAs quantum dots, the patterned substrate is first loaded into the load-lock chamber of a Riber 21T MBE system. After the chamber is pumped down the substrate is heated to 130°C for 1 hour to remove any volatile contamination. The substrate is transferred to the growth chamber and the surface oxide is removed using a unique Ga-assisted technique [39] which prevents damage to the pattern. This is accomplished by heating the substrate to 480°C followed by exposure to a low flux of ∼1 monolayer/min (ML/min) of gallium. The substrate is exposed to gallium for 30 s followed by a pause of 30 s. The excess gallium reacts with the surface oxide ($Ga_2O_3 + 4Ga \rightarrow 3Ga_2O$), producing Ga_2O which is more volatile and able to desorb from the surface. This is repeated for 16 cycles, or a total of about 8 monolayers (ML) of gallium, and then the substrate was heated to 550°C and annealed for 2 min under an As_4 atmosphere. The substrate was cooled to 500°C, at which point a 16 nm GaAs buffer layer was deposited, followed by InAs deposition (1.7 - 2.6 ML). Samples were annealed at growth temperature for varying amounts of time. Finally, samples for atomic force microscopy (AFM) study were rapidly cooled to room temperature, while samples for PL study were capped with 80 nm of GaAs and then cooled.

AFM measurements were conducted using a Nanosurf Easyscan 2 system. From these images it was found that InAs dots tended to form in pairs in each indent in the substrate. Annealing the sample was found to cause these double dots to merge into single dots. Additionally, the annealing lead to a decrease in the number of dots that formed in between etched holes. Figure 2.2 shows an AFM of sample A1130 which had no dots between holes, and a large percentage of single dots in holes.

Low-temperature photo-luminescence measurements were conducted at 10 K using a continuous flow liquid helium cryostat (CryoVac) and a HeNe laser to pump the sample. A high-NA, long working distance microscope objective (100X Mitutoyo Plan Apo NIR HR infinity corrected) is used to achieve a small spot size, so that only a small number of dots are excited. The emitted light is collimated and imaged using a 1.26m spectrometer (Spex Model 1269) and a liquid nitrogen cooled silicon CCD array (Princeton Instruments Model

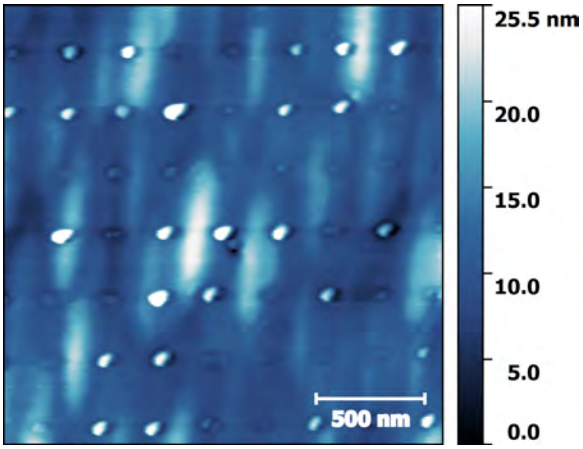

Figure 2.2: AFM image of sample A1130, showing no dots between sites and a large number of single dots.

LN/CCD-512-TKB/1/VISAR). Due to the low number of dots excited, narrow spectral lines originating from single quantum dots are resolvable.

One concern with deterministically placed dots is the introduction of defects as a result of the fabrication processes that happen prior to MBE growth. The defects will lead to a decreased quantum efficiency. Even if the dots form at the correct location they will be useless if they do not emit light. To test this we compared the integrated intensity of the PL from several locations on sample A1078, including two different patterned regions (one with holes spaced 250 nm apart and one 500 nm apart) and at un-patterned locations. Additionally, we collected AFM images of a similar un-capped sample (A1083), on the same patterned and un-patterned regions. Using these images we were able to count the average number of dots in holes and between holes. The quantum efficiency is then estimated using equations 2.1a, 2.1b and 2.1c, where C is a proportionality constant, P is the integrated PL intensity, η is the quantum efficiency, N is the average number of dots, and subscripts *bet*, *in* and *unpatt* stand for between holes, inside holes and un-patterned regions respectively.

$$C \times P^{(250)} = \eta_{\text{bet}} N_{\text{bet}}^{(250)} + \eta_{\text{in}} N_{\text{in}}^{(250)} \tag{2.1a}$$

$$C \times P^{(500)} = \eta_{\text{bet}} N_{\text{bet}}^{(500)} + \eta_{\text{in}} N_{\text{in}}^{(500)} \tag{2.1b}$$

$$C \times P_{\text{unpatt}} = \eta_{\text{unpatt}} N_{\text{unpatt}} \tag{2.1c}$$

Using this set of equations one finds that the relative efficiency of dots between holes to dots in un-patterned regions is 0.996 and the relative efficiency of dots inside of holes to dots between holes is 0.306. This shows that dots inside of holes do in fact emit light; however, the efficiency is significantly less and more work is needed to improve this method of quantum dot growth.

2.2 Tuning Photonic Crystal Cavities with Atomic Layer Deposition

A second limitation of QD/photonic crystal cavity systems has been the quality factor of the cavity. Despite simulations which show very high quality factors, actual fabricated devices typically perform significantly worse. This may be due to surface roughness after fabrication, or it could be due to absorption losses of the material. In the GaAs based photonic crystal cavity systems the quality factor rarely gets above 15,000. On the other hand, it has been seen that silicon based photonic crystal cavities exhibit much higher quality factors, easily reaching 100,000+. With this knowledge we decided to investigate these cavities to see just how high the quality factor in a minimum mode-volume cavity could reach. The cavity we investigated is shown in fig. 2.3, and consists of a silicon ridge waveguide on top of a silicon oxide layer. Holes are etched along the length of the waveguide, forming a 1D photonic crystal. The diameter of the holes is tapered down towards the center of the cavity, forming a defect where the mode is confined. This taper allows for a gradual change in the photonic crystal bandgap, therefore it gently confines the mode, avoiding abrupt changes which would increase scattering and lead to a lower Q.

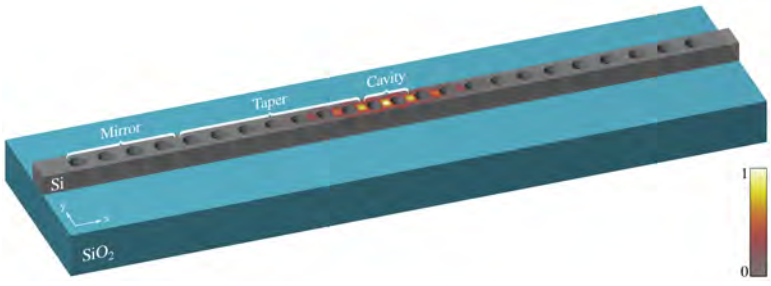

Figure 2.3: Schematic of a silicon based 1D photonic crystal cavity.

The obvious drawback to using silicon photonic crystal cavities is the lack of active emitters that can easily be incorporated with the cavity. However, high Q, low V cavities are still of great interest for increasing non-linear effects [40] and for cavity opto-mechanics [41]. There is also much effort to incorporate active material with silicon photonics [42–44], with mixed results. The lack of active emitter makes optical measurements of the cavity mode more challenging. In GaAs cavities containing QD's we can simply excite the QD's and observe the PL. Without this option we must provide a light source (A tunable laser - Agilent Model 81682A), and observe the transmission or reflection of the cavity, using either a tapered optical fiber or a free-space method [29].

Fiber Taper Method The tapered fiber method relies on a single-mode optical fiber which has been heated and pulled to form an adiabatic taper [45] with a diameter on the order of 1 μm. The tapered region of the fiber is formed into a loop which is then positioned on top of the cavity using micro-positioners, as seen in fig. 2.4a. The tunable laser light is passed into one end of the optical fiber and the intensity is detected at the opposite end. The laser wavelength is tuned and as it comes into resonance with the cavity some of the light is able to couple into the cavity through the evanescent field of the fiber. This light then scatters out of the cavity resulting in an observed dip in the intensity transmitted through the fiber taper.

The coupling of the fiber to the cavity is highly dependent on the relative position and orientation of the fiber. When placed over the center of the cavity the fiber will show the highest coupling; however, at this position the fiber introduces a large amount of loss into the cavity greatly reducing the Q. Therefore, it is beneficial to move the fiber away from the center of the cavity to reduce losses. There is a trade off between the measured Q and the signal to noise ratio. The coupling is also dependent on the angle between the cavity and the fiber as a result of available polarizations. The cavity mode is polarized linearly perpendicular to the axis of the nanobeam and parallel to the substrate surface. If the fiber were placed perpendicular to the nanobeam it would be impossible to couple to the cavity mode as the polarization would always be orthogonal. Placing the fiber parallel to the nanobeam once again introduces a large amount of loss due to the long interaction length.

Therefore the optimal contact is at a 45° angle and positioned near the end of the nanobeam cavity.

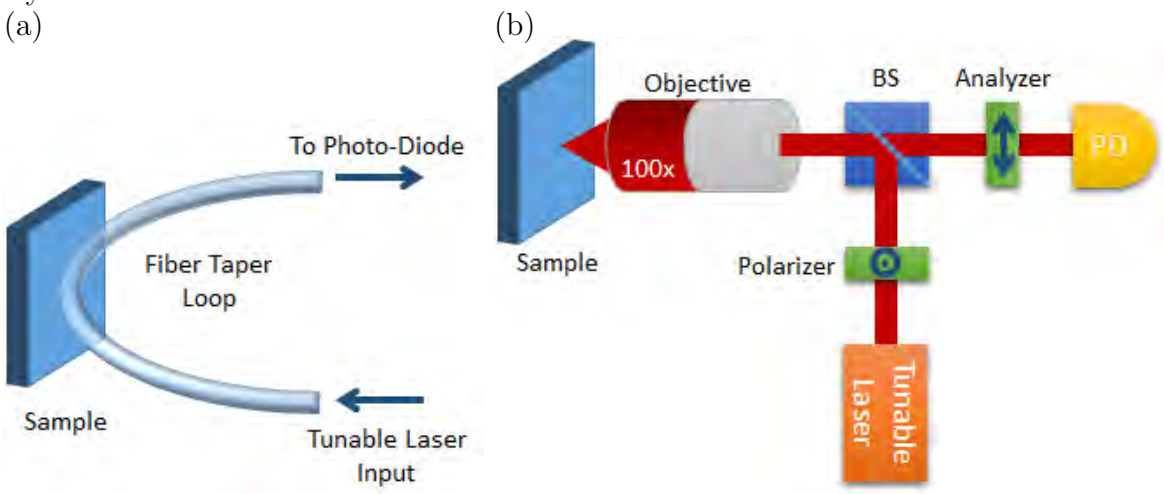

Figure 2.4: (a) Fiber taper method, in which a tapered fiber is brought into contact with the photonic crystal cavity, and (b) resonant scattering method in which a laser is focused onto the cavity and the polarization of the scattered light is analyzed to extract the cavity mode.

Resonant Scattering Method In order to measure the intrinsic Q of the cavity, without introducing additional losses, we must use a free space method. Figure 2.4b shows a schematic of the free space resonant scattering method. In this technique the tunable laser is focused onto the cavity using a high resolution microscope objective. The laser is linearly polarized at 45° with respect to the polarization of the cavity mode. The reflected light is collected by the same objective and passes through a polarizer which is oriented at 90° with respect to the incident laser polarization. Light which directly reflects from the sample is blocked by this polarizer. Light which couples into the cavity will scatter out of the cavity with polarization rotated by 45° and will partially transmit through the polarizer and be registered by an InGaAs detector. As mentioned this technique measures the intrinsic Q; however, cavities with high Q's scatter very little light resulting in a very low signal-to-noise ratio. As a result this technique can be difficult and is typically done only after the wavelength of the cavity resonance has already been determined by the fiber taper method.

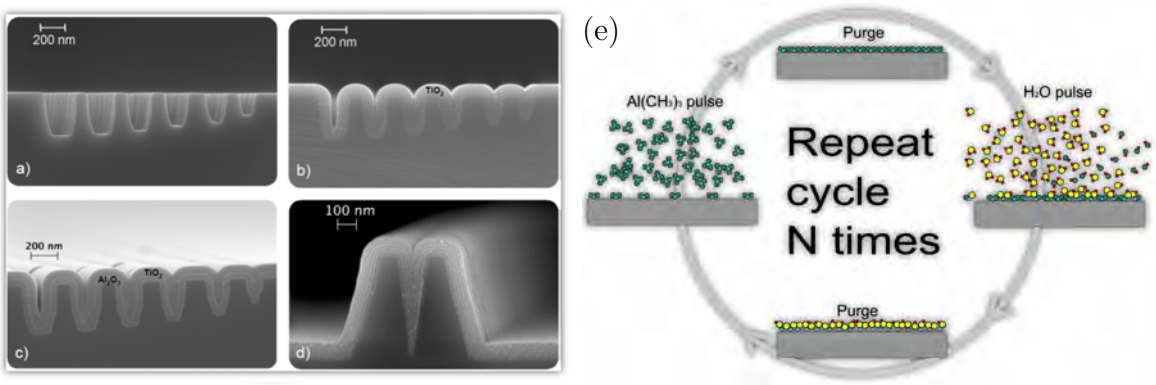

Figure 2.5: (a-d) Several SEM images demonstrating the conformal nature of ALD which is able to fill in gaps and indents in a sample. (e) Illustration of the atomic layer deposition process where a sample is successively exposed to two precursor materials which react at the surface of the sample [46, 47].

Results of Atomic Layer Deposition It has been shown that atomic layer depostion can lead to a reduction of propagation losses in silicon ridge waveguides [47]. This is attributed to the conformal nature of the ALD process (fig. 2.5) which is able to fill in defects to form a smooth surface. With this in mind we decided to investigate the effect of atomic layer deposition on silicon nanobeam cavities [31]. Two samples were fabricated with an array of cavities and the quality factor of each was measured. One sample was coated with 20 nm of Al_2O_3 and the other was coated with 20 nm of TiO_2. The samples were then measured again by the same procedure. The samples coated with TiO_2 showed on average a change in Q of $-1.3\% \pm 16\%$, while the sample coated with Al_2O_3 showed an average increase of $38\% \pm 31\%$. This increase in Q from Al_2O_3 is demonstrated in fig. 2.6a.

A second sample was fabricated which had a series of cavities which had the radius of etched holes shifted from that of the optimum design. This sample was characterized, coated with 20 nm of Al_2O_3 and then characterized again. This sample also showed an average increase in Q ($20\% \pm 19\%$). It was noticed that cavities which had larger holes to begin with saw the greatest increase in Q. It seems reasonable that the largest contribution to the increase in quality factor is not the 'smoothing' effect seen in ref. [47], but instead due to a post-fabrication 'correction' of the hole radius. Cavities with holes that are too large are essentially being brought closer to the optimal design by the addition of the ALD layer.

It is also worth noting the ability of this method to tune the wavelength of the cavity

resonance. Figure 2.6b shows the measured shift in cavity resonance for various initial hole radii. Depending on the initial geometry the cavity shifts anywhere from 20 nm to 28 nm. The ALD process builds up a film layer by layer (fig. 2.5). For the process used in this work each layer was approximately 0.1 nm thick. It therefore took 200 cycles to build up a 20 nm layer. We can then approximate the cavity shift per layer to be on the order of 0.1-0.15 nm, allowing precise post-fabrication control over the resonance wavelength.

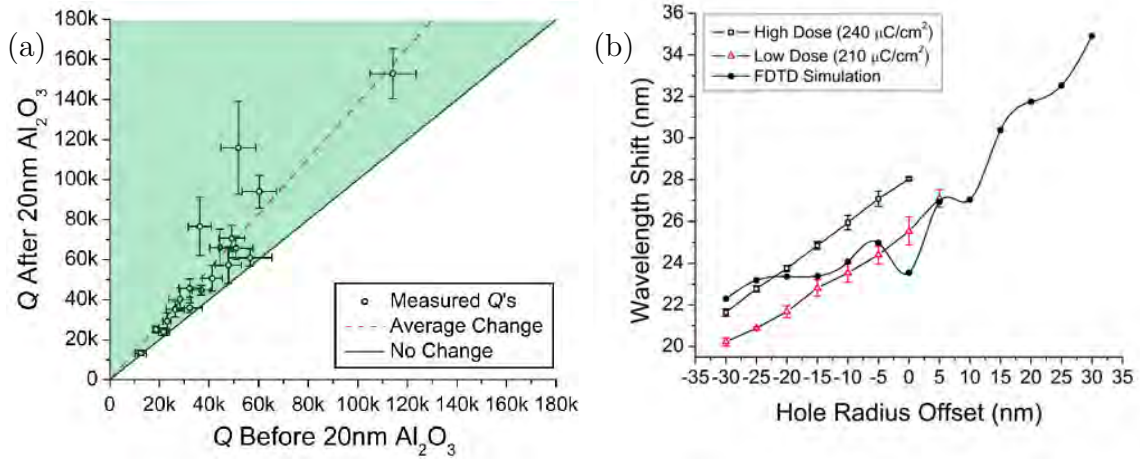

Figure 2.6: (a) Demonstration of the increased quality factor of silicon nanobeam cavities following the deposition of 20 nm of Al_2O_3, and (b) the resulting shift in cavity resonance wavelength as a function of the initial cavity hole radius.

Chapter 3

Metallic Cavity Systems

3.1 Theory

3.1.1 Optical Properties of Semiconductor Structures

Band Structure When working in condensed matter physics we can determine much about a material by understanding its band diagram. That is, the relationship between energy and momentum of the allowed electronic states. For example, in fig. 3.1a we see the band diagram of a single free electron, given by the relation $E = \hbar^2 k^2 / 2m_e$. When the electron becomes bound to an atom its linear momentum will go to zero, and it will be restricted to discrete energy levels (fig. 3.1b). However, if we bring a large number of atoms together to form a solid, the electron wave-functions of individual atoms begin to overlap and the electrons begin to interact through the Coulomb force. This interaction leads to new Eigenstates of the system, which are extended in space and have slightly shifted energies. For each discrete energy level of the original atom, there now forms a band of energy levels with non-zero momentum (fig. 3.1c).

To characterize the electrical and optical properties of a material we must introduce the Fermi level, a hypothetical energy level which has a 50% probability of being occupied by

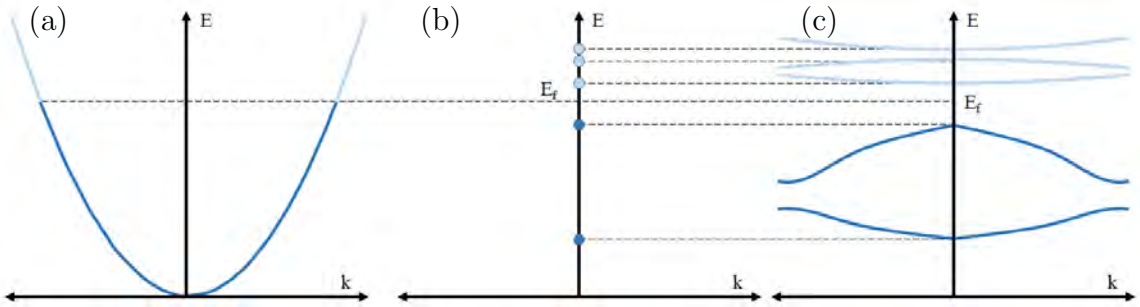

Figure 3.1: Dispersion relation of (a) a free electron, (b) a bound electron, and (c) an electron in a crystal lattice. Dark blue represents filled levels, at T = 0 K all levels below the Fermi level (E_f) will be filled.

an electron when the system is in thermal equilibrium. At 0 K all electron states below this energy are filled and all states above it are empty. If the Fermi level occurs within an energy band there are a large number of states around the Fermi level which are available to conduct a current and the material is considered a metal. If the Fermi level happens to fall in a gap between two bands (as in fig. 3.1c) there are no available states and the material is considered an insulator. If this gap between bands is on the order of a few electron volts (eV) then it is classified as a semiconductor.

Optical Transitions In a semiconductor, this gap between bands is large enough that it will be insulating under normal conditions. However, through doping (introducing impurities) or through the absorption of optical energy, carriers can be moved between bands allowing the material to become conducting, hence the name semiconductor. For this work we are primarily concerned with optical properties and will neglect doping. In this case the Fermi level lies near the middle of the band-gap, and the bands below this (valence bands) are completely full while the bands above this (conduction bands) are completely empty (at 0 K).

If a photon with energy greater than the band-gap is incident on the semiconductor, it is possible that the photon will be absorbed resulting in the transition of an electron from a valence band to a conduction band. The electron is now considered a free carrier. Additionally, the electron leaves behind an empty state in the valence band. It is possible for another electron in the valence band to move into this empty state, effectively causing the empty state to move. Rather than keep track of $\sim 10^{24}$ /m^3 electrons in the valence band, it is much easier to keep track of a single empty state which we treat as an effective positive charge carrier which is referred to as a hole. The absorption of a photon then creates a negative electron in the conduction band and a positive hole in the valence band. In this transition momentum must be conserved. Since the momentum of a photon is tiny compared to that of an electron we approximate the photon momentum as zero, and a transition involving the absorption or emission of a photon then appears as a vertical line in momentum space as seen in fig. 3.2.

The absorption of a photon creates a non-equilibrium state of the semiconductor (i.e.

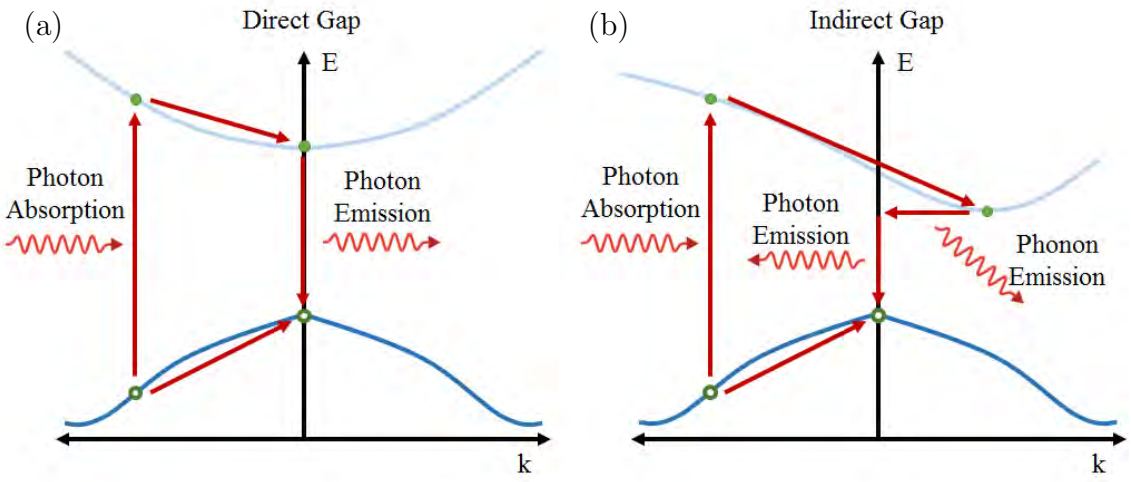

Figure 3.2: Example of photon absorption and emission in (a) direct and (b) indirect gap semiconductors.

the electrons are no longer in a thermal distribution). As a result the charges of the system will begin to relax towards equilibrium. This happens through the scattering of energetic electrons with other electrons or with the crystal lattice (phonons). These scattering events happen on very short time scales of a few picoseconds or less. Through many scattering events the non-equilibrium electrons 'fall' towards the lowest energy state of the energy band which it occupies. Likewise holes 'rise' towards the highest energy state of the band which they occupy. Once the electron (hole) reaches the lowest (highest) energy state, it is still not at thermal equilibrium since it has not returned to the original band from which it came. However, to transition to a different band it must lose an amount of energy equal to the band-gap, much larger than the energy of typical scattering events, and therefore the electron(hole) may sit at this position for much longer periods of time.

From this point the relaxation process can happen in a number of ways, strongly dependent on the structure of the energy bands involved. If the highest point of the valence band and the lowest point of the conduction band lie at the same location in momentum space then we are in luck. This is considered a direct gap semiconductor (fig. 3.2a). An electron in the conduction band will be able to transition to fill the hole in the valence band, without a change in momentum. The transition will likely result in the emission of a photon with energy equal to that of the band-gap. If we're not this lucky, the electron and hole do

not align in momentum space, the process is considered indirect (fig. 3.2b). If the electron and hole were to recombine and only emit a photon, conservation of momentum would be violated. For this recombination to occur the momentum must be transferred to a vibration of the crystal lattice (a phonon). This three-particle transition is much less likely to occur than a two-particle transition. It is more likely that the electron and hole will recombine through other processes which do not involve the emission of a photon, making indirect band structures poor optical emitters. For this reason we will be mainly concerned with direct gap semiconductors.

Confined Structures As mentioned above, non-equilibrium electrons(holes) quickly relax to the lowest(highest) energy states of the energy band. Therefore, for the design of semiconductor hetero-structures (structures formed from two or more material compositions) we move from momentum-space to real space and take the energy gap as the defining energy between the valence and conduction bands (fig. 3.3a-b). We can use this idea to understand the design of a quantum well, composed of a thin layer of material with a small band-gap sandwiched between two layers of a material with a larger band-gap (fig. 3.3c). This band-gap structure acts as a square well potential for electrons(holes) traveling perpendicular to the quantum well layer. We know from introductory quantum mechanics that a square well potential leads to states with discrete energy levels within the well. Within the plane of the quantum well, electrons(holes) are still free to move about in two dimensions with a continuum of momentum states. Therefore, each of the discrete levels of the quantum well acts similar to a two-dimensional electron gas. Each of these levels is shifted from the bulk band-gap by the confinement energy of the quantum well. The confinement energy is a function of the barrier height and the width of the quantum well layer. As a result one can engineer the energy levels of the quantum well to obtain transitions at a desired energy simply by changing either the material composition or the layer structure.

For this work we use a quantum well made of a layer of $In_{0.532}Ga_{0.468}As$ sandwiched between layers of $In_{0.524}Al_{0.476}As$. The band-gap of $In_{0.532}Ga_{0.468}As$ at 10 K is 0.814 eV and $In_{0.524}Al_{0.476}As$ has a band-gap of 1.5188 eV. The $In_{0.532}Ga_{0.468}As$ layer is only 13.8 nm thick, which leads to an additional confinement energy (of the lowest transition) of

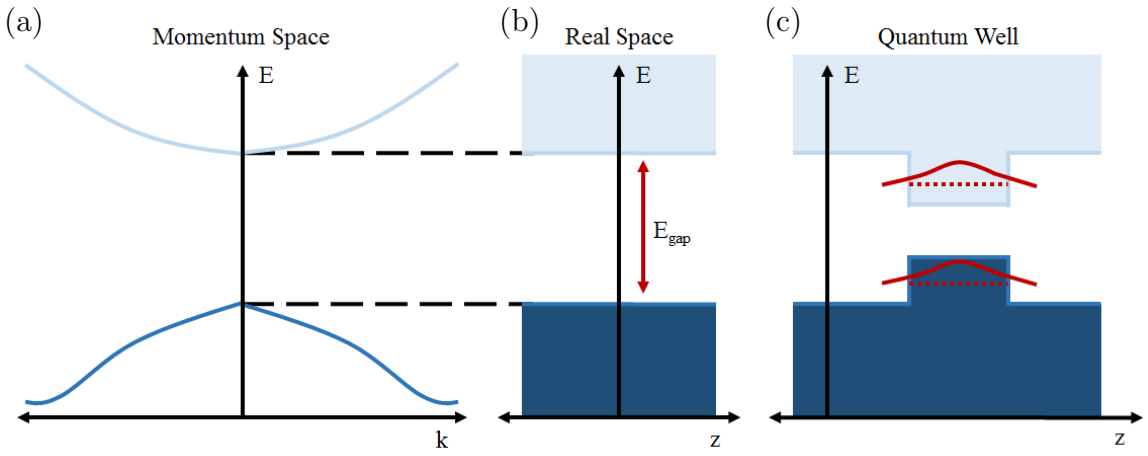

Figure 3.3: Energy gap shown in (a) momentum space and (b) real space. (c) Example of a quantum well consisting of a low energy band-gap material sandwiched between high band-gap barriers in real space.

about 13 meV. This additional energy puts the lowest energy transition at 0.827 eV or a wavelength of approximately 1500 nm. This lowest energy transition is between the first confined electron state (e1) in the conduction band and the first confined hole state (hh1, there are actually three valence bands, but due to spin-orbit interactions and the confinement of the quantum well they are non-degenerate and we only consider the 'heavy-hole' band). The next transition of this quantum well happens around 0.912 nm (or 1360 nm). This is sufficiently far from the lowest transition (for the low pump-power regime) that we treat the quantum well as a single transition with a ground state and an excited state separated by 0.827 eV. This is an extreme simplification, and it quickly breaks down if the carrier density is too high (i.e. higher pump-powers).

3.1.2 Simulating Optical Nano-Structures

The simulation of optical nano-structures was accomplished using finite difference time domain (FDTD) methods. A commonly used tool for this is MEEP (MIT Electromagnetic Equation Propagation) [48], a free FDTD software package. For rough simulations, this software provides adequate flexibility and can be run on a decent desktop computer (e.g. 4-core, 3.4 GHz CPU with 16 Gb RAM). MEEP is also available to be run through the free online cloud computing resources of Nanohub.org. For published simulations, we used the

much more flexible softare, "Sim3D_Max"^{TM}, of the research group of Dr. Jerome Moloney. This software allows for a flexible simulation grid. The resolution of the simulation can be locally increased, for example at the location of nano-scale features, and then decreased in uniform regions. This, along with the ability to run on a large number of parallel processors, allows for much more intensive simulations.

A critical part of simulating metallic structures using FDTD methods is implementing the correct dispersion relationship for the materials. For metals, we typically use the Lorentz-Drude model (eq. 3.1), which gives the permittivity as a sum of several resonances [49]. The parameters of this model are determined experimentally and reasonable values can be found in several places [49–51]. Unfortunately, these experimentally determined parameters are typically for bulk material. For nano-scale structures there's no guarantee that these parameters will hold, and they will likely depend on the purity and morphology of the metal. Despite this, FDTD simulations provide useful information such as optical mode distribution and general trends with respect to device dimensions.

$$\epsilon(\omega) = 1 - \frac{f_1\omega_p^2}{(\omega^2 + \mathrm{i}\Gamma_1\omega)} + \sum_{j=2}^{N} \frac{f_j\omega_p^2}{\left(\omega_j^2 - \omega^2 + \mathrm{i}\Gamma_j\omega\right)} \tag{3.1}$$

3.1.3 Coupled Oscillator Model

For the purposes of comparing measured differential transmission data of a quantum well coupled to a plasmonic resonance it is useful to introduce a model of two coupled oscillators [52]. This model incorporates the interaction between the two oscillators as a near-field interaction. This is in essence a dipole-dipole interaction. The dipole moment of each oscillator generates a longitudinal (non-propagating) field. This field then acts as a driving force on the dipole moment of the other oscillator. Therefore we must begin with the equations of motion of the two oscillators, incorporating this dipole-dipole interaction, and then calculate the optical properties of the coupled system.

Optical Bloch Equations We begin with the density matrix for a two-level system [53].

$$\rho = \begin{bmatrix} \rho_{11} & \rho_{12} \\ \rho_{21} & \rho_{22} \end{bmatrix} \tag{3.2}$$

Where ρ_{11} and ρ_{22} are the population of the lower and upper state, respectively, and $\rho_{21} = \rho_{12}^*$ is the complex transition amplitude. The equations of motion are then given by

$$\mathrm{i}\hbar\frac{\partial\rho}{\partial t} = [H, \rho] \tag{3.3}$$

Where H is the dipole interaction Hamiltonian (eq. 1.2). Considering the interaction of the two-level system with an optical field detuned from resonance by $\delta \equiv \omega_0 - \omega$ and including spontaneous emission as an exponential decay of the population at a rate of A_{21} leads to the optical Bloch equations equations in the rotating wave approximation.

$$\frac{\partial\rho_{11}}{\partial t} = A_{21}\rho_{22} - \frac{\mathrm{i}}{2}(\chi\rho_{12} - \chi^*\rho_{21}) \tag{3.4a}$$

$$\frac{\partial\rho_{22}}{\partial t} = -A_{21}\rho_{22} + \frac{\mathrm{i}}{2}(\chi\rho_{12} - \chi^*\rho_{21}) \tag{3.4b}$$

$$\frac{\partial\rho_{12}}{\partial t} = -\left(\frac{A_{21}}{2} - \mathrm{i}\delta\right)\rho_{12} + \frac{\mathrm{i}\chi^*}{2}(\rho_{22} - \rho_{11}) \tag{3.4c}$$

$$\frac{\partial\rho_{21}}{\partial t} = -\left(\frac{A_{21}}{2} + \mathrm{i}\delta\right)\rho_{12} - \frac{\mathrm{i}\chi}{2}(\rho_{22} - \rho_{11}) \tag{3.4d}$$

Where χ is the Rabi frequency, given by

$$\chi = (e\,\langle 1|r|2\rangle \cdot \hat{\epsilon})\,\frac{E_0}{\hbar} = \frac{d_{12}E_0}{\hbar} \tag{3.5}$$

If we define $f \equiv \rho_{22}$ to be the occupation of the upper level and use the conservation of probability ($\rho_{22} + \rho_{11} = 1$) we can simplify the equation of motion for ρ_{22}.

$$\frac{\partial f}{\partial t} = -A_{21}f + \frac{\mathrm{i}}{2\hbar}\left(d_{12}E_0\rho_{12} - d_{12}^*E_0^*\rho_{21}\right) \tag{3.6}$$

Similarly, the equation for the complex transition amplitude, $\rho \equiv \rho_{21}$, can be simplified to

$$\frac{\partial\rho}{\partial t} = -\left(\frac{A_{21}}{2} + \mathrm{i}\delta\right)\rho + \frac{\mathrm{i}d_{12}E_0}{2\hbar}\left(1 - 2f\right) \tag{3.7}$$

Equations 3.6 and 3.7 describe a fermionic two-level system, and will be used to model our quantum well. A similar set of equations can be found for bosonic systems, except that the factor $(1 - 2f)$ in eq. 3.7 is set to unity. Equation 3.8 will be used to model the mode of our metallic resonator.

$$\frac{\partial\rho}{\partial t} = -\left(\frac{A_{21}}{2} + \mathrm{i}\delta\right)\rho + \frac{\mathrm{i}d_{12}E_0}{2\hbar} \tag{3.8}$$

Near-field Coupling In order to account for coupling between our two oscillators we must define the macroscopic polarization of each. We introduce the subscripts $_{QW}$ and $_{PL}$ for the quantum well and plasmonic resonances, respectively. The macroscopic polarizations are then found by multiplying the transition amplitude by the dipole moment (d) and the dipole density (N).

$$P_{QW} = N_{QW} d_{QW} \rho_{QW} + \text{c.c.} \tag{3.9a}$$

$$P_{PL} = N_{PL} d_{PL} \rho_{PL} + \text{c.c.} \tag{3.9b}$$

It is assumed that this polarization generates an electric field which is accounted for by adding the polarization times a coupling constant L to the electric field which drives each oscillator.

$$E_{QW} = E_0 + L P_{PL} \tag{3.10a}$$

$$E_{PL} = E_0 + L P_{QW} \tag{3.10b}$$

Finally, we look for steady-state solutions, meaning we replace f with a constant and set all derivatives with respect to time to zero. (For consistency with published work we make the substitution $\frac{A_{21}}{2} \equiv \gamma$)

$$-\left(\gamma_{QW} + \mathrm{i}\delta_{QW}\right)\rho_{QW} + \frac{\mathrm{i}d_{QW}}{2\hbar}\left(E_0 + L\left(N_{PL} d_{PL} \rho_{PL} + \text{c.c.}\right)\right)(1-2f) = 0 \tag{3.11a}$$

$$-\left(\gamma_{PL} + \mathrm{i}\delta_{PL}\right)\rho_{PL} + \frac{\mathrm{i}d_{PL}}{2\hbar}\left(E_0 + L\left(N_{QW} d_{QW} \rho_{QW} + \text{c.c.}\right)\right) = 0 \tag{3.11b}$$

Solving this set of equations lead to the steady-state transition amplitudes.

$$\rho_{QW} = \frac{(1-2f)\, d_{QW}\left(1 + \dfrac{L N_{PL} d_{PL}^2}{\hbar\left(\delta_{PL} - \mathrm{i}\gamma_{PL}\right)}\right)}{\hbar\left(\delta_{QW} - \mathrm{i}\gamma_{QW}\right) - (1-2f)\dfrac{L^2 d_{QW}^2 d_{PL}^2 N_{QW} N_{PL}}{\hbar\left(\delta_{PL} - \mathrm{i}\gamma_{PL}\right)}} \frac{E_0}{2} \tag{3.12a}$$

$$\rho_{PL} = \frac{d_{PL}}{\hbar\left(\delta_{PL} - \mathrm{i}\gamma_{PL}\right)}\left(1 + L N_{QW} d_{QW} \rho_{QW}\right)\frac{E_0}{2} \tag{3.12b}$$

Linear Optical Properties Substituting 3.12a and 3.12b into 3.9a and 3.9b allows one to calculate the macroscopic polarization of each oscillator. The linear transmission, reflection and absorption of the coupled system is then calculated using either a transfer matrix method or

the Maxwell-Garnett effective-medium method. Both methods produce very similar results, so for this work we use the Maxwell-Garnett method which is computationally easier. In this method we take a weighted average of the macroscopic polarizations as follows.

$$P = \frac{l_{QW}}{l_{QW} + l_{PL}} P_{QW} + \frac{l_{PL}}{l_{QW} + l_{PL}} P_{PL} = \epsilon_0 \chi \frac{E_0}{2} exp\left(-\mathrm{i}\omega t\right) + \text{c.c.} \tag{3.13}$$

Where l_{QW} and l_{PL} are the layer thickness of the quantum well and plasmonic resonance, respectively.

From eq. 3.13 one can extract χ and from this the complex refractive index. This is then used to calculate the normal-incidence complex transmittivity (eq. 3.14a) and reflectivity (eq. 3.14b), where $Z = Z_0\sqrt{\frac{\mu}{\epsilon}}$ is the impedance and i and t are the medium on the incident and transmitted side, respectively [54].

$$t(\omega) = \frac{2}{\left(1 + \frac{Z_i}{Z_t}\right)\cos\left(\frac{\omega n(\omega) d}{c}\right) - \mathrm{i}\left(\frac{Z(\omega)}{Z_t} + \frac{Z_i}{Z(\omega)}\right)\sin\left(\frac{\omega n(\omega) d}{c}\right)} \tag{3.14a}$$

$$r(\omega) = \frac{\left(1 - \frac{Z_i}{Z_t}\right)\cos\left(\frac{\omega n(\omega) d}{c}\right) - \mathrm{i}\left(\frac{Z(\omega)}{Z_t} - \frac{Z_i}{Z(\omega)}\right)\sin\left(\frac{\omega n(\omega) d}{c}\right)}{\left(1 + \frac{Z_i}{Z_t}\right)\cos\left(\frac{\omega n(\omega) d}{c}\right) - \mathrm{i}\left(\frac{Z(\omega)}{Z_t} + \frac{Z_i}{Z(\omega)}\right)\sin\left(\frac{\omega n(\omega) d}{c}\right)} \tag{3.14b}$$

$$T(\omega) = \frac{n_t}{n_i}|t(\omega)|^2 \tag{3.15a}$$

$$R(\omega) = |r(\omega)|^2 \tag{3.15b}$$

Model Parameters We now see that we have 12 parameters in this model. Each oscillator has a resonance frequency (Ω), a damping frequency (γ), a dipole moment (d), a density (N) and a layer thickness (l). Additionally, the quantum well has an occupation factor (f) and the two oscillators interact through the coupling constant (L). We are able to measure each oscillator essentially independently, revealing Ω, γ, d, N, and l for each. This is demonstrated in fig. 3.4. In fig. 3.4a differential transmission measurements of quantum well HSG64 are fit to this model. The quantum well is assumed to be inverted by the pump ($f = 0 \rightarrow 1$), and the density (N_{QW}) is approximated by the effective density of electronic states. The

thickness (l_{QW}) is taken from the designed thickness of the quantum well. The resonance frequency, damping frequency, and dipole moment are allowed to vary in order to fit the measured data. Similarly, in fig. 3.4b, absolute transmission measurements of an array of antennas is measured and fit to the model. The density (N_{PL}) and layer thickness (l_{PL}) is known exactly from fabrication and the remaining parameters are varied to fit the data. The only remaining parameter is the coupling constant (L) which is varied to fit differential transmission measurements of the coupled system.

A final figure-of-merit that is used in this model is the effective coupling frequency (V_{eff}). This parameter, eq. 3.16, takes into account not only the coupling constant (L), but also the dipole moment and density of the two oscillators. This is important as both of these parameters are a factor in the magnitude of the observed interaction between the oscillators.

$$V_{eff} = \frac{1}{\hbar} d_{QW} d_{PL} L \sqrt{N_{QW} N_{PL}} \tag{3.16}$$

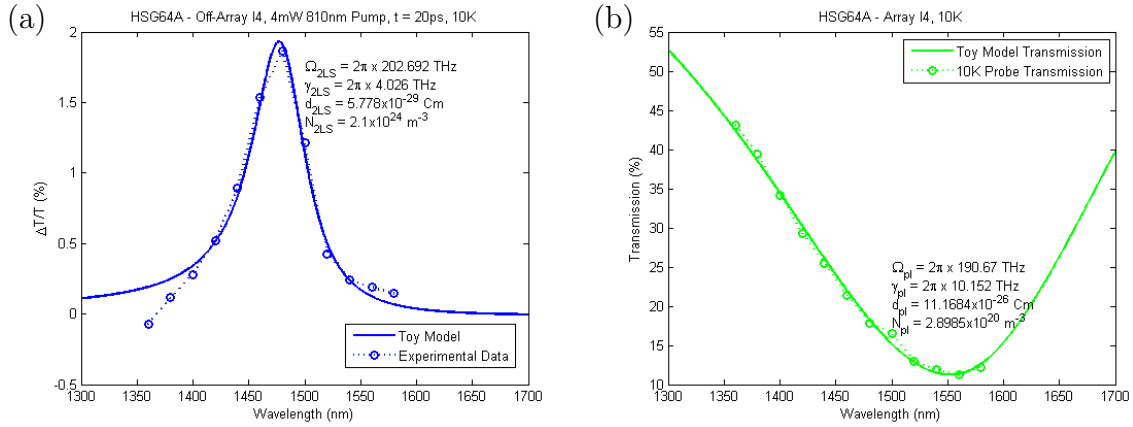

Figure 3.4: Example of fitting the oscillator model to measured data. (a) Peak differential transmission measurement of the quantum well and (b) absolute transmission of the probe through the plasmonic resonance.

3.2 Experiment

3.2.1 Molecular Beam Epitaxy Growth

Molecular beam epitaxy is an ultra-high vacuum method which allows for the precise deposition of high-purity crystalline material. During deposition the vacuum chamber background pressure is on the order of 10^{-10} torr. This allows for deposition rates of 1 atomic layer per second or less without worry of incorporating significant impurities. These low pressures are reached through a combination of ion pumps, titanium sublimation pumps, and liquid nitrogen filled cryo-panels. Elemental materials (e.g. indium, gallium, aluminum) are held in ceramic crucibles with PID controlled temperatures stable to less than 0.1°C. The temperature in turn controls the deposition rate which is directly proportional to the vapor pressure of the material. Mechanical shutters in front of each crucible allow for the deposition of any combination of the available materials. As a special case, arsenic, which sublimates at low temperatures, is held in a reservoir at a constant temperature. A valve, with micro-meter control, on the reservoir sets the desired flux of arsenic.

For the deposition of III-V semiconductor materials one deposits at least two materials (e.g. gallium and arsenic) which must combine stoichiometrically at the substrate surface. This is accomplished through a three temperature method, where the substrate temperature is held between the temperature of the two materials being deposited ($T_1 < T_{subs} < T_2$). As an example, let's look at the deposition of GaAs. The optimal substrate temperature in this case is ∼600°C. At this temperature arsenic will not stick to the substrate unless it encounters a free gallium atom. On the other hand, gallium will stick to the substrate and if there is not enough arsenic it will accumulate as metallic gallium. Therefore, one must supply an excess of arsenic. In this situation every gallium atom that arrives at the surface will find an arsenic atom, and excess arsenic atoms will simply evaporate from the substrate. This results in the stoichiometric growth of a GaAs film, where the deposition rate is determined only by the rate of incoming gallium atoms.

This method can also be used to deposit ternary or quaternary compounds; however, the deposition rate will be determined by the total flux of group-III atoms that arrive at the surface. Additionally, group-III materials which have higher vapor pressures (i.e. indium)

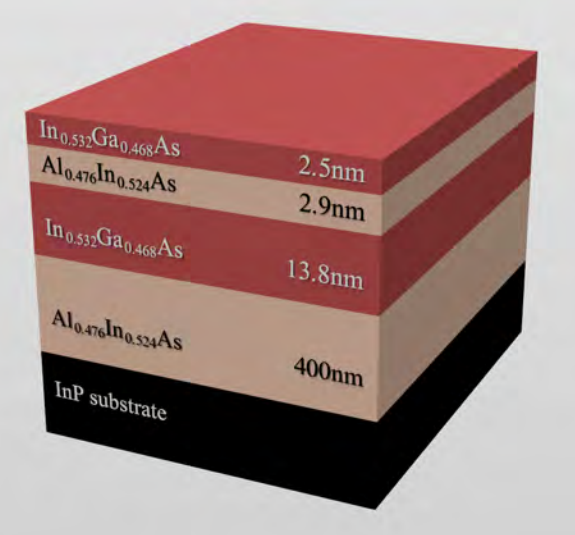

Figure 3.5: Schematic of the near-surface well structure used in this work.

may require a lower substrate temperature in order to ensure that all arriving atoms 'stick' to the substrate.

The quantum well structure used for this work is depicted in fig. 3.5. It is grown on an InP substrate. In order to be lattice matched to InP ($a = 5.87$Å) we must use the ternary materials $In_{0.532}Ga_{0.468}As$ and $In_{0.524}Al_{0.476}As$. An $In_{0.524}Al_{0.476}As$ buffer of 400+ nm is first grown to provide a smooth surface for the quantum well. This layer also serves as the lower potential barrier of the quantum well. The quantum well consists of 13.8 nm of $In_{0.532}Ga_{0.468}As$. The top barrier of $In_{0.524}Al_{0.476}As$ is only 2.9 nm thick. A final cap layer of 2.5 nm of $In_{0.532}Ga_{0.468}As$ protects the easily oxidized aluminum content of the top barrier.

Several samples with the structure of fig. 3.5 have been grown, either in the Riber 32 MBE system in Tucson, AZ (fig. 3.6a) or in the Riber 412 MBE system at the Laboratory for Analysis and Architecture of Systems (LAAS-CNRS) in Toulouse, France (fig. 3.6b). The first sample of this type, HSG37, was grown in Tucson. Attempts to reproduce this sample, (HSG39-43, 64, 68, 69) were unsuccessful, producing low quantum efficiency. One of the difficult aspects of this sample growth is that the composition of the ternary compounds ($In_{0.532}Ga_{0.468}As$ and $In_{0.524}Al_{0.476}As$) must be very precise to avoid strain in the deposited layer. We expected this to be the reason that we were unable to reproduce HSG37.

During the spring of 2013 we began a collaboration with Dr. Alexandre Arnoult of

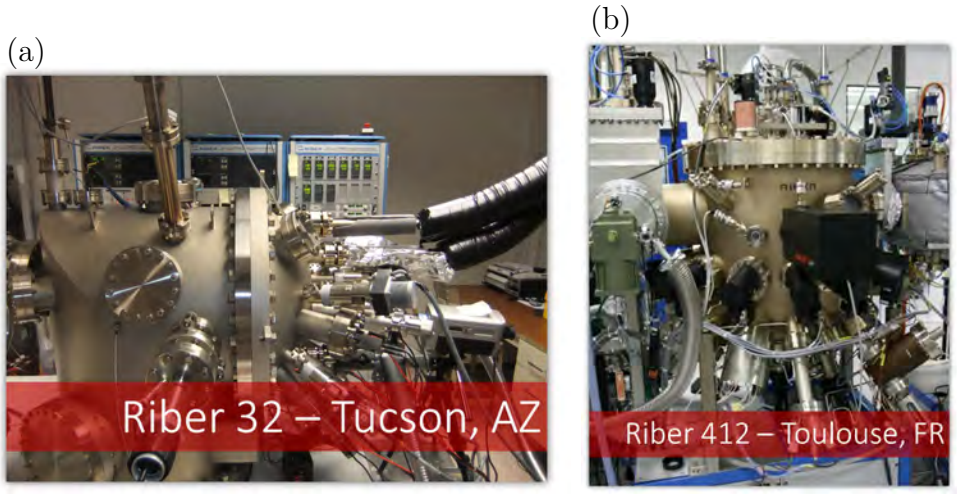

Figure 3.6: (a) Riber 32 MBE chamber in Tucson, AZ and (b) Riber 412 MBE chamber in Toulouse, France

LAAS-CNRS, and I spent slightly over a week working with Dr. Arnoult, using his state-of-the-art Riber 412 MBE system to grow samples. Dr. Arnoult had the capability to perform high-resolution x-ray diffration (HRXRD) on samples immediately following growth. This provided immediate feedback on the relative concentration of the $In_xAl_{1-x}As$ buffer layer, which allowed us to correct the growth parameters and improve the lattice matching through multiple iterations. Figure 3.7a shows $\Omega - 2\Theta$ curves for the samples grown in France, as well as one from Tucson (HSG64). The InP substrate produces a narrow intense diffraction peak at 63.338°, while the $In_xAl_{1-x}As$ buffer produces a less intense peak, with a diffraction angle determined by the concentration x. Fringes in the diffraction pattern provide information on the thickness of the buffer layer, but only appear if the interfaces between layers are atomically smooth. We see then that sample A111 has the best lattice matching (the substrate and buffer layer peaks overlap), however, this sample shows no fringes meaning the sample potentially has rough interfaces.

Figure 3.7b shows the low-temperature, low-pump-power PL measured from each of the samples in fig. 3.7a, as well as from the target sample (HSG37). From this we can clearly see that HSG64 (the Tucson attempt to reproduce HSG37) is significantly less efficient. Sample A106, which was poorly lattice matched, showed similarly low PL. All three of the other samples grown in France (A107, A109 and A111) showed more PL than HSG37, with A107 being the brightest. Figure 3.8a shows a plot of the peak PL intensity of these samples as a

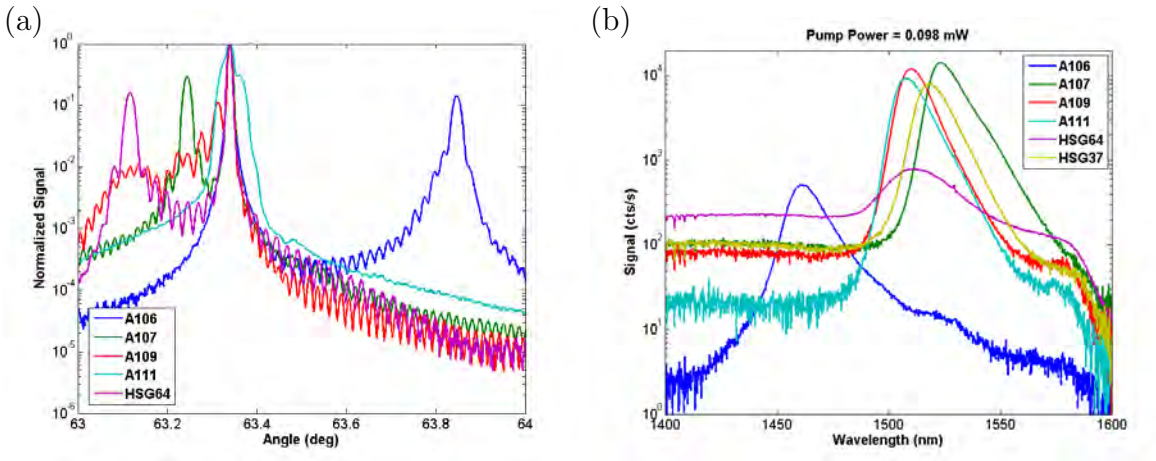

Figure 3.7: (a) High resolution x-ray diffraction measurements of several quantum well samples and (b) low-temperature, low-pump-power PL measurements.

function of the calculated lattice mismatch, while fig. 3.8b shows the peak wavelength. A107 was determined to be the highest efficiency QW and was therefore used for the work on the comparison of antenna geometries [32]. Several examples of data from HSG64, which was measured prior to the growth of the French samples, will also be presented.

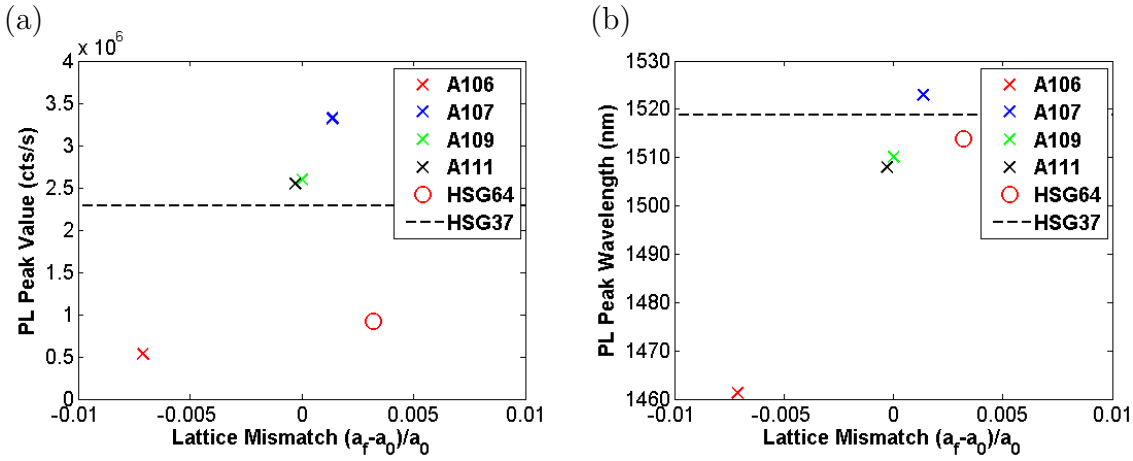

Figure 3.8: Low-temperature, low-pump-power PL intensity (a) and wavelength (b) as a function of lattice mismatch.

3.2.2 Nano-Fabrication

Fabrication of metallic structures was done using electron beam lithography, metal deposition and a lift-off process as illustrated in fig. 3.9. Exact details of the fabrication procedure are

presented here for reference.

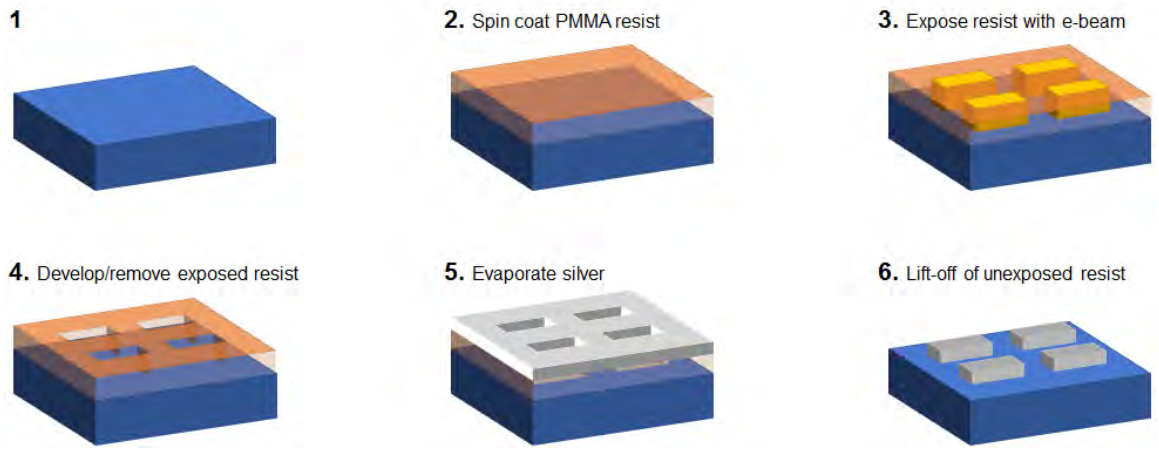

Figure 3.9: Illustration of the fabrication process. A clean substrate (1) is coated with a thin layer of resist (2). The desired pattern is written into the resist using EBL (3) and then developed (4). After depositing a layer of silver (5) the sample is placed in a solvent which dissolves the resist and removes the excess silver (6).

Substrate De-Oxidation (Optional) For the samples presented in this dissertation de-oxidation was never necessary. However, for some substrates this is a required step. During the MBE growth process the native oxide is thermally removed and pure semiconductor material is deposited. When the sample is removed from the MBE chamber the surface begins to form a new oxide layer. If the sample has been recently removed from the MBE chamber this oxide layer will be relatively thin and will not create any issues for the fabrication process. However, old samples, or substrates which have not been thermally de-oxidized will have a significant oxide layer which can interfere with fabrication. This is most noticable for GaAs and silicon. Oxidation on GaAs can be removed using a brief ($\sim$1 min) dip in concentrated HCl acid followed by a thorough rinse in de-ionized (DI) water. Oxidation on Si is removed using a 3 min dip in 1% HF acid followed by a thorough rinse in DI water.

Substrate Cleaning Samples that are recently removed from the MBE chamber have a very clean surface and may not require a cleaning step. Samples which have been in storage for some time, or samples which have been cleaved may have dust or other contaminates on the surface which must be removed prior to spin coating. To clean the substrate one places

the sample in a series of ultra-sonic baths. Preferably a PTFE beaker is used to prevent breaking the substrate. The baths are, in order, acetone, methanol, and isopropanol (IPA). Sonication for 5 minutes each is generally sufficient, but times may be altered base on the level of contamination.

Resist Spinning There are many recipes for resist depending on the necessary resolution and thickness of deposited metal. For the structures in this work we require very high resolution (<50 nm linewidth) and only deposit ∼30 nm of metal. Therefore we use a single ∼200 nm layer of resist (MicroChem 950PMMA-A4). This resist has a high molecular weight, making it less soluble which provides a higher development contrast between exposed and unexposed regions. Using a syringe with a 0.2 μm filter, the resist is dispensed onto the substrate. The substrate is then spun at 4000 rpm for 45 s, followed by a pre-bake on a hot-plate at 180°C for 60-90 s.

To do lift-off with thicker metal layers it may be necessary to apply two or more layers of resist. Additionally, using a lower resolution resist for the bottom layer will provide an undercut to the developed pattern which allows for a cleaner lift-off.

Electron Beam Lithography Electron beam lithography was performed with an Elionix ELS-7000 system operating at 100 keV. In order to achieve high resolution the electron beam passes through a 30 μm aperture, and the beam current is set to 100 pA. This is expected to result in a spot size of less than 5 nm. The patterns are exposed as a series of spots on a grid. The grid is 150 μm x 150 μm with 60,000 x 60,000 spots. The exposure dose is a complex function of the exact geometry and feature size of the pattern being written and must be determined through trial and error. The small feature size of the optical antennas requires a very high dose on the order of 1500 - 5000 μC/cm^2 for squares and 7000 - 50000 μC/cm^2 for split-ring and dipole shaped antennas.

Antennas were written in dense arrays which covered an area of 100 μm x 100 μm. A grid of 12 x 10 of these patterns were written. For each of the 12 rows some parameter (shape, length, width, etc...) was varied. For each of the 10 columns the electron beam dose was varied. Higher doses lead to increased exposure of the resist and larger feature sizes which effectively tunes the antenna resonance.

Development After the pattern is written into the resist it must be developed. This is accomplished using a 1:3 mixture of methyl isobutyl ketone:isopropanol (MIBK:IPA). In order to maintain small feature sizes the development time is limited to 20 s followed by a thorough rinse in IPA. For structures where the feature size is not critical, a longer development time of 40 s will provide for a cleaner development and tends to improve adhesion of metal films. Following the IPA rinse the sample is blown dry with N_2 and then placed on a 100°C hot-plate for 60 s.

Metal Deposition Deposition of metal can be accomplished by several techniques, including thermal, electron beam, and sputtering. For this work all deposition was done by electron beam deposition. Following development, samples are attached to a glass slide using double sided Kapton tape. The glass slide is then clamped to the sample mount and placed at the upper position of a BOC Edwards Auto 306 deposition chamber. High purity silver (99.995%) in a molybdenum crucible is loaded into the hearth. The chamber is cycled and allowed to pump down for at least 3 hours. The base pressure after this time is on the order of 1×10^{-6} mbar. Silver is then deposited at a rate of ∼1-2 Å/s until a thickness of 30 nm is reached.

Lift-Off The final step of the fabrication process is to remove the resist and excess metal. The sample is placed in a bath of MicroChem PG Remover held at 50-80°C. For 30 nm films of silver the resist will typically dissolve in less than 20 min, and the silver can be seen lifting off of the sample. For thicker films, or different metals, the resist may take longer to dissolve. Once it is clear that the resist has completely dissolved the sample can be removed from the bath. The sample should be rinsed with IPA as it is removed from the bath in order to prevent metal particles from settling on the sample. The sample should be rinsed thoroughly in IPA and then blown dry with N_2.

Characterization Following fabrication samples are characterized by scanning electron microscopy (SEM) and Fourier transform infra-red (FTIR) spectroscopy in order to determine if the dimensions and resonance wavelength meet specifications. Figure 3.10 shows SEM images of several dipole antenna arrays along with FTIR transmission measurements. SEM

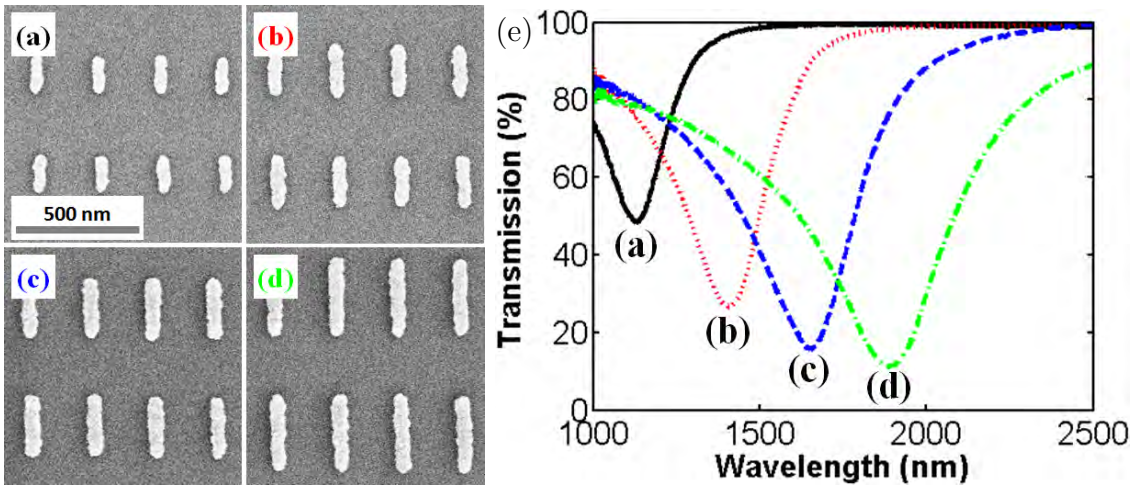

Figure 3.10: (a-d) SEM images of several dipole antenna arrays and (e) corresponding FTIR measurements showing the shift in resonance wavelength.

images are collected using the Elionix ELS-7000 EBL system, while FTIR measurements are conducted with a Bruker Vertex 80v with Hyperion 2000 IR microscope located at Air Force Research Labs at Wright-Patterson Air Force Base. There is some indication that SEM imaging of the metallic resonators can alter the resonances so some care should be taken when collecting images. If possible optical measurements (FTIR, pump-probe, etc.) should be performed before collecting SEM images.

3.2.3 Transient Pump-Probe Measurement

Finding a quantitative measure of the coupling between the quantum well and the metallic antennas was accomplished using a transient differential transmission measurement. A schematic of the experimental setup used is depicted in fig. 3.11. The experiment was based around a Spectra-Physics Tsunami Ti:Sapphire laser system, which was tuned to produce $\sim$ 120 fs pulses at a center wavelength of 810 nm. This laser was directed into a Spectra-Physics Opal Optical Parametric Oscillator (OPO) which produced a probe pulse which was tunable in wavelength from 1350 nm to 1600 nm.

Approximately 120 mW of the original Ti:Sapphire pump reflected off of the Opal crystal and was collimated and passed out of an aperture on the back of the Opal to be used as a pump. The pump pulse was passed through an adjustable telescope which decreased the

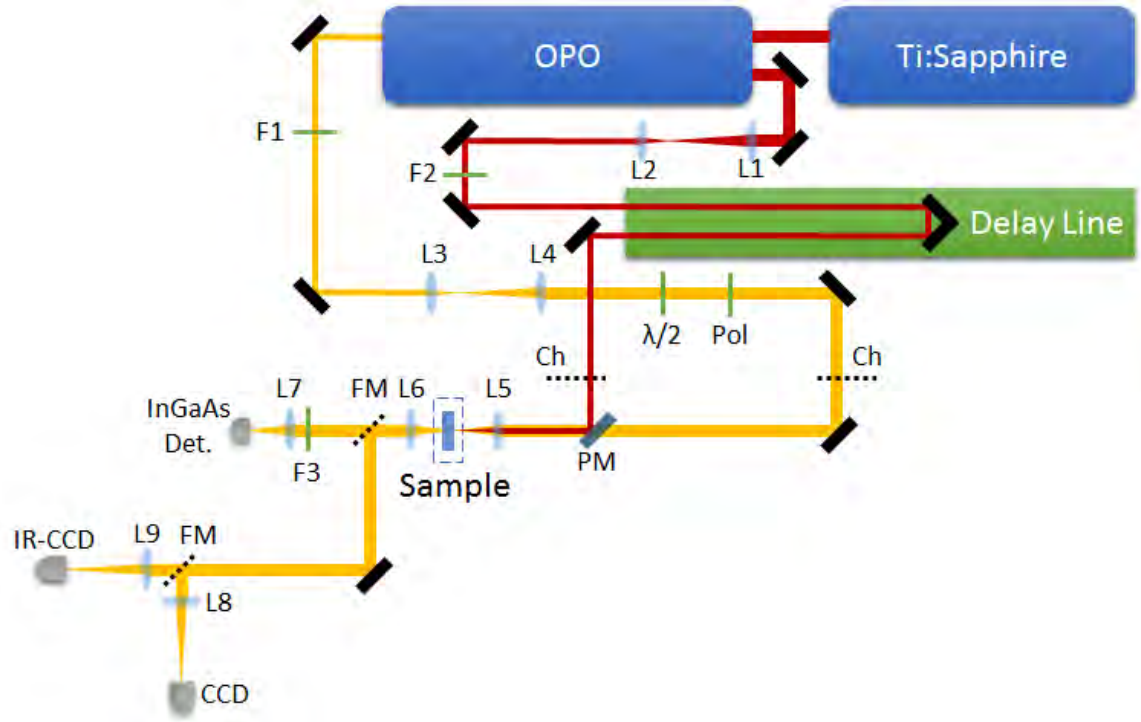

Figure 3.11: Schematic of the differential transmission measurement experiment which derives a pump-pulse (red) from the Ti:Sapphire laser and a probe-pulse (yellow) from an optical parametric oscillator (OPO). (L - Lenses [L1 = 150 mm, L2 = 50 mm, L3 = 35 mm, L4 = 100 mm, L5 = 50 mm, L6 = 50 mm, L7 = 25 mm, L8 = 200 mm, L9 = 200 mm], F - Filters [F1 = Neutral Density, F2 = Variable Neutral Density, F3 = RG1000], PM - Pick-up Mirror, FM - Flip Mirror, Pol - Polarizer, Ch - Chopper)

beam width by a factor of 3 ($f_1 = 150$ mm, $f_2 = 50$ mm), before being reflected off of a corner cube on a variable delay line (Daedal Linear Stage, 1 m of travel). A variable attenuator (Thorlabs Model NDC-100C-4) allowed the pump power to be varied over four orders of magnitude.

The probe pulse from the OPO was also passed through a variable telescope which increased the beam width by a factor of 2.86 ($f_3 = 35$ mm, $f_4 = 100$ mm). A Berek variable waveplate (Newport Model 5540) acted as a $\lambda/2$ waveplate in order to rotate the polarization of the probe pulse. A Glan-Taylor polarizer (Thorlabs Model GT15) was placed after the Berek waveplate in order to produce a clean linearly polarized beam. The combination of $\lambda/2$ waveplate and polarizer also functioned as a variable attenuator, allowing fine tuning to maintain a constant probe power as the wavelength of the OPO was varied (15 μW of probe

power was typically used).

The pump and probe beams were combined using a dichroic beamsplitter (Semrock Model LP02-980RE-25) which allowed the probe to pass through while reflecting the pump. The two beams were aligned co-linearly and focused on to the sample using a 50 mm focal length lens. The sample was held at 10 K in a continuous-flow liquid helium cryostat (Oxford Instruments Model Microstat He2). The sample was rotated such that the pump and probe beams were incident at an angle of approximately 13°. This was the minimum angle required so that the reflection of the probe beam off of the back side of the sample would be displaced and not return to the original pumped spot on the front of the sample. On the back side of the sample the two beams were collimated using an identical lens. Most of the pump beam is absorbed by the sample, however, the measurement is very sensitive so an additional filter (Schott RG1000) is used to block any stray 810 nm light. The probe beam is then focused onto an InGaAs detector (Thorlabs Model PDA10CS) using a 25 mm focal length lens. Prior to data collection a knife edge experiment was constructed which used the same focusing lens in order to measure the spot sizes of both the pump and probe beams. The adjustable telescopes are intended to adjust the beam widths which in turn adjusts the focused spot size (which is proportional to $\lambda f/D$). Additionally, the telescopes allow one to adjust the relative divergence which is needed to correct for the different focal lengths at the wavelengths of the pump and probe. Ideally, the pump spot size should be much larger than the probe spot size, to ensure that the probe is measuring a uniformly pumped region. In reality, the spot sizes change with both delay line position and with the probe wavelength, so it is useful to keep the pump beam slightly de-focused such that small changes in either spot size do not make significant changes to the measured signal. The spot size of the probe beam was typically 10 μm in diameter, while the pump spot size was 20 μm.

The transmission signal is measured using a lock-in amplifier (Stanford Research Systems Model 830) connected to the InGaAs detector. A chopper is placed in both the pump and the probe beam paths. If the probe beam chopper is turned on the lock-in amplifier detects a voltage which is directly proportional to the absolute transmission of the probe through the sample. If the pump beam chopper is turned on the lock-in amplifier detects a voltage which is directly proportional to the change in probe transmission that results from the presence of

the pump beam. Taking the ratio of these two voltages provides the normalized differential transmission $\Delta T/T$.

A mirror can be flipped into place in front of the detector, which directs light to a system of two imaging cameras, one silicon camera which allows imaging from visible wavelengths out to 1100 nm in wavelength and a second silicon camera treated with a phosphor coating which allows imaging of the probe beam. A tungsten lamp illuminates the front of the sample allowing it to be imaged in transmission. Antenna arrays which scatter light show up as shadows on the sample. Due to the large difference in wavelength of the pump and probe beams the imaging setup can only be used as a rough guide to align the overlap of the pump and probe beams. The overlap must then be fine-tuned by making adjustments to maximize the differential transmission signal.

To illustrate exactly what is being measured by a differential transmission measurement, several plots are shown in fig. 3.12 which use the model of sec. 3.1.3 to illustrate the measurement. In fig. 3.12a we see the absolute transmission of the two separate resonances, the quantum well in blue and the antenna array in red. When coupling is introduced ($L \neq 0$) we see the combined lineshape of fig. 3.12b. In this case the quantum well is relaxed ($f = 0$), and the coupling constant is chosen to be sufficiently large so that the change in lineshape is obvious (in actual data presented later this change is much smaller). When the quantum well is pumped ($f = 1$) we see a change in the lineshape to that in fig. 3.12c. Finally, the transmission lineshapes are overlaid in fig. 3.12d so that we can see the change in transmission (ΔT). We see that ΔT becomes negative near the resonance, meaning the transmission drops, while it is positive to the side of the resonance. The signal measured in the experiment is this ΔT normalized by the un-pumped transmission T (fig. 3.12b).

3.3 Results

3.3.1 Quantum Well Characterization

Before measuring the coupled system it's important to understand the behavior of the quantum well by itself. Figure 3.13 shows the low-temperature photo-luminescence of sample HSG64, measured in the same configuration as the pump-probe experiment described above,

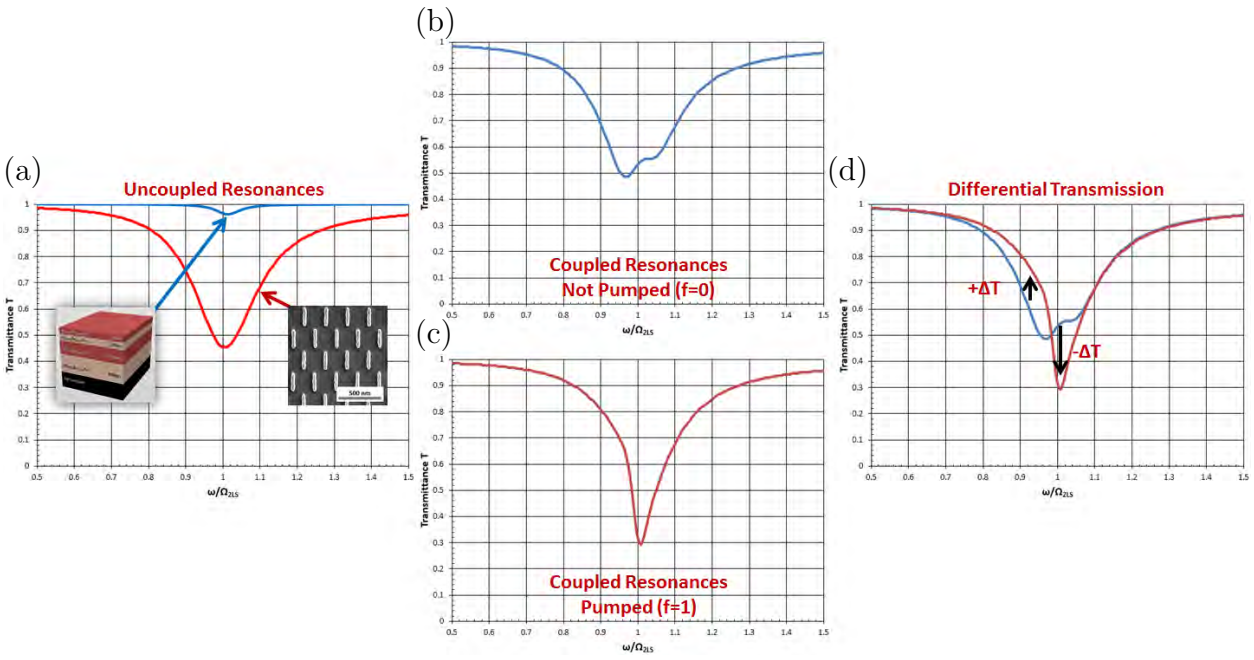

Figure 3.12: Plots generated using the coupled oscillator model (sec. 3.1.3), showing (a) the uncoupled transmission resonances of the quantum well and antenna array, (b) the coupled transmission line-shape when the quantum well is relaxed, (c) the same as (b) with the quantum well inverted, and (d) an overlay of (b) and (c) demonstrating the differential transmission is expected to be negative on resonance.

for various pump powers. We see that at low powers (<12.5 mW) there is only a single peak, corresponding to the lowest energy transition (e1→hh1) of the quantum well. As the pump power is increased further charge carriers begin to fill up the e1 and hh1 levels faster than the carriers can recombine. As a result charge carriers begin to accumulate in higher energy levels, and we start to see additional peaks in emission. At 12.5 mW we start to see a second transition peak (e2→hh2) around 1360 nm, and at 50 mW we start to see a third peak (e3→hh3) around 1200 nm.

Similarly, we can take transient pump-probe measurements of the quantum well at various pump powers. Figure 3.14 shows differential transmission measurements of HSG64 with the probe wavelength fixed near the peak signal at 1480 nm. At low pump powers we notice a purely exponential decay (fit by the dotted lines) of the signal. This exponential decay depends on the pump power, with a decay of 82 ps at 100 μW, increasing to 212 ps for 100 mW. The magnitude of the peak $\Delta T/T$ signal increases linearly with pump power up to about the 3.12 mW trace. At this point we notice a shoulder develop, where there is a

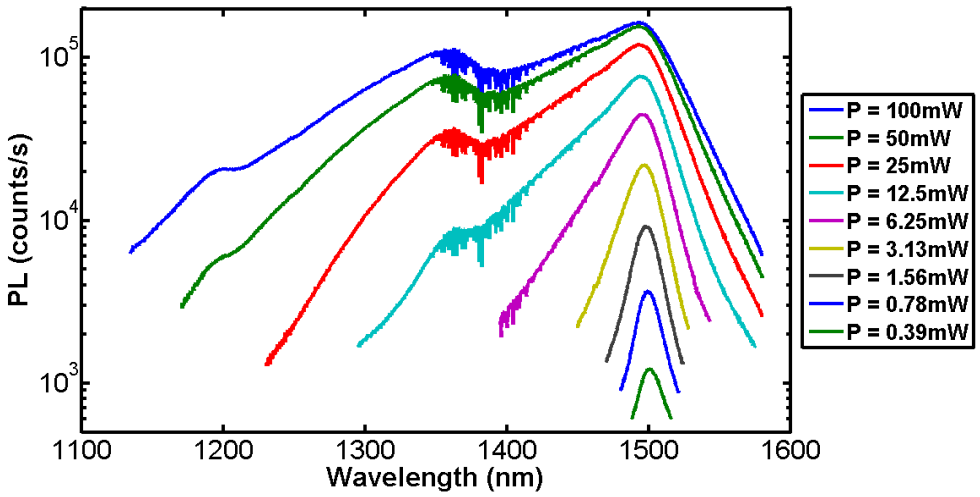

Figure 3.13: Low-temperature photo-luminescence of sample HSG64, a sample grown in Tucson, for various pump-powers.

slower initial decay, followed by a nearly exponential decay. This is attributed to saturation of the lowest energy transition. Following the initial pump pulse a large number of hot (high energy) carriers are generated. These carriers quickly relax through electron-electron and electron-phonon scattering processes. If there are enough carriers the lowest energy transition will be completely filled and charges will start to fill higher energy levels. It's important to note that the probe pulse is fixed at 1480 nm and is therefore only probing the inversion of the e1→hh1 transition. Once this transition is inverted, adding more carriers will begin to invert other transitions at higher energies, but there should be no increase in the peak differential transmission at 1480 nm. It will, however, affect the decay characteristics at this wavelength. As charge carriers recombine via this transition we expect the differential transmission signal to decay. However, if there are carriers in higher energy levels, they can scatter down to replenish the lowest energy levels. This scattering happens on time scales of a few ps, much faster than carrier recombination. As a result, we see this shoulder appear where the inversion of the e1→hh1 transition is being maintained by carriers relaxing from other levels. Once the higher energy levels are depleted of carriers, the signal once again begins to decay exponentially.

We notice that this shoulder appears between the 3.12 mW and 6.25 mW pump power traces, and for later data we take a value of 4 mW as the power needed to invert the e1→hh1

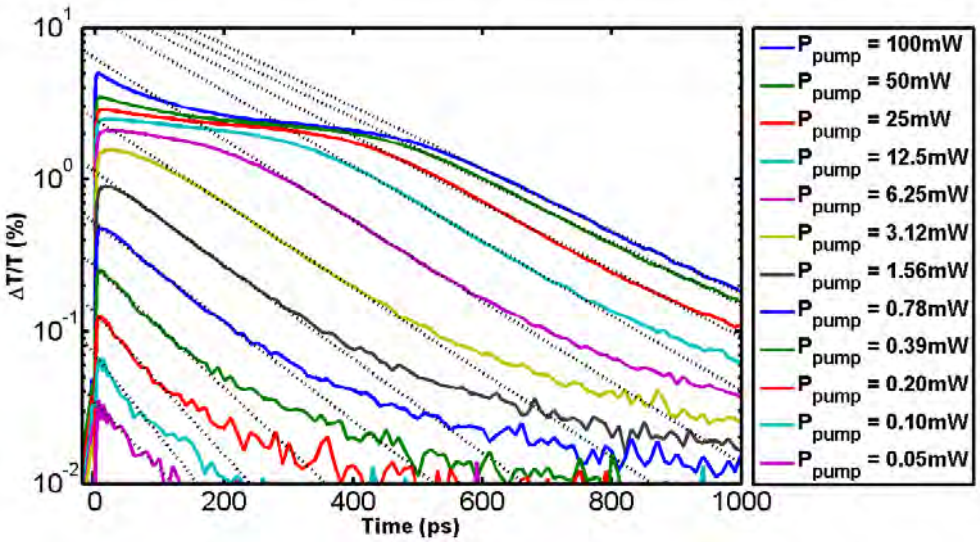

Figure 3.14: Differential transmission measurements of HSG64, for a fixed probe wavelength of 1480nm, as pump-power is increased from 50 μW to 100 mW. Dotted lines are exponential fits to the final decay of the signal.

transition. It is interesting to see that the peak differential transmission signal has a value of approximately 2% at this point. This is in good agreement with the expected value. The absorption of a single quantum well is expected to be on the order of 10^4 /cm. This roughly translates to a 1% transmission dip. Likewise, when the quantum well is inverted it will provide approximately 1% gain. Therefore the total differential transmission signal will be 2%.

Surprisingly, when we look at fig. 3.14, we notice that if we continue to increase the pump power, past the initial saturation, the peak differential transmission once again begins to rise. In fact it reaches more than 5% at 100 mW pump power. Clearly this can not be from the quantum well, so instead we must attribute this to the substrate. Measurements of an InP substrate, as well as a structure similar to HSG64 but without the InGaAs quantum well layer, revealed ∼3% differential transmission at a pump power of 100 mW which was for the most part independent of the probe wavelength. This is consistent with our understanding that the quantum well adds 2% to this signal to reach the 5% seen on HSG64.

The most likely explanation for this signal is a change in the refractive index of the substrate resulting from a pile-up of free carriers. If we do a quick back of the envelope

calculation we see that it takes a change in refractive index on the order of -0.1 to create a 3% change in transmission. Both the sign and magnitude of this change are consistent with theoretical calculations of band-filling effects [55] for a charge carrier concentration on the order of 10^{19} /cm^3. Estimating the absorption of InP/AlGaAs to be 10^4 /cm and given a pump spot diameter of 20 μm, 100 mW should generate $\sim 1.7\times10^{19}$ /cm^3 carriers, consistent with the necessary concentration required to create this change in refractive index.

With a better understanding of the quantum well, it becomes clear that the pump power must be limited. We definitely do not want to introduce spurious signals from the substrate, but we also do not want charge carriers to begin building up in higher energy levels of the quantum well. The coupled oscillator model treats the quantum well as a single two-level system, and therefore we only want to observe differential transmission associated with the inversion of the e1→hh1 transition. Therefore, when using this model, the pump power is limited to 4 mW. With this in mind we can now vary the probe wavelength and measure the peak differential transmission signal spectrum, an example of which can be seen in fig. 3.4a for quantum well HSG64.

3.3.2 Coupled System Characterization

With the quantum well characterized we can now begin to understand the differential transmission measurements from a coupled QW/antenna structure. Initial investigations were done over a range of pump powers, all the way to the maximum available power (120-130 mW), which revealed some very interesting features. In fig. 3.15a we see the differential transmission spectrum of quantum well HSG64 alone for various pump-powers. For low power we see a single peak associated with the e1→hh1 transition, and at 120 mW we see the entire spectrum shifted up ∼3% due to the substrate. Figure 3.15b shows the same measurements done on an array of dipole shaped antennas. We see the expected negative $\Delta T/T$ signal near resonance; however, at 120 mW we see a very large magnitude of nearly -12% and an unexpected splitting of the spectrum appears around 1540 nm. If we want to have any hope of quantifying the coupling we must restrict ourselves to a pump-power of 4 mW which allows the data to be fit to the coupled oscillator model as in fig. 3.16.

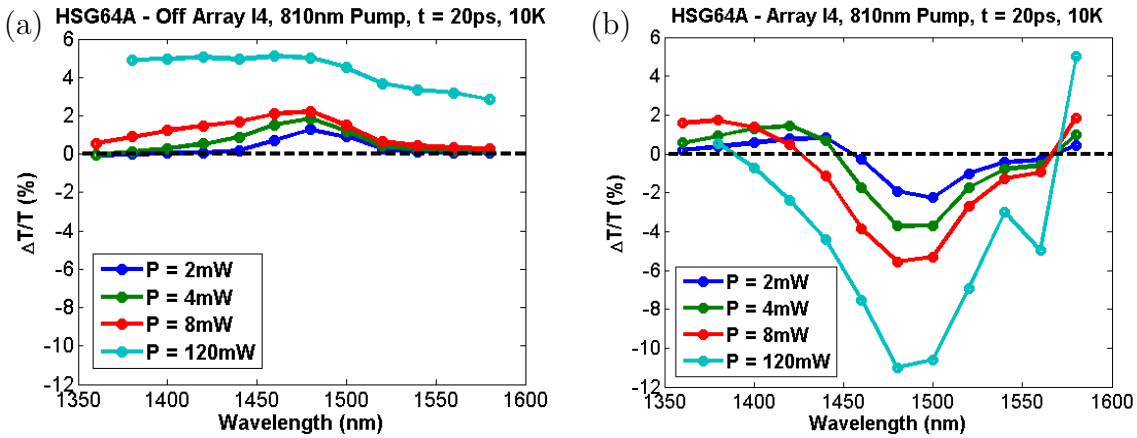

Figure 3.15: Differential transmission spectra at several pump-powers both off (a) and on (b) an array of dipole antennas.

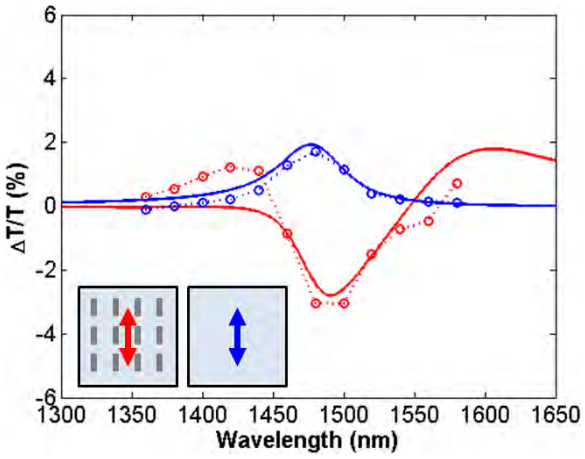

Figure 3.16: Differential transmission spectra at 4 mW pump power from fig. 3.15 fit to the coupled oscillator model in order to quantify the coupling constant.

3.3.3 Comparison of Antenna Shape

As explained in the introduction, the dipole moment, and therefore the radiative coupling, can be controlled by the shape of the antenna. As the coupling between quantum well and antenna is a result of a dipole-dipole interaction we were naturally curious to see how the shape of the individual antennas changes the observed coupling to a quantum well. To explore this idea I fabricated arrays of dipole (fig. 3.10a), square (fig. 3.10b), and split-ring (fig. 3.10c) shaped antennas on the same piece of quantum well (A107). The dipole moment of individual antennas with the same shapes were measured by our collaborators

in Karlsruhe [26], and it was found that the square antenna had the largest dipole moment, while split-rings have the smallest and dipole antennas were in the middle. This same trend was observed in the arrays of antennas fabricated on A107. The dipole moment (d_{PL}), as well as the resonance frequency (Ω_{PL}) and damping frequency (γ_{PL}), was determined by measuring the absolute transmission of the antenna arrays and fitting to the oscillator model. Surprisingly, the damping frequency was very similar for each of the arrays. This is attributed to interactions between the densely packed antennas which leads to an increased damping relative to a single antenna.

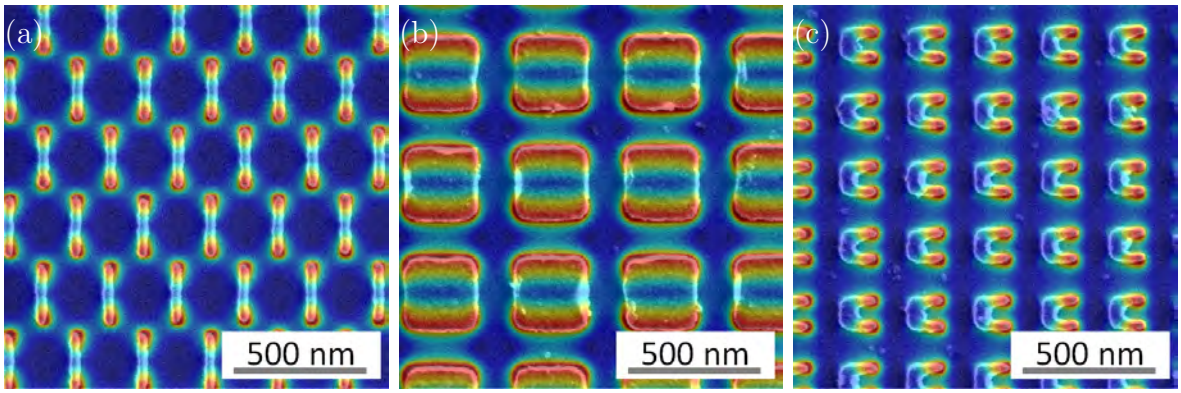

Figure 3.17: SEM images of (a) dipole, (b) square and (c) split-ring antennas, along with an overlay of the simulated electric field distribution of each antenna.

Figure 3.18 shows the measured differential transmission spectra of each of the arrays from fig. 3.17 both on the array (red) and from the quantum well alone, directly next to the array (blue). The quantum well data is fit in order to retrieve the resonance frequency (Ω_{QW}), damping frequency (γ_{QW}) and dipole moment (d_{QW}). The on-array data is then fit by varying only the coupling constant L. Table 3.1 summarizes all of the parameters of the fit data. Also listed in this table is the effective coupling frequency (V_{eff}) which accounts for the density and dipole moment of the two oscillators. The primary conclusion of this data is that the split-ring resonator, despite having the smallest dipole moment, displays the largest coupling (L) and effective coupling (V_{eff}). This was surprising given the much smaller dipole moment.

This result is understood by considering the meaning of the coupling constant (L). This constant is essentially a measure of the magnitude of the mode distribution at the location

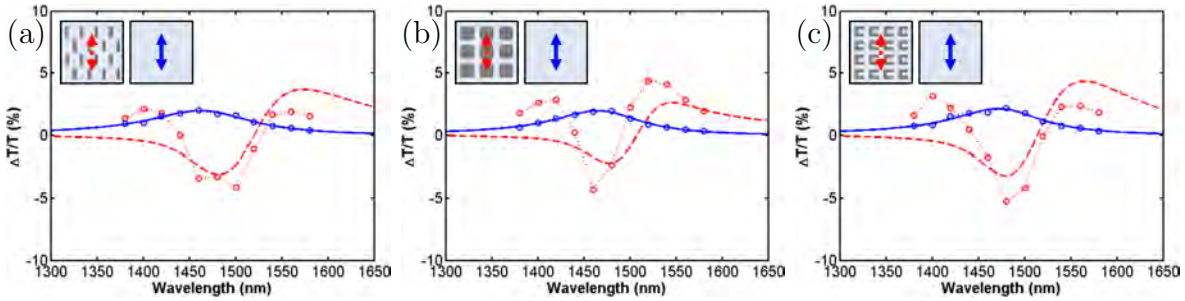

Figure 3.18: Differential transmission spectrum and model fit of (a) dipole, (b) square and (c) split-ring antennas (red data). Blue data is measured from the quantum well directly next to each array.

of the quantum well. In other words it can be considered a measure of the local density of optical states (LDOS). As one moves away from the antenna, the magnitude of the mode distribution, as well as the LDOS, falls off approximately exponentially [56]. Likewise, we expect the coupling to fall off in a similar fashion as the quantum well is moved away from the antenna. We are using an approximation by assuming that the coupling constant is independent of spatial location, but in fact the coupling constant will vary in the plane of the quantum well. This can be seen by looking at the mode distribution of the different antenna shapes shown in fig. 3.17. What we realize from this is that the split-ring antennas localize the mode to a much smaller volume, leading to a large LDOS inside of the quantum well and as a result a larger coupling constant. It seems then that there is a trade-off between dipole moment and mode-volume (coupling). As the dipole moment increases so too does the mode-volume and the coupling constant is seen to drop. In fact, if we take the product of the coupling constant and the dipole moment of each antenna array we see that the value is nearly constant. The effective coupling frequency (V_{eff}), which is a better figure of merit for the antenna array, includes this product of the dipole moment and coupling constant. Unfortunately, it also includes the square root of the dipole density. The large size of the square antennas physically limits the density of the antenna array and in the end the split-ring resonators still come out ahead.

Table 3.1: Summary of coupled oscillator parameters from fit to experimental data

	Quantum Well	Dipole Antennas	Square Antennas	Split-Ring Antennas
ω	$2\pi \times 204$ THz	$2\pi \times 197$ THz	$2\pi \times 198$ THz	$2\pi \times 198$ THz
γ	$2\pi \times 8.6$ THz	$2\pi \times 9.4$ THz	$2\pi \times 7.7$ THz	$2\pi \times 9.7$ THz
d	8.7×10^{-29} Cm	7.8×10^{-26} Cm	17×10^{-26} Cm	5.8×10^{-26} Cm
N	2.1×10^{24} m^{-3}	5.33×10^{20} m^{-3}	1.98×10^{20} m^{-3}	5.33×10^{20} m^{-3}
L	–	0.38×10^{10} m F^{-1}	0.18×10^{10} m F^{-1}	0.56×10^{10} m F^{-1}
V_{eff}	–	8.4 THz	5.0 THz	9.1 THz

Chapter 4
Future Directions

4.1 Self-Assembled Plasmonic Structures

The search for improved interaction between metallic plasmonic resonators and nearby optical emitters can go down several paths. Improving the quantum efficiency of the emitter, reducing Ohmic losses in the metal and optimizing the separation between the two are the most obvious. In section 3.3.1 I explained how the optical quality of the emitter (QW) was optimized using HRXRD and low temperature PL measurements. This resulted in increased PL meaning a greater number of electron/hole pairs recombined radiatively rather than non-radiately. The separation between the metallic structure and the QW is already nearing its minimum. Further decrease in the thickness of the capping layer of the quantum well would only reduce the quantum efficiency of the quantum well. As a result, the remaining path is the improvement of the metallic resonator.

Significant efforts have been made to improve the quality of plasmonic materials [57–59], the primary aim being to reduce ohmic losses in the wavelength range of interest. The ohmic loss is partially a property of the material, but it is also strongly influenced by the purity and morphology of the material. One would expect the lowest losses from high purity material with a crystalline structure. This naturally leads one to ask whether high purity, crystalline metal can be deposited using MBE technology. There have been several promising results in the growth of silver both as a crystalline thin film [60] and as crystalline nanoparticles [61,62]. While silver is an obvious choice due to its intrinsically low ohmic losses, it is not a common material in MBE systems. Therefore, we became interested in the materials we do have available: indium, aluminum, and gallium. We were pleasantly surprised to find that indium, much like silver, will form nano-scale particles or islands on the surface of GaAs (fig. 4.1).

Despite these islands forming through a random self-assembled process, the distribution in sizes of islands on a single sample is on the order of $\pm 10\%$. As a result one can easily

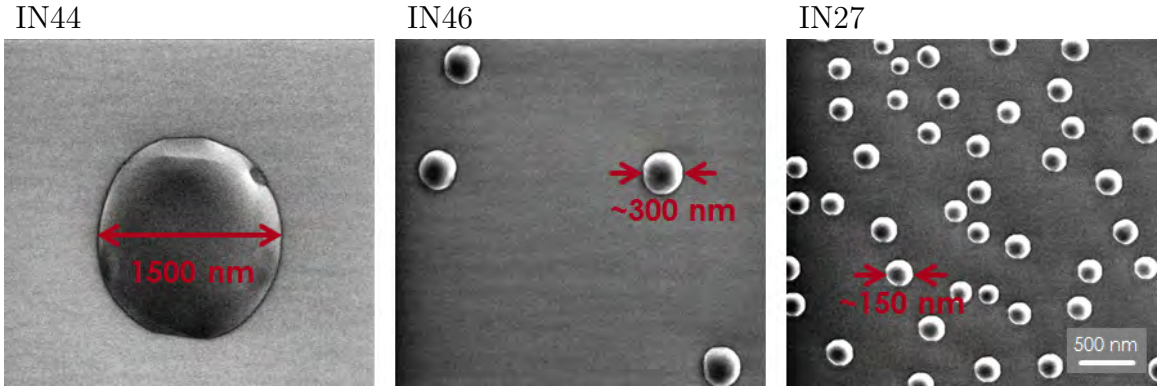

Figure 4.1: SEM images of several indium island samples with varying sizes and densities.

measure a collective plasmonic resonance from the ensemble of islands. This resonance is tunable by varying the size and density of islands through MBE growth parameters. The high purity of the deposited metal, as well as the *in situ* nature of the process are both beneficial for improving the coupling between the plasmonic resonance and the underlying semiconductor. One can imagine making many interesting devices by aligning the islands with near-surface quantum dots [61] or by controlling the placement and dimensions with pre-patterned substrates [62]. It will be highly interesting to investigate the possible active plasmonic structures that can be formed with this method of MBE growth.

4.2 Semiconductor - Superconductor Hybrid Structures

Some of the most promising candidates for qubits in quantum information science and computing schemes are currently based on superconducting circuits [63]. The robustness of superconductivity, along with the Josephson effect has allowed for a wealth of qubit systems, including the Cooper pair box, the flux qubit, and the phase qubit. Over the past decade the performance and coherence time of these qubits has continuously increased. Just recently researchers at IBM have announced the demonstration of qubits with coherence times on the order of 0.1 ms, a milestone which will soon allow the implementation of quantum error-correcting schemes [64].

At the same time, a vast majority of quantum communication proposals center on the photon as the fundamental qubit, with information encoded in properties such as the polarization, phase, or frequency [65]. The gap between stationary superconducting qubits,

useful for processing and storage, and traveling photonic qubits has been a looming concern in the field of quantum information science with very few proposed solutions to date. This is largely due to the huge energy mismatch between optical photons ($\sim$1 eV) and superconducting Cooper pairs ($\sim$1 meV). Finding a suitable system to interface between these two qubit systems will be an essential task for the realization of quantum networks which rely on both the transmission of quantum information over long distances and the processing of such information at intermediate nodes such as quantum repeaters [65].

Another limitation to the deployment of quantum networks is the ability to deterministically generate and efficiently detect both single photons and entangled photon pairs. Many schemes exist for accomplishing these tasks, but most suffer from restrictions that make them impractical. Improving on and surpassing the current methods of novel photon state generation and detection will be another pressing task in the coming years.

One promising approach to achieving both of these goals is that of the superconducting LED [66, 67]. This idea is based on the proximity effect, which allows for electrons in the conduction band of a semiconductor in contact with a superconductor to occupy a superconducting like state. This would allow for entangled electron pairs (Cooper pairs) from the superconductor to radiatively recombine with holes in the semiconductor, producing entangled photons containing quantum state information from the original electrons. This idea is still in its early stages, but observations of enhanced luminescence and shortened radiative lifetimes already support the theory behind this novel hybrid system. Improved fabrication and careful measurements will be necessary to fully realize the transfer of quantum information from superconducting electrons to photonic qubits.

4.2.1 Superconductivity in Indium Islands

Along these lines we decided to search for signs of superconductivity in a single epitaxially grown indium island. It is well known that below 3.4 K indium transitions to a superconducting state in which the many conduction electrons behave as a single coherent quantum state. It is not immediately clear that superconductivity will survive when the dimensions of the metal are reduced to the micron or nanometer scale. Surprisingly, it has been shown that superconductivity is actually enhanced in indium nano-particles with dimensions on the

order of 100 nm [68–70]. It is also important to show that superconductivity survives when the nano-particles are deposited on the surface of a semiconductor. To achieve this, electron beam lithography was used to fabricate gold electrodes onto a single indium island on the surface of a gallium arsenide substrate, as pictured in fig. 4.2.

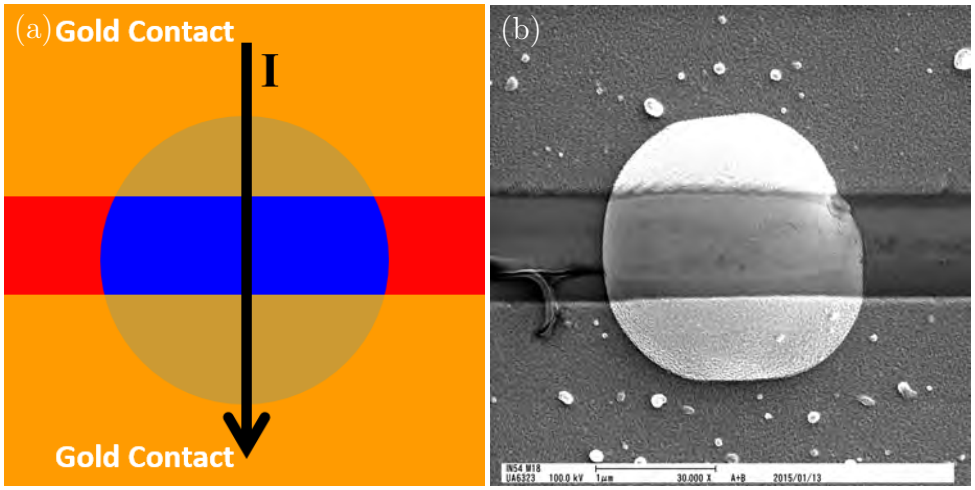

Figure 4.2: (a) Schematic of gold contacts on an indium island and (b) SEM image of the sample which was measured.

The resistance of the island was measured as the sample was cooled below the transition temperature. Figure 4.3a shows a measure of the combined island and gold electrode resistance as the sample was cooled. A clear drop in resistance was observed at 3.33 K, remarkably close to the expected transition temperature of bulk indium. As further evidence of the superconducting nature of the indium island, the differential resistance was measured (fig. 4.3b) while varying the DC current flowing through the island. At 10 K, above the superconducting transition the differential resistance was nearly constant as a function of bias current (red curve), typical of a resistive load. Below the transition temperature (blue curve, 0.4 K) new features arise. Near zero bias current there is a peak in differential resistance, a result of the gap in the electronic density of states of the superconductor. As the bias current is increased ($\pm$ 50 μA) electrons gain enough energy to begin tunneling through the superconductor as quasi-particles [71]. As the current is increased further, it eventually reaches the critical current of the superconductor, $\sim$217 μA, where superconductivity is destroyed and the island again acts as a normal resistor.

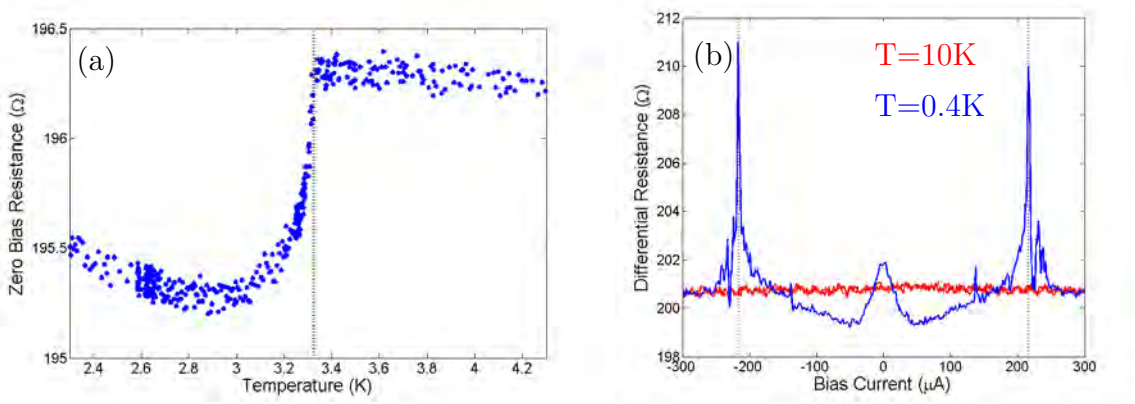

Figure 4.3: Differential resistance measurements at (a) zero-bias, showing a drop in resistance at 3.33K and (b) as a function of bias current, showing signs of a superconductivity gap and the critical current.

4.2.2 Theory

Superconductivity and Cooper Pairs While superconductivity was first observed in 1911, it was only understood empirically until 1957 when Bardeen, Cooper, and Schrieffer proposed the first microscopic theory (BCS theory) [71]. The main idea of this theory is that at low enough temperatures, any attractive potential between electrons will lead to an instability of the traditional Fermi sea, resulting in a ground state where electrons of opposite momentum pair up into Cooper pairs (fig. 4.4). This ground state is predicted to be lower in energy than the Fermi level creating a small energy gap, making it more stable and preventing the scattering of electrons into normal conducting states when the thermal energy (k_bT) is much less than that of the gap. The attractive potential between electrons is attributed to phonons, or vibrations of the atomic lattice underlying the sea of electrons. Intuitively, one can imagine an electron attracting the positively charged atomic lattice leading to a slight deformation (a phonon). This deformation will be slightly more positive than the surrounding lattice, which in turn attracts more electrons, leading to an effective interaction.

Proximity Effect The field of hybrid superconductor/semiconductor systems has been extremely active and rewarding in the past decade, primarily in the study of electrical properties of these structures [72–78]. This field of study is possible only because of the superconducting proximity effect, a phenomenon in which a non-superconducting material placed

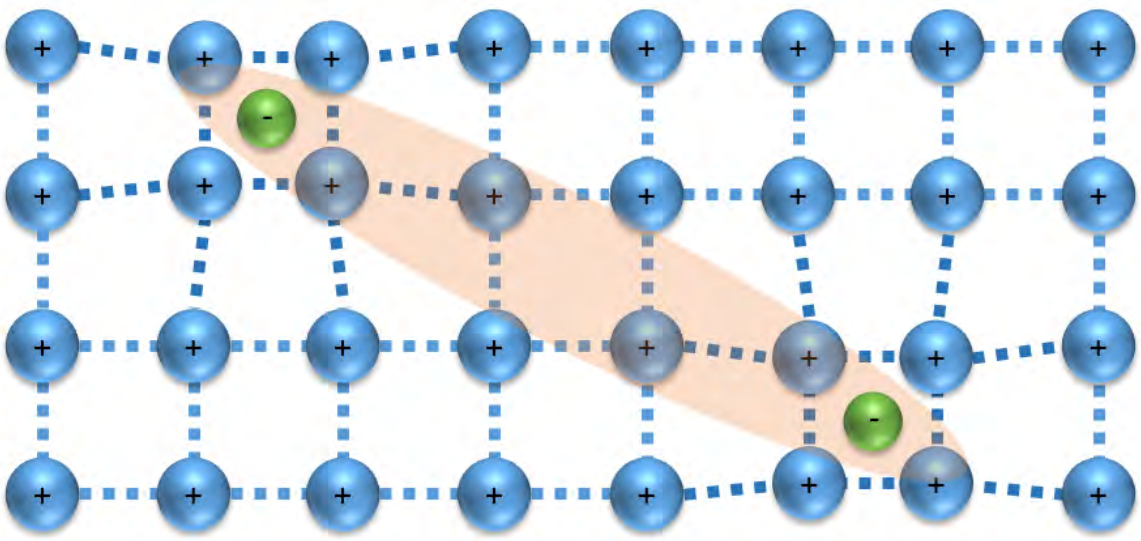

Figure 4.4: Illustration of a Cooper pair, consisting of two electrons of opposite spin and momentum bound through phonon interactions. A negatively charged electron causes a deformation of the crystal lattice (phonon), leading to a region with a slightly larger positive charge. A second electron is then attracted to this positive region.

in contact with a superconductor inherits superconducting properties over a short distance from the interface [79–83]. This effect is very strong and has been observed over distances of many microns in metals and hundreds of nanometers in graphene [84, 85] and semiconductors [86, 87]. An interesting aspect of the proximity effect is that the electronic density of states in both the semiconductor and metal are altered near the interface. Figure 4.5a illustrates the density of states of a non-superconducting material with its Fermi level (or in the case of a photo-excited semiconductor the quasi-Fermi level) in the conduction band. In figure 4.5b we see the density of states for a superconductor with a gap around the Fermi level (exaggerated for illustrative purposes). When the two materials are brought into contact, the superconductor develops new states within the normal superconducting energy gap, seen in fig. 4.5d, essentially "softening" the superconducting state. At the same time the non-superconducting material suddenly forms a gap, fig. 4.5c, in the density of states around the Fermi energy [88–91]. This gap is smaller than that of the intrinsic superconductor and decreases as one moves away from the interface, but in regions which contain this gap it is possible to pass a supercurrent, carried by correlated Cooper pairs [92–96]. This fact has enabled many of the recent works concerning Majorana fermions, which occur at the ends

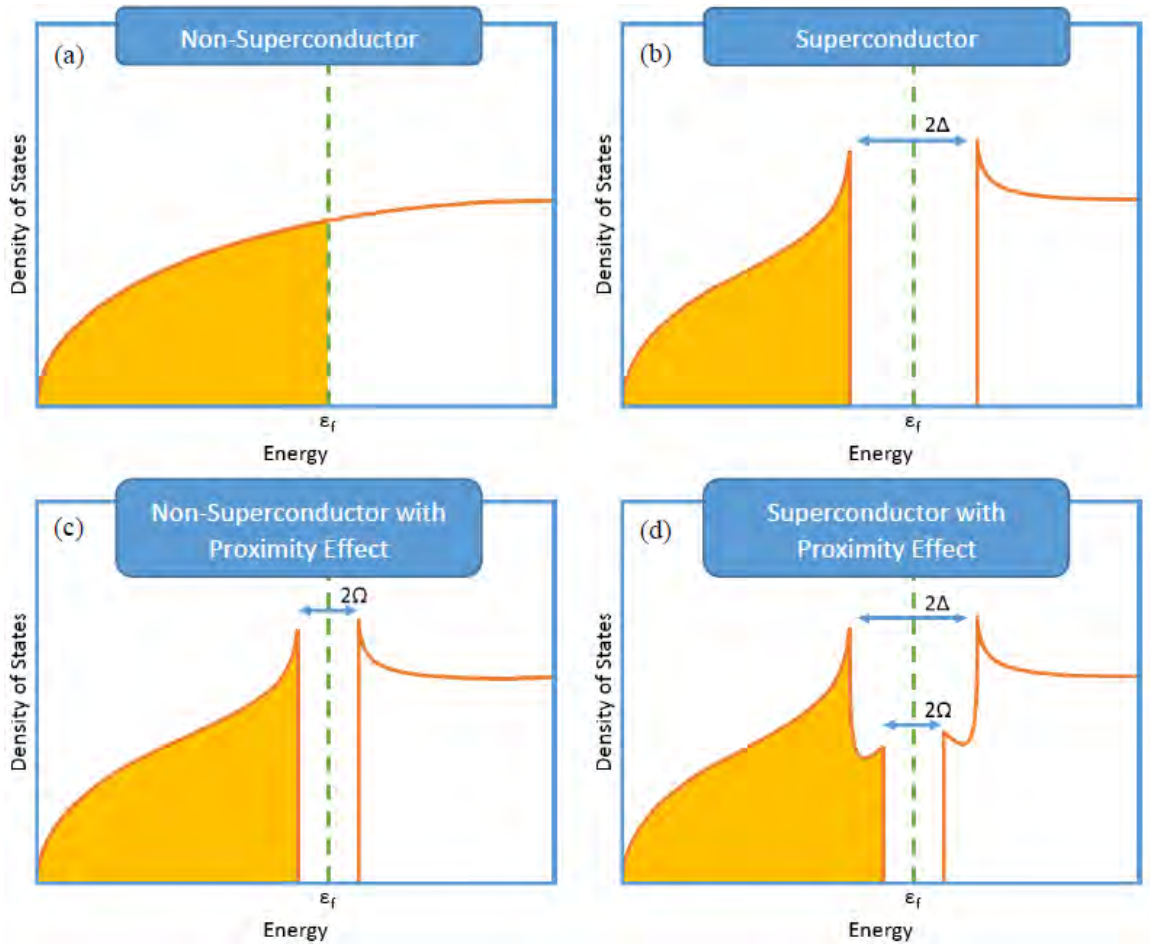

Figure 4.5: Illustration of density of states, in (a) a metal or doped-semiconductor, (b) a superconductor below the transition temperature, (c) the material of (a) with an induced energy gap, and (d) the superconductor of (b) with a weakened energy gap as a result of the proximity effect.

of semiconductor nano-wires which have formed a superconducting energy gap due to the proximity effect [72, 76].

Cooper Pair Recombination While the superconducting proximity effect leads to many unique electrical properties and new quasi-particles like the Majorana fermion, very few works have looked into the optical properties of semiconductors under the influence of the proximity effect [97–99]. Typically, superconductivity and optics are thought to be incompatible due to the large mismatch between the energy of the superconducting gap (a few meV) and the energy of optical photons (∼1 eV). In fact, this mismatch is the principle behind supercon-

ducting single photon detectors as it takes only a single photon to destroy a huge number of Cooper pairs, thereby destroying superconductivity over a relatively large region which can be measured electrically [100].

While this complicates things, it does not entirely rule out the integration of superconductivity and optics, and carefully designed experiments will allow the investigation of these systems. Several theoretical papers have attempted to describe the properties of radiative recombination of Cooper pair electrons with normal holes [101–103]. An important aspect of the recombination is that the two electrons of the Cooper pair are in a state lower than the Fermi energy, in a region where single electron states do not exist. Because of this it is not possible for a single electron from the Cooper pair to radiatively recombine as this would leave behind the other electron in a forbidden state. Therefore, both electrons must recombine with holes at the same time in a single second order process like that illustrated in fig. 4.6. In theory this process will emit two photons with opposite momentum and a total energy equal to twice the band-gap minus the superconducting energy gap. As it is a single second order photon emission event rather than two first order photon emission events there is no which-path information. This means the two photons should not only be correlated but should also be polarization-entangled [101]. Additionally, it is expected [102] and some preliminary results have shown [97], Cooper pair recombination leads to enhanced radiative recombination due to the macroscopic coherence of the many-body BCS ground state. It is important to note that only the sum of the energy of the two photons must be constant. While there will still be single-photon emission at the exciton energy (E_0), this can be spectrally removed and one can look for correlated/entangled photon pairs at $E_0 \pm \delta E$ [101].

Majorana Fermions While very few experimental results exist on the optical properties of hybrid semiconductor/superconductor structures, there have been exciting observations of the electrical properties which reveal the signs of Majorana fermions [72]. A Majorana fermion is a particle which is its own anti-particle and was first predicted as an alternative solution to the Dirac equation by Ettore Majorana in the 1930's. In the field of condensed matter physics it is expected to arise as a quasi-particle. A particle which is its own anti-

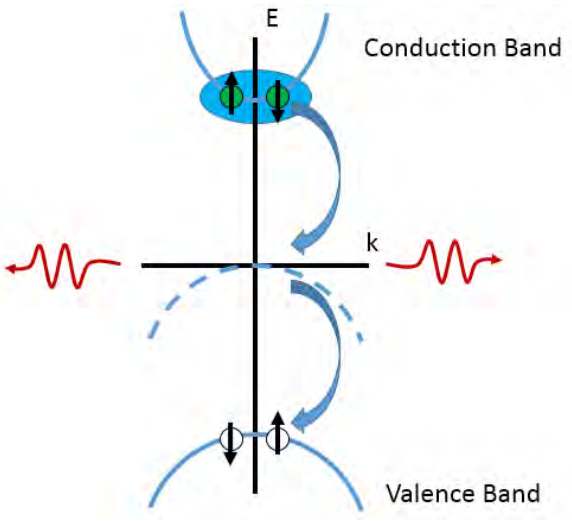

Figure 4.6: Schematic of the second-order process involving the recombination of a Cooper pair with two holes resulting in the emission of two polarization entangled photons.

particle will have a creation operator which is identical to it's annihilation operator. If we start with creation and annihilation operators for fermionic particles we can construct Majorana-like operators as follows.

$$\gamma_{2j-1} = c_j^\dagger + c_j \tag{4.1a}$$

$$\gamma_{2j} = \mathrm{i}\left(c_j^\dagger - c_j\right) \tag{4.1b}$$

We see then that $\gamma = \gamma^\dagger$ and that when we create a Majorana quasi-particle we end up with a superposition of an electron (c) and a hole ($c^\dagger$). The reason that Majorana fermions have gained such interest is that they fall into a class of quasi-particles known as anyons. When you exchange two fermions their wavefunction develops a phase factor of $e^{\mathrm{i}\pi} = -1$. On the other hand, when you exchange two bosons their wavefunction develops a phase factor of $e^{\mathrm{i}2\pi} = 1$. Anyons are a special class of particles in which the exchange of two particles results in an additional phase of $e^{\mathrm{i}\phi}$, where ϕ is can be an arbitrary number from 0 to 2π. Alexei Kitaev showed that fault tolerant quantum computing could be accomplished simply by multiple exchange operations on a set of non-Abelian anyons [104].

Kitaev Model In addition to showing that quantum computing could be accomplished using the exchange of anyons, Kitaev also provided a simple model for a one-dimensional system which exhibited Majorana quasi-particle edge states [105]. The Kitaev Hamiltonian is given in eq. 4.2

$$H = \sum_j \left[-w\left(c_j^\dagger c_{j+1} + c_{j+1}^\dagger c_j\right) - \mu\left(c_j^\dagger c_j - \frac{1}{2}\right) + \Delta c_j c_{j+1} + \Delta^* c_{j+1}^\dagger c_j^\dagger \right] \tag{4.2}$$

This model considers a one-dimensional chain of fermion (electron) sites labeled with the subscript j, as illustrated in fig. 4.7a. The first term of the Hamiltonian describes the energy (w) required for an electron to hop from one site to an adjacent site. The second term is the chemical potential (μ) which describes the energy required to add another electron to the system. The final two terms describe an induced superconducting energy gap (Δ). We see that it is associated with the occupation of two adjacent sites.

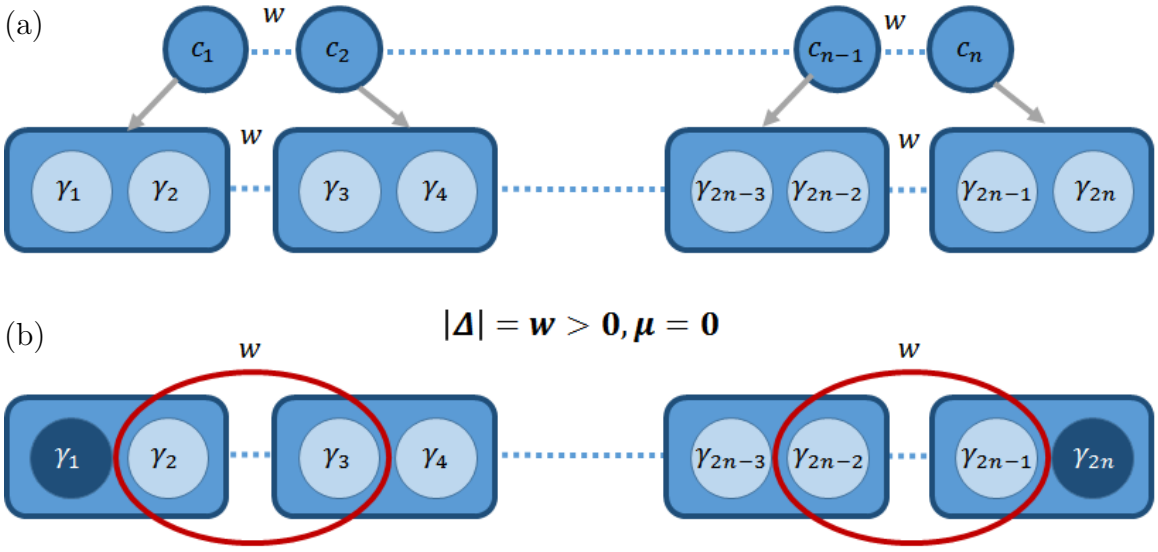

Figure 4.7: Illustration of the Kitaev model consisting of (a) a one-dimensional chain of fermion sites, which can be translated into pairs of Majorana quasi-particles. Under the right circumstances (b) the quasi-particles can be made to interact with neighboring sites in such a way that the first and last quasi-particle (γ_1, γ_{2n}) will be de-coupled, forming the basis of a topologically protected qubit.

In order to reduce this Hamiltonian to one in which we can easily see Majorana fermions we consider the special case where $\mu = 0$ and $|\Delta| = w > 0$, as illustrated in fig. 4.7b. In this case, eq. 4.2 reduces to eq. 4.3, where the Majorana fermion operators of eq. 4.1a and 4.1b

have been used to replace the fermion operators.

$$H = \mathrm{i}w \sum_{j=1}^{n-1} \gamma_{2j}\gamma_{2j+1} \tag{4.3}$$

In this Hamiltonian j ranges from 1 to $n-1$, where n is the number of original fermion sites. Each fermion site is essentially split into two Majorana quasi-particles ($c_1 \rightarrow \gamma_1, \gamma_2; c_2 \rightarrow \gamma_3, \gamma_4$; etc.). We see then that the interactions in eq. 4.3 are between Majorana fermions in different fermion sites. For example, the first term in the summation will be $\mathrm{i}w\gamma_2\gamma_3$, where $\gamma_2 = \mathrm{i}\left(c_1^\dagger - c_1\right)$ and $\gamma_3 = c_2^\dagger + c_2$. We also see that there are two Majorana operators which do not appear in this Hamiltonian, γ_1 and γ_{2n}. It is specifically these Majorana states that we're interested in. A quasi-particle created in either of these states will have zero energy, will not interact with particles in other states, and in theory would provide a qubit free from phase errors [105].

The Kitaev model has been realized in a system consisting of a InSb nano-wire (the 1D fermion chain), with a superconducting gap induced by a niobium titanium nitride (NbTiN) superconductor [72]. In a similar fashion, the QNOS group is positioned to investigate the existance of Majorana fermions in InAs based nano-structures with a superconducting gap induced by metallic indium islands. The ability to completely grow the structure in a single high-vacuum process will produce the cleanest interfaces between semiconductor and superconductor.

References

[1] J. C. Maxwell, "A dynamical theory of the electromagnetic field," *Philosophical Transactions of the Royal Society of London*, vol. 155, pp. 459–512, 1865.

[2] E. Yablonovitch, "Inhibited spontaneous emission in solid-state physics and electronics," *Physical review letters*, vol. 58, no. 20, p. 2059, 1987.

[3] V. G. Veselago, "The electrodynamics of substances with simultaneously negative values of ϵ and μ," *Physics-Uspekhi*, vol. 10, no. 4, pp. 509–514, 1968.

[4] U. C. Fischer and D. W. Pohl, "Observation of single-particle plasmons by near-field optical microscopy," *Physical review letters*, vol. 62, no. 4, p. 458, 1989.

[5] E. M. Purcell, "Spontaneous emission probabilities at radio frequencies," *Physical Review*, vol. 69, p. 681, 1946.

[6] E. T. Jaynes and F. W. Cummings, "Comparison of quantum and semiclassical radiation theories with application to the beam maser," *Proceedings of the IEEE*, vol. 51, no. 1, pp. 89–109, 1963.

[7] T. Yoshie, A. Scherer, J. Hendrickson, G. Khitrova, H. M. Gibbs, G. Rupper, C. Ell, O. B. Shchekin, and D. G. Deppe, "Vacuum Rabi splitting with a single quantum dot in a photonic crystal nanocavity," *Nature*, vol. 432, no. 7014, pp. 200–203, 2004.

[8] J. P. Reithmaier, G. Sek, A. Löffler, C. Hofmann, S. Kuhn, S. Reitzenstein, L. V. Keldysh, V. D. Kulakovskii, T. L. Reinecke, and A. Forchel, "Strong coupling in a single quantum dot–semiconductor microcavity system," *Nature*, vol. 432, no. 7014, pp. 197–200, 2004.

[9] J. B. Khurgin, "How to deal with the loss in plasmonics and metamaterials," *Nature nanotechnology*, vol. 10, no. 1, pp. 2–6, 2015.

[10] P. Biagioni, J.-S. Huang, and B. Hecht, "Nanoantennas for visible and infrared radiation," *Reports on Progress in Physics*, vol. 75, no. 2, p. 024402, 2012.

[11] J. N. Farahani, H.-J. Eisler, D. W. Pohl, M. Pavius, P. Flückiger, P. Gasser, and B. Hecht, "Bow-tie optical antenna probes for single-emitter scanning near-field optical microscopy," *Nanotechnology*, vol. 18, no. 12, p. 125506, 2007.

[12] A. V. Akimov, A. Mukherjee, C. L. Yu, D. E. Chang, A. S. Zibrov, P. R. Hemmer, H. Park, and M. D. Lukin, "Generation of single optical plasmons in metallic nanowires coupled to quantum dots," *Nature*, vol. 450, no. 7168, pp. 402–406, 2007.

[13] A. G. Curto, G. Volpe, T. H. Taminiau, M. P. Kreuzer, R. Quidant, and N. F. van Hulst, "Unidirectional emission of a quantum dot coupled to a nanoantenna," *Science*, vol. 329, no. 5994, pp. 930–933, 2010.

[14] L. Cao, P. Fan, A. P. Vasudev, J. S. White, Z. Yu, W. Cai, J. A. Schuller, S. Fan, and M. L. Brongersma, "Semiconductor nanowire optical antenna solar absorbers," *Nano letters*, vol. 10, no. 2, pp. 439–445, 2010.

[15] X. Fang, M. L. Tseng, J.-Y. Ou, K. F. MacDonald, D. P. Tsai, and N. I. Zheludev, "Ultrafast all-optical switching via coherent modulation of metamaterial absorption," *Applied Physics Letters*, vol. 104, no. 14, p. 141102, 2014.

[16] O. Hess, J. B. Pendry, S. A. Maier, R. F. Oulton, J. M. Hamm, and K. L. Tsakmakidis, "Active nanoplasmonic metamaterials," *Nature materials*, vol. 11, no. 7, pp. 573–584, 2012.

[17] N. Kumar, "Spontaneous emission rate enhancement using optical antennas," Ph.D. dissertation, University of California, Berkeley, 2013.

[18] J.-H. Song, J. Kim, H. Jang, I. Y. Kim, I. Karnadi, J. Shin, J. H. Shin, and Y.-H. Lee, "Fast and bright spontaneous emission of Er^{3+} ions in metallic nanocavity," *Nature communications*, vol. 6, 2015.

[19] T. M. Babinec, Y. A. Kelaita, K. A. Fischer, K. G. Lagoudakis, T. Sarmiento, A. Rundquist, A. Majumdar, and J. Vuckovic, "A light-matter interface based on a single InAs/GaAs quantum dot in a nanometallic cavity," *arXiv preprint arXiv:1406.7050*, 2014.

[20] A. F. Koenderink, "On the use of Purcell factors for plasmon antennas," *Optics letters*, vol. 35, no. 24, pp. 4208–4210, 2010.

[21] S. A. Maier, "Plasmonic field enhancement and SERS in the effective mode volume picture," *Optics Express*, vol. 14, no. 5, pp. 1957–1964, 2006.

[22] R. Ruppin, "Electromagnetic energy density in a dispersive and absorptive material," *Physics letters A*, vol. 299, no. 2, pp. 309–312, 2002.

[23] N. Meinzer, M. Ruther, S. Linden, C. M. Soukoulis, G. Khitrova, J. Hendrickson, J. D. Olitzky, H. M. Gibbs, and M. Wegener, "Arrays of Ag split-ring resonators coupled to InGaAs single-quantum-well gain," *Optics express*, vol. 18, no. 23, pp. 24 140–24 151, 2010.

[24] M. Husnik, M. W. Klein, N. Feth, M. König, J. Niegemann, K. Busch, S. Linden, and M. Wegener, "Absolute extinction cross-section of individual magnetic split-ring resonators," *Nature Photonics*, vol. 2, no. 10, pp. 614–617, 2008.

[25] M. Husnik, S. Linden, R. Diehl, J. Niegemann, K. Busch, and M. Wegener, "Quantitative experimental determination of scattering and absorption cross-section spectra of individual optical metallic nanoantennas," *Physical review letters*, vol. 109, no. 23, p. 233902, 2012.

[26] M. Husnik, J. Niegemann, K. Busch, and M. Wegener, "Quantitative spectroscopy on individual wire, slot, bow-tie, rectangular, and square-shaped optical antennas," *Optics letters*, vol. 38, no. 22, pp. 4597–4600, 2013.

[27] M. Helfrich, D. Hu, J. Hendrickson, M. Gehl, D. Rülke, R. Gröger, D. Litvinov, S. Linden, M. Wegener, D. Gerthsen, T. Schimmel, M. Hetterich, H. Kalt, G. Khitrova, H. M. Gibbs, and D. M. Schaadt, "Growth and annealing of InAs quantum dots on prestructured GaAs substrates," *Journal of Crystal Growth*, vol. 323, no. 1, pp. 187–190, 2011.

[28] J. Hendrickson, M. Helfrich, M. Gehl, D. Hu, D. Schaadt, S. Linden, M. Wegener, B. Richards, H. Gibbs, and G. Khitrova, "InAs quantum dot site-selective growth on GaAs substrates," *physica status solidi (c)*, vol. 8, no. 4, pp. 1242–1245, 2011.

[29] B. C. Richards, J. Hendrickson, J. D. Olitzky, R. Gibson, M. Gehl, K. Kieu, U. K. Khankhoje, A. Homyk, A. Scherer, J.-Y. Kim, Y.-H. Lee, G. Khitrova, and H. M. Gibbs, "Characterization of 1D photonic crystal nanobeam cavities using curved microfiber," *Optics express*, vol. 18, no. 20, pp. 20 558–20 564, 2010.

[30] B. C. Richards, J. Hendrickson, J. D. Olitzky, R. Gibson, M. Gehl, K. Kieu, P. Polynkin, G. Khitrova, H. M. Gibbs, U. K. Khankhoje, A. Homyk, A. Scherer, J.-Y. Kim, and Y.-H. Lee, "Progress in growth, fabrication, and characterization of semiconductor photonic crystal nanocavities," *physica status solidi (b)*, vol. 248, no. 4, pp. 892–896, 2011.

[31] M. Gehl, R. Gibson, J. Hendrickson, A. Homyk, A. Säynätjoki, T. Alasaarela, L. Karvonen, A. Tervonen, S. Honkanen, S. Zandbergen, B. C. Richards, J. D. Olitzky, A. Scherer, G. Khitrova, H. M. Gibbs, J.-Y. Kim, and Y.-H. Lee, "Effect of atomic layer deposition on the quality factor of silicon nanobeam cavities," *JOSA B*, vol. 29, no. 2, pp. A55–A59, 2012.

[32] M. Gehl, S. Zandbergen, R. Gibson, M. Béchu, N. Nader, J. Hendrickson, J. Sears, P. Keiffer, M. Wegener, and G. Khitrova, "Spectroscopic studies of resonant coupling of silver optical antenna arrays to a near-surface quantum well," *Journal of Optics*, vol. 16, no. 11, p. 114016, 2014.

[33] R. Gibson, M. Gehl, J. Sears, S. Zandbergen, N. Nader, P. Keiffer, J. Hendrickson, A. Arnoult, and G. Khitrova, "Molecular beam epitaxy grown indium self-assembled plasmonic nanostructures," *Journal of Crystal Growth*, vol. 425, pp. 307–311, 2015.

[34] D. Leonard, M. Krishnamurthy, C. M. Reaves, S. P. Denbaars, and P. M. Petroff, "Direct formation of quantum-sized dots from uniform coherent islands of InGaAs on GaAs surfaces," *Applied Physics Letters*, vol. 63, no. 23, pp. 3203–3205, 1993.

[35] J. I. Cirac, P. Zoller, H. J. Kimble, and H. Mabuchi, "Quantum state transfer and entanglement distribution among distant nodes in a quantum network," *Physical Review Letters*, vol. 78, no. 16, p. 3221, 1997.

[36] G. Khitrova, H. M. Gibbs, F. Jahnke, M. Kira, and S. W. Koch, "Nonlinear optics of normal-mode-coupling semiconductor microcavities," *Reviews of Modern Physics*, vol. 71, no. 5, p. 1591, 1999.

[37] P. Michler, A. Kiraz, C. Becher, W. Schoenfeld, P. Petroff, L. Zhang, E. Hu, and A. Imamoglu, "A quantum dot single-photon turnstile device," *Science*, vol. 290, no. 5500, pp. 2282–2285, 2000.

[38] M. Pelton, C. Santori, J. Vucković, B. Zhang, G. S. Solomon, J. Plant, and Y. Yamamoto, "Efficient source of single photons: a single quantum dot in a micropost microcavity," *Physical review letters*, vol. 89, no. 23, p. 233602, 2002.

[39] P. Atkinson, S. Kiravittaya, M. Benyoucef, A. Rastelli, and O. G. Schmidt, "Site-controlled growth and luminescence of InAs quantum dots using *in situ* Ga-assisted deoxidation of patterned substrates," *Applied Physics Letters*, vol. 93, no. 10, p. 101908, 2008.

[40] M. Soljačić, M. Ibanescu, S. G. Johnson, Y. Fink, and J. D. Joannopoulos, "Optimal bistable switching in nonlinear photonic crystals," *Physical Review E*, vol. 66, no. 5, p. 055601, 2002.

[41] J. Chan, T. M. Alegre, A. H. Safavi-Naeini, J. T. Hill, A. Krause, S. Gröblacher, M. Aspelmeyer, and O. Painter, "Laser cooling of a nanomechanical oscillator into its quantum ground state," *Nature*, vol. 478, no. 7367, pp. 89–92, 2011.

[42] H. Z. Chen, A. Ghaffari, H. Wang, H. Morkoc, and A. Yariv, "Continuous-wave operation of extremely low-threshold GaAs/AlGaAs broad-area injection lasers on (100) Si substrates at room temperature," *Optics letters*, vol. 12, no. 10, pp. 812–813, 1987.

[43] A. W. Fang, H. Park, O. Cohen, R. Jones, M. J. Paniccia, and J. E. Bowers, "Electrically pumped hybrid AlGaInAs-silicon evanescent laser," *Optics express*, vol. 14, no. 20, pp. 9203–9210, 2006.

[44] X. Sun, A. Zadok, M. J. Shearn, K. A. Diest, A. Ghaffari, H. A. Atwater, A. Scherer, and A. Yariv, "Electrically pumped hybrid evanescent Si/InGaAsP lasers," *Optics letters*, vol. 34, no. 9, pp. 1345–1347, 2009.

[45] T. Birks and Y. W. Li, "The shape of fiber tapers," *Journal of Lightwave Technology*, vol. 10, no. 4, pp. 432–438, 1992.

[46] A. Säynätjoki, "Atomic-layer-deposited thin films for silicon nanophotonics," *SPIE Newsroom*, 2012.

[47] T. Alasaarela, D. Korn, L. Alloatti, A. Säynätjoki, A. Tervonen, R. Palmer, J. Leuthold, W. Freude, and S. Honkanen, "Reduced propagation loss in silicon strip and slot waveguides coated by atomic layer deposition," *Optics express*, vol. 19, no. 12, pp. 11 529–11 538, 2011.

[48] A. F. Oskooi, D. Roundy, M. Ibanescu, P. Bermel, J. D. Joannopoulos, and S. G. Johnson, "MEEP: A flexible free-software package for electromagnetic simulations by the FDTD method," *Computer Physics Communications*, vol. 181, pp. 687–702, January 2010.

[49] A. D. Rakić, A. B. Djurišić, J. M. Elazar, and M. L. Majewski, "Optical properties of metallic films for vertical-cavity optoelectronic devices," *Applied optics*, vol. 37, no. 22, pp. 5271–5283, 1998.

[50] E. D. Palik, *Handbook of optical constants of solids*. Academic press, 1998, vol. 3.

[51] P. B. Johnson and R.-W. Christy, "Optical constants of the noble metals," *Physical Review B*, vol. 6, no. 12, p. 4370, 1972.

[52] M. Wegener, J. L. García-Pomar, C. M. Soukoulis, N. Meinzer, M. Ruther, and S. Linden, "Toy model for plasmonic metamaterial resonances coupled to two-level system gain," *Optics express*, vol. 16, no. 24, pp. 19 785–19 798, 2008.

[53] H. J. Metcalf and P. van der Straten, *Laser Cooling and Trapping*, 1st ed. Springer New York, 1999.

[54] K. Busch, G. Von Freymann, S. Linden, S. F. Mingaleev, L. Tkeshelashvili, and M. Wegener, "Periodic nanostructures for photonics," *Physics reports*, vol. 444, no. 3, pp. 101–202, 2007.

[55] B. R. Bennett, R. A. Soref, and J. del Alamo, "Carrier-induced change in refractive index of InP, GaAs and InGaAsP," *Quantum Electronics, IEEE Journal of*, vol. 26, no. 1, pp. 113–122, 1990.

[56] N. Meinzer, M. König, M. Ruther, S. Linden, G. Khitrova, H. M. Gibbs, K. Busch, and M. Wegener, "Distance-dependence of the coupling between split-ring resonators and single-quantum-well gain," *Applied Physics Letters*, vol. 99, no. 11, p. 111104, 2011.

[57] A. Boltasseva and H. A. Atwater, "Low-loss plasmonic metamaterials," *Science*, 2011.

[58] P. R. West, S. Ishii, G. V. Naik, N. K. Emani, V. M. Shalaev, and A. Boltasseva, "Searching for better plasmonic materials," *Laser & Photonics Reviews*, vol. 4, no. 6, pp. 795–808, 2010.

[59] G. V. Naik, V. M. Shalaev, and A. Boltasseva, "Alternative plasmonic materials: beyond gold and silver," *Advanced Materials*, vol. 25, no. 24, pp. 3264–3294, 2013.

[60] Y. Wu, C. Zhang, N. M. Estakhri, Y. Zhao, J. Kim, M. Zhang, X.-X. Liu, G. K. Pribil, A. Alù, C.-K. Shih, and X. Li, "Intrinsic optical properties and enhanced plasmonic response of epitaxial silver," *Advanced Materials*, vol. 26, no. 35, pp. 6106–6110, 2014.

[61] A. Urbańczyk, F. W. M. van Otten, and R. Nötzel, "Self-aligned epitaxial metal-semiconductor hybrid nanostructures for plasmonics," *Applied Physics Letters*, vol. 98, no. 24, p. 243110, 2011.

[62] A. Urbańczyk and R. Nötzel, "Site-controlled Ag nanocrystals grown by molecular beam epitaxy–Towards plasmonic integration technology," *Journal of Applied Physics*, vol. 112, no. 12, p. 124302, 2012.

[63] M. H. Devoret and R. J. Schoelkopf, "Superconducting circuits for quantum information: an outlook," *Science*, vol. 339, no. 6124, pp. 1169–1174, 2013.

[64] C. Rigetti, J. M. Gambetta, S. Poletto, B. L. T. Plourde, J. M. Chow, A. D. Córcoles, J. A. Smolin, S. T. Merkel, J. R. Rozen, G. A. Keefe, M. B. Rothwell, M. B. Ketchen, and M. Steffen, "Superconducting qubit in a waveguide cavity with a coherence time approaching 0.1 ms," *Physical Review B*, vol. 86, no. 10, p. 100506, 2012.

[65] N. Gisin, G. Ribordy, W. Tittel, and H. Zbinden, "Quantum cryptography," *Reviews of modern physics*, vol. 74, no. 1, p. 145, 2002.

[66] S. S. Mou, H. Irie, Y. Asano, K. Akahane, H. Kurosawa, H. Nakajima, H. Kumano, M. Sasaki, and I. Suemune, "Superconducting light-emitting diodes," *Selected Topics in Quantum Electronics, IEEE Journal of*, vol. 21, no. 2, pp. 1–11, 2015.

[67] I. Suemune, H. Sasakura, Y. Asano, H. Kumano, R. Inoue, K. Tanaka, T. Akazaki, and H. Takayanagi, "Photon-pair generation based on superconductivity," *IEICE Electronics Express*, vol. 9, no. 14, pp. 1184–1200, 2012.

[68] W.-H. Li, C. C. Yang, F. C. Tsao, S. Y. Wu, P. J. Huang, M. K. Chung, and Y. D. Yao, "Enhancement of superconductivity by the small size effect in In nanoparticles," *Physical Review B*, vol. 72, no. 21, p. 214516, 2005.

[69] A. M. Toxen, "Size effects in thin superconducting indium films," *Physical Review*, vol. 123, no. 2, p. 442, 1961.

[70] F.-Y. Wu, C. C. Yang, C.-M. Wu, C.-W. Wang, and W.-H. Li, "Superconductivity in zero-dimensional indium nanoparticles," *Journal of applied physics*, vol. 101, no. 9, p. 09G111, 2007.

[71] M. Tinkham, *Introduction to Superconductivity*, 2nd ed. Dover Publications, Inc., 1996.

[72] V. Mourik, K. Zuo, S. M. Frolov, S. R. Plissard, E. P. A. M. Bakkers, and L. P. Kouwenhoven, "Signatures of Majorana fermions in hybrid superconductor-semiconductor nanowire devices," *Science*, vol. 336, no. 6084, pp. 1003–1007, 2012.

[73] Y. Makhlin, G. Schön, and A. Shnirman, "Quantum-state engineering with Josephson-junction devices," *Reviews of modern physics*, vol. 73, no. 2, p. 357, 2001.

[74] W. Chang, V. E. Manucharyan, T. S. Jespersen, J. Nygård, and C. M. Marcus, "Tunneling spectroscopy of quasiparticle bound states in a spinful Josephson junction," *Physical review letters*, vol. 110, no. 21, p. 217005, 2013.

[75] M. Cheng, R. M. Lutchyn, and S. D. Sarma, "Topological protection of Majorana qubits," *Physical Review B*, vol. 85, no. 16, p. 165124, 2012.

[76] P. W. Brouwer, "Enter the Majorana fermion," *Science*, vol. 336, no. 6084, pp. 989–990, 2012.

[77] P. Macha, G. Oelsner, J.-M. Reiner, M. Marthaler, S. André, G. Schön, U. Hübner, H.-G. Meyer, E. Ilichev, and A. V. Ustinov, "Implementation of a quantum metamaterial using superconducting qubits," *Nature communications*, vol. 5, 2014.

[78] J. Q. You and F. Nori, "Atomic physics and quantum optics using superconducting circuits," *Nature*, vol. 474, no. 7353, pp. 589–597, 2011.

[79] T. M. Klapwijk, "Proximity effect from an Andreev perspective," *Journal of superconductivity*, vol. 17, no. 5, pp. 593–611, 2004.

[80] I. E. Batov, T. Schäpers, N. M. Chtchelkatchev, H. Hardtdegen, and A. V. Ustinov, "Andreev reflection and strongly enhanced magnetoresistance oscillations in $Ga_xIn_{1-x}As$/InP heterostructures with superconducting contacts," *Physical Review B*, vol. 76, no. 11, p. 115313, 2007.

[81] W. Chang, "Superconducting proximity effect in InAs nanowires," Ph.D. dissertation, Harvard University, 2014.

[82] B. Pannetier and H. Courtois, "Andreev reflection and proximity effect," *Journal of low temperature physics*, vol. 118, no. 5-6, pp. 599–615, 2000.

[83] C. Beenakker, "Three universal mesoscopic Josephson effects," in *Transport Phenomena in Mesoscopic Systems*. Springer, 1992, pp. 235–253.

[84] H. B. Heersche, P. Jarillo-Herrero, J. B. Oostinga, L. M. K. Vandersypen, and A. F. Morpurgo, "Bipolar supercurrent in graphene," *Nature*, vol. 446, no. 7131, pp. 56–59, 2007.

[85] Z. Han, A. Allain, H. Arjmandi-Tash, K. Tikhonov, M. FeigelMan, B. Sacépé, and V. Bouchiat, "Collapse of superconductivity in a hybrid tin-graphene Josephson junction array," *Nature Physics*, vol. 10, no. 5, pp. 380–386, 2014.

[86] C. W. J. Beenakker, "Quantum transport in semiconductor-superconductor microjunctions," *Physical Review B*, vol. 46, no. 19, p. 12841, 1992.

[87] R. Inoue, H. Takayanagi, T. Akazaki, K. Tanaka, and I. Suemune, "Transport characteristics of a superconductor-based LED," *Superconductor Science and Technology*, vol. 23, no. 3, p. 034025, 2010.

[88] S. Takei, B. M. Fregoso, H.-Y. Hui, A. M. Lobos, and S. D. Sarma, "Soft superconducting gap in semiconductor Majorana nanowires," *Physical review letters*, vol. 110, no. 18, p. 186803, 2013.

[89] W. L. McMillan, "Tunneling model of the superconducting proximity effect," *Physical Review*, vol. 175, no. 2, p. 537, 1968.

[90] B. Van Wees, "Superconducting semiconductors," *Phys. World*, vol. 41, pp. 41–46, 1996.

[91] H. Le Sueur, P. Joyez, H. Pothier, C. Urbina, and D. Esteve, "Phase controlled superconducting proximity effect probed by tunneling spectroscopy," *Physical review letters*, vol. 100, no. 19, p. 197002, 2008.

[92] Y.-J. Doh, J. A. van Dam, A. L. Roest, E. P. A. M. Bakkers, L. P. Kouwenhoven, and S. De Franceschi, "Tunable supercurrent through semiconductor nanowires," *science*, vol. 309, no. 5732, pp. 272–275, 2005.

[93] A. Kastalsky, A. W. Kleinsasser, L. H. Greene, R. Bhat, F. P. Milliken, and J. P. Harbison, "Observation of pair currents in superconductor-semiconductor contacts," *Physical review letters*, vol. 67, no. 21, p. 3026, 1991.

[94] A. Chrestin, T. Matsuyama, and U. Merkt, "Evidence for a proximity-induced energy gap in Nb/InAs/Nb junctions," *Physical Review B*, vol. 55, no. 13, p. 8457, 1997.

[95] U. Schüssler and R. Kümmel, "Andreev scattering, Josephson currents, and coupling energy in clean superconductor-semiconductor-superconductor junctions," *Physical Review B*, vol. 47, no. 5, p. 2754, 1993.

[96] B. J. Van Wees, P. de Vries, P. Magnée, and T. M. Klapwijk, "Excess conductance of superconductor-semiconductor interfaces due to phase conjugation between electrons and holes," *Physical review letters*, vol. 69, no. 3, p. 510, 1992.

[97] H. Sasakura, S. Kuramitsu, Y. Hayashi, K. Tanaka, T. Akazaki, E. Hanamura, R. Inoue, H. Takayanagi, Y. Asano, C. Hermannstädter, H. Kumano, and I. Suemune, "Enhanced photon generation in a Nb/n–InGaAs/p–InP superconductor/semiconductor-diode light emitting device," *Physical review letters*, vol. 107, no. 15, p. 157403, 2011.

[98] A. Ignatov, R. H. Yuan, and N. L. Wang, "Photo luminescence of Cooper pairs in a naturally occurring heretostructure $K_{0.75}Fe_{1.75}Se_2$," *arXiv preprint arXiv:1307.3471*, 2013.

[99] I. Suemune, Y. Hayashi, S. Kuramitsu, K. Tanaka, T. Akazaki, H. Sasakura, R. Inoue, H. Takayanagi, Y. Asano, E. Hanamura, S. Odashima, and H. Kumano, "A Cooper-pair light-emitting diode: Temperature dependence of both quantum efficiency and radiative recombination lifetime," *Applied physics express*, vol. 3, no. 5, p. 054001, 2010.

[100] W. H. P. Pernice, C. Schuck, O. Minaeva, M. Li, G. N. Goltsman, A. V. Sergienko, and H. X. Tang, "High-speed and high-efficiency travelling wave single-photon detectors embedded in nanophotonic circuits," *Nature communications*, vol. 3, p. 1325, 2012.

[101] A. Hayat, H.-Y. Kee, K. S. Burch, and A. M. Steinberg, "Cooper-pair-based photon entanglement without isolated emitters," *Physical Review B*, vol. 89, no. 9, p. 094508, 2014.

[102] Y. Asano, I. Suemune, H. Takayanagi, and E. Hanamura, "Luminescence of a Cooper pair," *Physical review letters*, vol. 103, no. 18, p. 187001, 2009.

[103] P. Baireuther, P. P. Orth, I. Vekhter, and J. Schmalian, "Manipulation of a two-photon pump in superconductor-semiconductor heterostructures," *Physical review letters*, vol. 112, no. 7, p. 077003, 2014.

[104] A. Y. Kitaev, "Fault-tolerant quantum computation by anyons," *Annals of Physics*, vol. 303, no. 1, pp. 2–30, 2003.

[105] A. Y. Kitaev, "Unpaired Majorana fermions in quantum wires," *Physics-Uspekhi*, vol. 44, no. 10S, p. 131, 2001.

Appendix A

Characterization of 1D photonic crystal nanobeam cavities using curved microfiber

B. C. Richards, J. Hendrickson, J. D. Olitzky, R. Gibson, M. Gehl, K. Kieu, U. K. Khankhoje, A. Homyk, A. Scherer, J.-Y. Kim, Y.-H. Lee, G. Khitrova, H. M. Gibbs

Optics Express, Vol. 18, No. 20, pp. 20558-20564 (September, 2010)

Characterization of 1D photonic crystal nanobeam cavities using curved microfiber

B. C. Richards,[1,*] J. Hendrickson,[1] J. D. Olitzky,[1] R. Gibson,[1] M. Gehl,[1] K. Kieu,[1] U. K. Khankhoje,[2] A. Homyk,[2] A. Scherer,[2] J.-Y. Kim,[3] Y.-H. Lee,[3] G. Khitrova,[1] H. M. Gibbs,[1]

[1]*College of Optical Sciences, The University of Arizona, Tucson, AZ 85721, USA*
[2]*Electrical Engineering, California Institute of Technology, Pasadena, CA 91125, USA*
[3]*Department of Physics, Korea Advanced Institute of Science and Technology, Daejeon 305-701, Korea*
[*]*brichards@optics.arizona.edu*

Abstract: We investigate high-*Q*, small mode volume photonic crystal nanobeam cavities using a curved, tapered optical microfiber loop. The strength of the coupling between the cavity and the microfiber loop is shown to depend on the contact position on the nanobeam, angle between the nanobeam and the microfiber, and polarization of the light in the fiber. The results are compared to a resonant scattering measurement.

OCIS codes: (350.4238) Nanophotonics and photonic crystals; (140.3948) Microcavity devices

References and links

1. T. Yoshie, A. Scherer, J. Hendrickson, G. Khitrova, H. M. Gibbs, G. Rupper, C. Ell, O. B. Shchekin, and D. G. Deppe, "Vacuum Rabi splitting with a single quantum dot in a photonic crystal nanocavity," Nature **432,** 200-203 (2004).
2. D. Englund, D. Fattal, E. Waks, G. Solomon, B. Zhang, T. Nakaoka, Y. Arakawa, Y. Yamamoto, and J. Vuckovic, "Controlling the spontaneous emission rate of a single quantum dot in a two dimensional photonic crystal," Phys. Rev. Lett. **95,** 013904 (2005).
3. D. Press, S. Gotzinger, S. Reitzenstein, C. Hofman, A. Loffler, M. Kamp, A. Forchel, and Y. Yamamoto, "Photon antibunching from a single quantum-dot-microcavity system in the strong coupling regime," Phys. Rev. Lett. **98,** 117402 (2007).
4. G. Khitrova, H. M. Gibbs, M. Kira, S. W. Koch, and A. Scherer, "Vacuum Rabi splitting in semiconductors," Nat. Phys. **2,** 81-90 (2006).
5. U. K. Khankhoje, S.-H. Kim, B. C. Richards, J. Hendrickson, J. Sweet, J. D. Olitzky, G. Khitrova, H. M. Gibbs, and A. Scherer, "Modelling and fabrication of GaAs photonic-crystal cavities for cavity quantum electrodynamics", Nanotechnology **21,** 065202 (2010).
6. J. Sweet, B. C. Richards, J. D. Olitzky, J. Hendrickson, G. Khitrova, H. M. Gibbs, D. Litvinov, D. Gerthsen, D. Z. Hu, D. M. Schaadt, M. Wegener, U. Khankhoje, and A. Scherer, "GaAs photonic crystal slab nanocavities: Growth, fabrication, and quality factor," Photonics and Nanostructures – Fundamentals and Applications **8,** 1-6 (2010).
7. M. W. McCutcheon, G. W. Rieger, I. W. Cheung, J. F. Young, D. Dalacu, S. Frédérick, P. J. Poole, G. C. Aers, and R. L. Williams, "Resonant scattering and second-harmonic spectroscopy of planar photonic crystal microcavities," Appl. Phys. Lett. **87,** 221110 (2005).
8. D. Englund, A. Faraon, I. Fushman, N. Stoltz, P. Petroff, and J. Vučković, "Controlling cavity reflectivity with a single quantum dot," Nature **450,** 857-861 (2007).
9. K. Srinivasan, P. E. Barclay, M. Borselli, and O. Painter, "Optical-fiber-based measurement of an ultrasmall volume high-Q photonic crystal microcavity," Phys. Rev. B **70,** 081306(R) (2004).
10. I.-K. Hwang, G.-H. Kim, and Y.-H. Lee, "Optimization of coupling between photonic crystal resonator and curved microfiber," IEEE J. of Quantum Electron., **42,** 131—6 (2006).
11. P. Deotare, M. McCutcheon, I. Frank, M. Khan, and M. Loncăr, "High quality factor photonic crystal nanobeam cavities," Appl. Phys. Lett. **94,** 121106 (2009).
12. C. Sauvan, P. Lalanne, and J. Hugonin, "Slow-wave effect and mode-profile matching in photonic crystal microcavities," Phys. Rev. B **71,** 1-4 (2005).
13. A. Oskooi, D. Roundy, M. Ibanescu, P. Bermel, J. Joannopoulos, and S. Johnson, "Meep: A flexible free-software package for electromagnetic simulations by the FDTD method," Comput. Phys. Commun. **181,** 687702 (2010).

#131274 - $15.00 USD Received 7 Jul 2010; revised 3 Sep 2010; accepted 4 Sep 2010; published 13 Sep 2010

14. A. R. M. Zain, N. P. Johnson, M. Sorel, and R. M. De La Rue, "Ultra high quality factor one dimensional photonic crystal/photonic wire micro-cavities in silicon-on-insulator (SOI)," Opt. Express **16,** 12084-12089 (2008).
15. M. Galli, S. L. Portalupi, M. Belotti, L. C. Andreani, L. O'Faolain, and T. F. Krauss, "Light scattering and Fano resonances in high-Q photonic crystal nanocavities," Appl. Phys. Lett. **94,** 071101 (2009).
16. S. Mosor, J. Hendrickson, B. C. Richards, J. Sweet, G. Khitrova, H. M. Gibbs, T. Yoshie, A. Scherer, O. B. Shchekin, and D. G. Deppe, "Scanning a photonic crystal slab nanocavity by condensation of xenon," Appl. Phys. Lett. **87**, 141105 (2005).

1. Introduction

The use of photonic crystal nanocavities as a means of confining light has led to an active field of cavity quantum electrodynamics research in the solid state. Specifically, the interaction between such confined fields and matter has led to the observation of a number of fundamental quantum optics results in semiconductors [1-3]. The primary way of enhancing such interactions between light and matter is to increase the ratio of quality factor Q to effective mode volume V. Increasing Q provides longer photon storage times, which leads to a greater chance of interaction between the light and the matter. Decreasing V leads to higher field intensities in the cavity, and hence stronger interactions between the light and the matter. High Q and small V are pursued by the semiconductor cavity QED community because they are essential for large Purcell enhancement ($F_p \propto Q/V$) of spontaneous emission and for a large vacuum Rabi splitting (VRS $\propto Q/\sqrt{V}$) [1, 2, 4-6].

Cavity QED experiments with quantum dots (QDs) as the active emitters are usually performed at cryogenic temperatures. In this temperature regime, radiative recombination of excited carriers is the dominant decay mechanism, and hence the dots are easily studied by optical spectroscopic techniques. As a result, the standard technique of measuring cavity Qs using QD photoluminescence usually requires expensive helium cryostats. Since characterizing cavity Qs is a time consuming task for researchers in this field, techniques have been developed to enable measuring Qs independently of the active emitters, and hence at room temperatures. Measuring a probe signal in a cross-polarized resonant scattering configuration [7-8] and using a tapered microfiber probe [9-10] are two such techniques that have been developed and employed specifically for semiconductor cavity QED.

We report the results of our investigations of 1D photonic crystal nanobeam cavities by means of a microfiber tapered loop. Using this method to investigate silicon nanobeams on a silica substrate, we have measured the highest Q/V ratio reported for such devices. We present the results of these experiments, as well as a comparison between the two methods of cross-polarized resonant scattering and tapered fiber transmission. We observe an asymmetric lineshape of the cavity modes using both approaches, and show that the asymmetry can be varied in the case of the tapered fiber by varying the input polarization of the probe field.

2. Photonic crystal design and fabrication

The cavity considered here is a nanobeam cavity, which is essentially a wavelength-scale Fabry-Perot etalon formed by sandwiching a 1D photonic crystal waveguide between 1D photonic crystal Bloch mirrors, as shown in Figure 1. In the transverse directions, the light is confined in the nanobeam by total internal reflection. By smoothly tapering the air hole radius and the corresponding lattice constants in the mirror sections, the scattering loss is minimized and a high Q is achieved [11-12]. 3D finite-difference time-domain (FDTD) simulations [13] reveal that the cavity exhibits a reasonably high Q in excess of 500,000 with very low mode volumes, even though it is placed on a low index substrate. The region of tapered holes in the center of the nanobeam effectively confines the light, analogous to a Fabry-Perot spacer.

#131274 - $15.00 USD Received 7 Jul 2010; revised 3 Sep 2010; accepted 4 Sep 2010; published 13 Sep 2010

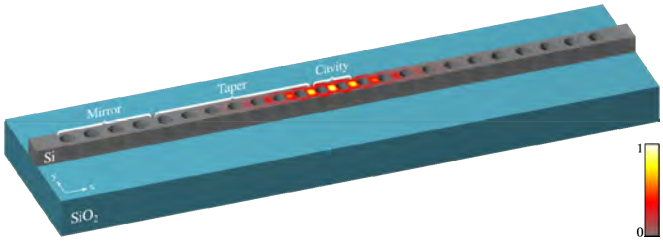

Figure 1. Schematic of cavity geometry with normalized electric field energy density $\varepsilon|E|^2$ through mid-plane of Si slab showing maximum concentration in cavity region. With the lattice constant in the mirror section as "a", the tapered section lattice constant ranges from 0.98a to 0.86a in 0.02a decrements, ending in the cavity section with 0.84a. Hole radius is 0.3 times the local lattice constant. For a 220 nm Si slab on bulk SiO_2 with a = 410 nm, the computed Q is 519,083 at λ = 1490 nm and mode volume $V = 0.27(\lambda/n)^3$ with $n = 3.53$.

The nanobeams are fabricated using electronics grade silicon-on-insulator with a 220 nm silicon device layer and 2 μm buried oxide. To prepare the samples for electron-beam lithography, the wafers are manually cleaved, cleaned with acetone and isopropanol, and the native oxide is removed by a short dip in 10:1 buffered hydrofluoric acid. The samples are then baked at 180 ºC, spin-coated with 2 percent PMMA 950K in chlorobenzene, and baked again at 180 ºC for 5 minutes. Electron-beam lithography is performed in a Leica EBPG 5000+ at 100kV. Following electron-beam exposure, the samples are developed in 1:3 MIBK:IPA for 60 seconds, rinsed in IPA, and dried with nitrogen. After development, the wafers are etched using an Oxford Instruments Plasmalab System100 ICP380 with a mixed-mode gas chemistry consisting of SF_6 and C_4F_8. Figure 2 shows SEM images of one of our nanobeam cavities.

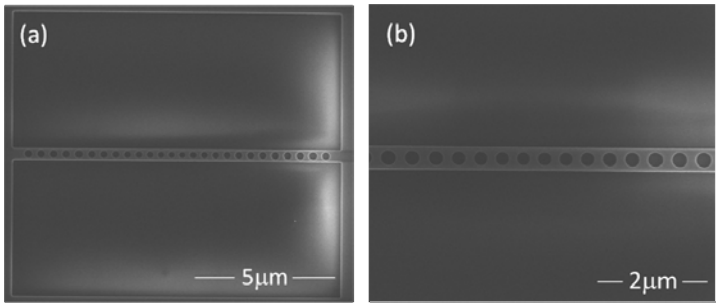

Figure 2. (a) SEM image of a nanobeam cavity. (b) SEM image of the center of a nanobeam, showing region of tapered holes.

3. Fiber transmission measurement

We investigate the spectral response of our nanobeam cavities by means of a curved, tapered optical fiber. The taper is fabricated in two stages. In the first stage, a Corning SMF-28 optical fiber is heated and stretched to a diameter of 1 μm, in which the tapered region operates in a single mode at 1.55 μm. In the second stage, mechanical translation stages are used to form the taper into a highly curved loop with typically 90 μm radius of curvature. The fiber taper loop is mounted onto a motorized xyz stage and brought into contact with the nanobeam cavity. The loop has proven very robust, as we have used the same loop for ten months so far

#131274 - $15.00 USD Received 7 Jul 2010; revised 3 Sep 2010; accepted 4 Sep 2010; published 13 Sep 2010

without any problems. An Agilent 8164A mainframe with an Agilent 81682A tunable laser with 0.2 pm wavelength resolution is input into the fiber equipped with an inline polarization compensator before propagating through the tapered region. The transmitted light is detected at the output end of the fiber by an InGaAs photodiode. The laser is tuned across the cavity resonance, and the interaction of the light with the cavity mode can be observed as a change in the transmitted intensity of the propagating field. The laser needs to have resolution better than the FWHM of the cavity mode and amplitude fluctuations must be slower than the time to scan across a mode. The *Q* is the transition energy of the mode divided by the FWHM energy width of the cavity mode. The nanobeam sample is mounted on a stage rotating about an axis normal to the sample, so that the angle between the tapered fiber and the axis of the nanobeam cavity can be varied. Figure 3 (a) shows a typical fiber loop transmission spectrum of a nanobeam cavity, with two cavity modes visible.

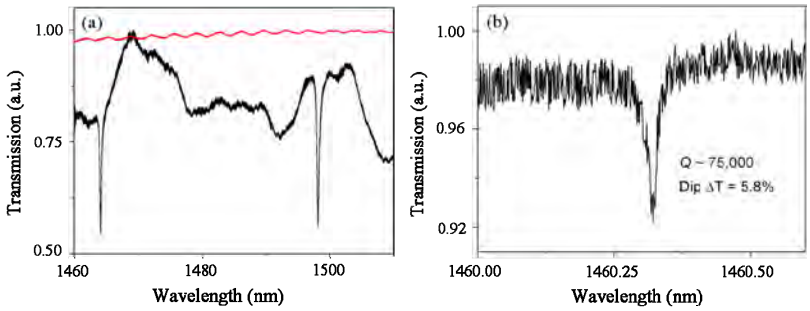

Figure 3. (a) Fiber loop transmission spectrum of a typical nanobeam cavity at 45º, center contact (black) and spectrum directly from laser (red). (b) Fiber loop transmission spectrum of a high-*Q* nanobeam cavity mode, at 45º, edge contact, with *Q* = 75,000.

4. Fiber coupling to a nanobeam

By nature of the physical interaction between the field in the fiber taper and the nanobeam, a degradation of the cavity *Q* is expected. This is due to an additional source of losses contributed by the fiber taper, as the measurement is now of the coupled fiber-cavity system. However, the losses introduced by the presence of the fiber taper can be mitigated by careful selection of the contact parameters. The first parameter we adjust is the contact length of the fiber loop on the nanobeam. The presence of the fiber on the nanobeam introduces a loss channel. Hence, longer contact length between the fiber loop and the nanobeam reduces the *Q*. The fiber taper loop is brought in toward the nanobeam using small steps on a motorized actuator. At some critical distance from the sample surface, Van der Waals and electrostatic forces pull the fiber taper in, causing it to stick to the surface. Once the loop is in contact with the nanobeam, the actuator can still be advanced, increasing pressure and the contact length between the fiber taper and the nanobeam. The actuator can also be pulled away slowly while the loop is still stuck to the surface, decreasing the contact length. After sufficient force is applied to pull the loop away by overcoming the sticking force, it pops off the surface of the sample.

The second parameter we adjust is the contact position along the length of the nanobeam. We have confirmed that the weakest coupling, and therefore the highest *Q*, is observed when contact is made as close as possible to the edge of the nanobeam, whereas contact in the center of the nanobeam produces the strongest coupling and hence the lowest *Q*. Contact in the center of the nanobeam also modifies the local index of refraction in the vicinity of the cavity, which changes the effective index of the cavity mode and leads to a shift in the resonance frequency. The extra loss due to the presence of the fiber taper in the center of the nanobeam and subsequent degradation of the *Q* is dramatic. Figure 4 shows a plot of cavity

#131274 - $15.00 USD Received 7 Jul 2010; revised 3 Sep 2010; accepted 4 Sep 2010; published 13 Sep 2010

mode resonant wavelength and *Q* as a function of position on a high-*Q* nanobeam. Clearly one wants to avoid contact with the center of the nanobeam for measuring high *Q*s. Because the coupling between fiber and nanobeam decreases away from the center of the nanobeam, we found that on very high *Q* nanocavities it is not possible to take *Q* measurements all the way to the edge of the nanobeam. This is the case with the nanobeam studied in Figure 4, where the measurements extend between ±4 μm, whereas the nanobeam extends to ±6 μm. Measurements more than 4 μm from the center of this nanobeam yielded no perceptible dip in transmission. On lower *Q* nanocavities the measurements can usually be taken up to the very edge of the nanobeam. This observation is consistent with the fact that on high *Q* nanocavities the electric field is more tightly confined toward the center of the nanobeam.

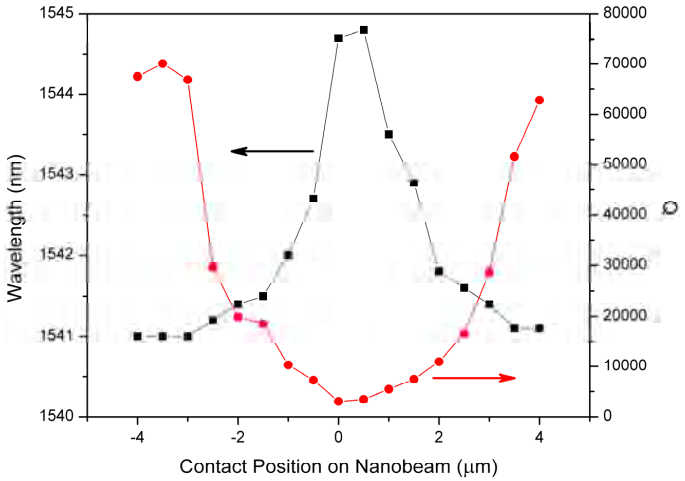

Figure 4. Fiber loop transmission measurements as a function of position on a typical nanobeam cavity at 45º (center of nanobeam corresponds to 0 μm and the attached edges to ±6 μm), cavity mode resonant wavelength (black squares) and *Q* (red circles).

The third parameter we adjust is the angle between the fiber taper and the axis of the nanobeam cavity. Because the polarization of the input field is always perpendicular to the axis of the fiber, the angle between the fiber and the nanobeam will affect the coupling to the mode of the nanobeam, which is linearly polarized perpendicular to the axis of the nanobeam. One would expect that the best polarization matching would occur when the nanobeam is aligned parallel to fiber. However, this configuration also produces the strongest coupling between the field in the fiber and the nanocavity, as well as the largest index modification in the vicinity of the cavity. Even when the contact is made at the edge of the nanobeam, the length of the contact region between the fiber and the nanobeam extends over a large fraction of the nanobeam. Hence, this configuration produces a deep dip in the transmitted signal, but does not yield the highest measured *Q*s. One might think that the perpendicular configuration between the fiber and the nanobeam would yield the highest *Q*s because of minimized contact between them as well as minimal coupling into the nanobeam. However, because of the drastically reduced coupling in the perpendicular configuration due to orthogonal polarizations, we were not able to observe any cavity modes in that configuration at the edge of the nanobeam. The highest *Q*s result with an angle ranging from 20º to 60º between the fiber taper and the nanobeam, and contact made at the edge of the nanobeam. This configuration reduces the physical contact between the fiber and the nanobeam compared to the parallel configuration, but still supports a polarization component that is matched to the

#131274 - $15.00 USD Received 7 Jul 2010; revised 3 Sep 2010; accepted 4 Sep 2010; published 13 Sep 2010

nanobeam mode. The highest Q we measured was 75,000 with a computed mode volume of $0.27(\lambda/n)^3$ in the 45º, edge configuration, yielding Q/V = 278,000. As far as we know, this yields the highest Q/V ratio that has been achieved on nanobeam cavities on substrate. The group of De La Rue [14] reported a Q of 147,000 with a computed mode volume of $0.85(\lambda/n)^3$, yielding Q/V = 173,000. Figure 3 (b) shows the spectrum of the highest Q nanobeam cavity mode.

5. Comparison to resonant scattering

As mentioned earlier, the presence of a fiber taper in contact with a nanobeam cavity provides an additional loss mechanism for light in the cavity. While this allows us to probe the Q of the system by measuring the transmission through the fiber, it also reduces the Q compared to the inherent Q that the cavity would have by itself. In order to investigate this loss mechanism, we have compared the results of measurements with the fiber taper loop to measurements performed by cross-polarized resonant scattering, as shown in Figure 5. [7-8, 11].

Cavity modes measured using resonant scattering are known to exhibit asymmetric lineshapes [15]. These lineshapes are attributed to a Fano interference between the resonantly scattered light and the coherent background. In order to extract a linewidth from such an asymmetric profile, we fit the signal to a Fano lineshape:

$$F(\omega) = A_0 + F_0 \frac{\left[q + 2(\omega - \omega_0)/\Gamma\right]^2}{1 + \left[2(\omega - \omega_0)/\Gamma\right]^2} \tag{1}$$

where ω_0 is the frequency of the cavity mode transition, Γ is the resonance linewidth, A_0 and F_0 are offset and scaling factors, respectively, and q is the Fano parameter that quantifies the asymmetry of the lineshape. Adjusting these parameters to fit a curve to our resonant scattering data, we are able to extract the underlying linewidth, and hence Q of the cavity mode. Such a fit is shown in Figure 5 (b), using Equation (1) with fit parameters A_0 = 0.658, F_0 = 0.054, q = 0.6, ω_0 = 30.9 *THz* and Γ = *0.7 GHz*. Galli, et al have reported [15] that the asymmetry of the lineshape from resonant scattering data can be varied by changing the spot size of the laser beam on the sample.

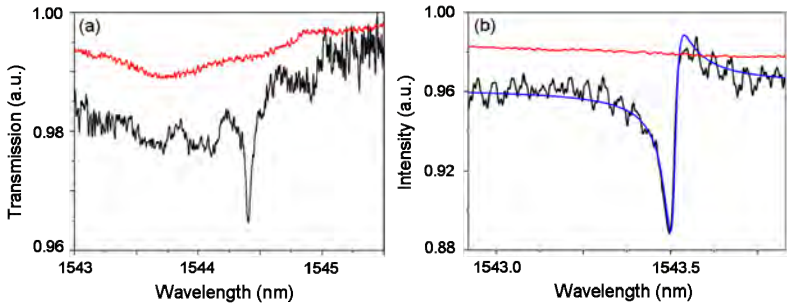

Figure 5. (a) Fiber loop transmission spectrum of a typical nanobeam cavity, Q = 29,000 (black) and spectrum directly from laser (red). (b) Cross-polarized resonant scattering signal of the same nanobeam cavity as (a), Q = 44,100 (black); fitted Fano lineshape (blue); spectrum directly from laser (red).

Cavity modes measured using the fiber taper also displayed asymmetric lineshapes, which we attribute to interference between two pathways: light interacting with the cavity mode and emitted back into the fiber and light coupled into the 2D slab. However, unlike the case with the resonant scattering technique, the asymmetry of the lineshape with the fiber taper

#131274 - $15.00 USD Received 7 Jul 2010; revised 3 Sep 2010; accepted 4 Sep 2010; published 13 Sep 2010

technique is strongly dependent on polarization. Hence, it was always possible to tune the polarization such that the resulting lineshape was symmetric, and this allowed us to directly fit a Lorentzian lineshape in order to extract the *Q*, without resorting to the more complicated fitting associated with the Fano Equation (1). The *Q*s measured using the resonant scattering technique were higher than those measured for the same cavity using the 45º fiber configuration at the edge of the nanobeam, consistent with the idea that the presence of the fiber loop lowers the *Q* by introducing an additional loss mechanism. The loss induced by the presence of the fiber taper is typically substantial, as the difference in *Q*s that we observed using the two methods showed the fiber loop measurement to be 38% lower on average than the resonant scattering measurement.

How do the two systems compare in other ways? The fiber taper loop measurement is more difficult to set up than the resonant scattering measurement, primarily because of the equipment and experience needed to successfully taper and curve the microfibers. Once the measurement is set up, the fiber taper loop measurement is quite robust and does not suffer from the extreme sensitivity to variations in alignment of the resonant scattering technique. Both measurements can be performed at room temperature or at cryogenic temperatures; however, the fiber taper measurement would require extensive modifications to most cryostats in order to insert the fiber taper and control its motion. In contrast, the resonant scattering technique can be performed with all of the optics outside of the cryostat. The fiber taper measurement is performed in an all-fiber configuration, whereas the resonant scattering method is performed in free space. We found that absorption lines due to atmospheric nitrogen in the spectral region of our nanobeam cavity modes also appear as dips in the measured resonant scattering spectrum. In order to accurately measure the *Q* of a cavity mode coincident with an absorption dip, as was unfortunately the case for the $Q = 75{,}000$ cavity in Fig. 3 (b), the mode would need to be spectrally shifted away from the absorption dip by a technique such as heating or condensation of xenon or nitrogen gas [16].

6. Conclusion

In conclusion, we have measured the *Q*s of 1D photonic crystal nanobeam cavities on substrate using the transmitted signal through a fiber taper loop. Using this technique, we have measured a *Q* as high as 75,000 with a computed mode volume of $0.27(\lambda/n)^3$, representing the highest *Q*/V ratio reported in this system. We have observed dependence of the measured *Q* on contact position and length between the nanobeam and the fiber taper, angle between the nanobeam and the fiber taper, and polarization of the light in the fiber. We have observed that higher *Q*s are measured when the fiber loop is contacted at the edge of the nanobeam and with a 20º to 60º angle between the fiber loop and the nanobeam. We have shown that the fiber taper loop technique is capable of measuring high *Q*s, and that by tuning the polarization in the fiber it is possible to eliminate the asymmetric lineshapes.

Acknowledgments

The USA authors would like to acknowledge support (EEC-0812072) from the National Science Foundation (NSF) through the Engineering Research Center for Integrated Access Networks (CIAN). The Tucson group also acknowledges support from NSF Atomic Molecular and Optical Physics (AMOP) and Electronics, Photonics and Device Technologies (EPDT), AFOSR, and Arizona Technology & Research Initiative Funding (TRIF). The Caltech authors gratefully acknowledge critical support and infrastructure provided for this work by the Kavli Nanoscience Institute at Caltech. HMG thanks the Alexander von Humboldt Foundation for a Renewed Research Stay. AH appreciates the generous support of the ARCS Foundation. The Tucson group thanks the groups of Prof. Jelena Vučkovíc and Prof. Edo Waks for helpful discussions regarding the resonant scattering technique. The authors thank Pavel Polynkin for the use of his Agilent mainframe and tunable laser.

#131274 - $15.00 USD Received 7 Jul 2010; revised 3 Sep 2010; accepted 4 Sep 2010; published 13 Sep 2010

Appendix B

Progress in growth, fabrication, and characterization semiconductor photonic crystal nanocavities

B. C. Richards, J. Hendrickson, J. D. Olitzky, R. Gibson, M. Gehl, K. Kieu, P. Polynkin, G. Khitrova, H. M. Gibbs, U. K. Khankhoje, A. Homyk, A. Scherer, J.-Y. Kim, Y.-H. Lee

Physica Status Solidi B, Vol. 248, No. 2, pp. 892-896 (April, 2011)

Phys. Status Solidi B **248**, No. 4, 892–896 (2011) / **DOI** 10.1002/pssb.201000853

physica status solidi b
www.pss-b.com
basic solid state physics

Progress in growth, fabrication, and characterization of semiconductor photonic crystal nanocavities

B. C. Richards*[,1], J. Hendrickson[1], J. D. Olitzky[1], R. Gibson[1], M. Gehl[1], K. Kieu[1], P. Polynkin[1], G. Khitrova[1], H. M. Gibbs[1], U. K. Khankhoje[2], A. Homyk[2], A. Scherer[2], J.-Y. Kim[3], and Y.-H. Lee[3]

[1] College of Optical Sciences, University of Arizona, 1630 E. University Blvd., Tucson, AZ 85705, USA
[2] Electrical Engineering, California Institute of Technology, 1200 E. California Blvd., Pasadena, CA 91125, USA
[3] Department of Physics, Korea Advanced Institute of Science and Technology, 373-1 Guseong-dong, Yuseong-gu, Daejeon 305-701, Republic of Korea

Received 14 August 2010, accepted 18 September 2010
Published online 24 December 2010

Keywords microcavities, nanophotonics, photonic crystals

* Corresponding author: e-mail brichards@optics.arizona.edu, Phone: +01 520 621 9606, Fax: +01 520 621 4358

We present the results of recent investigations into the fabrication and characterization of high-Q, small mode volume one-dimensional photonic crystal nanobeam cavities in Si and two-dimensional photonic crystal slab nanocavities in GaAs. The nanobeam cavity modes are investigated in transmission by means of a microfiber taper loop apparatus. The spectral transmission profile of the cavity modes is investigated as a function of input polarization into the fiber. The Q of the cavity for different positions and orientations of the fiber taper is investigated. The results are compared to measurements by resonant scattering. The slab nanocavities are investigated by means of quantum dot photoluminescence excitation spectroscopy. We present recent progress in growth and fabrication of such slab nanocavities.

1 Introduction Cavity QED experiments in semiconductors require high quality-factor (Q) and low mode volume nanocavities for confining the electromagnetic field. Photonic crystals have emerged in recent years as a popular system for investigating fundamental light–matter interactions in the QED regime, and have been employed in the observation of several fundamental quantum optics results [1–3]. An important figure of merit for such cavity systems is the ratio Q/V, where V is the effective mode volume of the cavity. Higher values of Q lead to longer photon lifetimes in the cavity (improved chance of light–matter interaction), and smaller values of V lead to higher field intensities (stronger light–matter interaction). The importance of the ratio Q/V can be seen in the expression for Purcell enhancement ($F_p \propto Q/V$) of spontaneous emission and for vacuum Rabi splitting (VRS $\propto Q/\sqrt{V}$) [1, 2, 5–7]. The pursuit of high Q, small V nanocavities has thus been a major focus of efforts in the semiconductor cavity QED community.

Several experimental techniques have been developed and utilized for the purpose of measuring the Qs of photonic crystal nanocavities. The most common technique consists of photoluminescence spectroscopy when the cavity contains active emitters such as quantum dots. This technique usually requires liquid helium temperatures, and also suffers from broadening (narrowing) of the cavity linewidths at low (high) powers due to absorption (gain) by the quantum dots [4]. Two more recent techniques have been developed specifically for the investigation of semiconductor cavity QED systems: a cross-polarized resonant scattering method [8, 9] and a tapered optical microfiber [10, 11]. These two techniques allow the measurement of empty cavity Qs, and hence can be performed at room temperature and without active emitters.

We report the results of our investigations of 1D photonic crystal nanobeam cavities by means of the fiber taper method, and compare the results to those obtained by the resonant scattering method. We observe that the cavity Qs depend on polarization of the light in the fiber, of contact position on the nanobeam, and of angle between the nanobeam and the fiber [12]. We also present recent progress in the growth and fabrication of 2D photonic crystal slab nanocavities in GaAs with InAs QDs [6, 7].

Original Paper

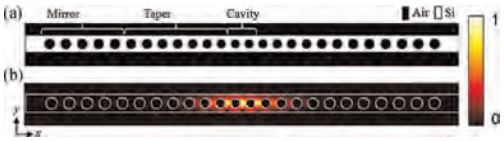

Figure 1 (online color at: www.pss-b.com) (a) Top view of cavity design. (b) Normalized computed electric field profile showing cavity region.

2 Design and fabrication

2.1 Design The first cavity investigated in this study is a photonic crystal nanobeam cavity, which is essentially a wavelength-scale Fabry–Perot etalon formed by sandwiching a 1D photonic crystal waveguide between 1D photonic crystal Bloch mirrors, as shown in Fig. 1. In the transverse directions, the light is confined in the nanobeam by total internal reflection. By smoothly tapering the air hole radius and the corresponding lattice constants in the mirror sections, the scattering loss is minimized and a high Q is achieved [13–15]. 3D finite-difference time-domain (FDTD) simulations [16] reveal that the cavity exhibits a reasonably high Q in excess of 500 000 with very low mode volumes, even though it is placed on a low index substrate. The region of tapered holes in the center of the nanobeam effectively confines the light, analogous to a Fabry–Perot spacer.

2.2 Fabrication The nanobeams are fabricated using electronics grade silicon-on-insulator with a 220 nm silicon device layer and 2 μm buried oxide. To prepare the samples for electron-beam lithography, the wafers are manually cleaved, cleaned with acetone and isopropanol, and the native oxide is removed by a short dip in 10:1 buffered hydrofluoric acid. The samples are then baked at 180 °C, spin-coated with 2% PMMA 950 K in chlorobenzene, and baked again at 180 °C for 5 min. Electron-beam lithography is performed in a Leica EBPG 5000+ at 100 kV. Following electron-beam exposure, the samples are developed in 1:3 MIBK/IPA for 60 s, rinsed in IPA, and dried with nitrogen. After development, the wafers are etched using an Oxford Instruments Plasmalab System100 ICP380 with a mixed-mode gas chemistry consisting of SF_6 and C_4F_8. Figure 2 shows an SEM of one of our nanobeam cavities.

3 Fiber taper loop apparatus

Our nanobeams were investigated by means of a transmission measurement through a tapered microfiber loop that was brought into physical contact with the nanobeam. The tapered region of the fiber is 1–1.5 μm in diameter, and the taper loop has a radius of curvature of 200 μm. The taper loop is produced in two stages, first by heating and pulling a standard single mode optical fiber into a taper, and then by forming the tapered region into a loop in a specially built curving apparatus. The fiber is then glued to a microscope slide in such a way that the loop extends beyond the edge of the slide, and the motion of this assembly is controlled by means of a computer controlled, motorized *xyz* stage.

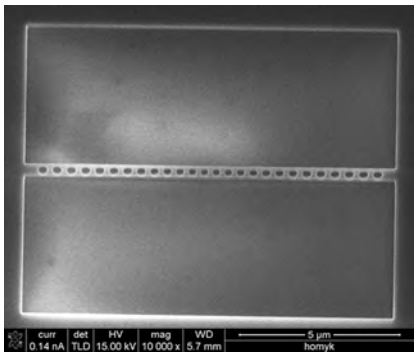

Figure 2 SEM of typical nanobeam cavity.

A beam from an Agilent 8164A mainframe with an Agilent 81682A tunable laser with 0.2 nm wavelength resolution propagates through the fiber and is detected at the output end by means of an InGaAs photodiode. An in-line polarization controller is installed between the laser and the tapered region. The wavelength of the laser is swept across a region of interest, and the output is recorded by a computer. When the tapered loop is moved into physical contact with a nanobeam, light that is propagating through the fiber can be coupled into the mode of the nanocavity, and the resulting interaction is observed as a change in the transmission spectrum output. The laser for this measurement must have a linewidth smaller than the FWHM of a cavity mode, and it must have amplitude fluctuations which are slow compared to the time necessary to scan across a mode. The Q is given by the wavelength of the cavity mode divided by the FWHM of the cavity mode. Figure 3a shows a schematic of the

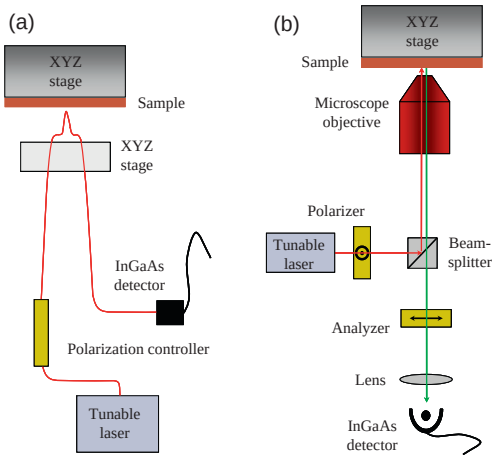

Figure 3 (online color at: www.pss-b.com) (a) Experimental setup for fiber taper loop measurement. (b) Experimental setup for resonant scattering measurement.

physica status solidi b

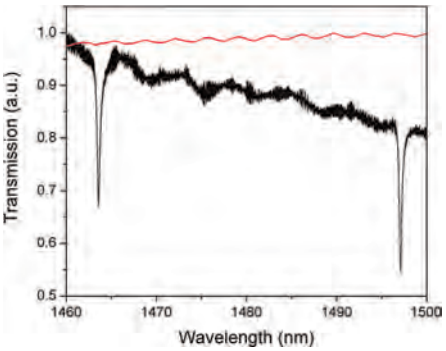

Figure 4 (online color at: www.pss-b.com) Fiber loop transmission spectrum of typical nanobeam cavity at 45°, center contact (black), and spectrum directly from laser (red).

apparatus. Figure 4 shows a typical transmission spectrum of a nanobeam taken with the fiber taper loop apparatus.

4 Coupling to a nanobeam

4.1 Polarization The nanobeams are designed to support a mode which is linearly polarized in a direction perpendicular to the axis of the nanobeam. In order to effectively couple into the cavity mode, the field in the fiber must have a polarization component parallel to the mode of the cavity. Our in-line polarization controller allows us to tune the polarization of the field, and hence control the coupling into the cavity. There are several pathways that the field can travel, each dependent upon the polarization: it can be coupled into the substrate, or it can be scattered back into the fiber in either the forward or the backward direction. As a result of these multiple pathways, we expect to observe interference effects which depend upon the polarization of the incident field, and hence the strength of the coupling into the available channels. We did observe such interference effects, which caused the lineshape of the cavity mode transmission to vary as a function of input polarization, resulting in asymmetric lineshapes. However, by tuning the polarization we were always able to achieve a symmetric lineshape of the transmitted signal.

4.2 Contact pressure The fiber taper loop is brought into contact with the nanobeam, and the motion of the loop is controlled by a motorized *xyz* stage. As the loop comes near to the surface of the sample, electrostatic and Van der Waals forces pull the fiber into the sample, causing it to stick to the nanobeam.

Once the taper loop is in contact with the nanobeam, it can still be advanced or retracted by the actuators, allowing us to adjust the pressure with which the fiber loop contacts the nanobeam. Increased pressure increases the contact length between the fiber taper and the nanobeam, and hence affects the coupling between them, and decreased pressure caused by pulling the taper away likewise decreases the contact length. At some point as the loop is pulled away it pops off the surface of the nanobeam.

Because the contact between the nanocavity and the fiber taper introduces another loss mechanism for light to escape from the cavity, we expect the strength of coupling between the two to affect the measured Q of the cavity. Specifically, if the coupling between the two systems is very strong, we expect to observe lower Qs, and hence the optimal configuration for observing the highest Qs will be the configuration that minimizes the coupling between the fiber taper and the nanobeam, while still allowing enough interaction to observe a change in transmission through the fiber. This expectation was confirmed by our observation of the pressure and contact length affecting the measured Qs of our cavities. To measure the highest Q, it is important to minimize the contact length between the nanobeam and the fiber taper.

4.3 Contact position As seen in Fig. 1, the field profile of the cavity mode is concentrated near the center of the nanobeam. As a result, we expect the coupling between the fiber loop and the nanobeam to depend on the position along the length of the nanobeam at which contact is made: contact at the center should result in the strongest coupling, and contact at the edge should result in the weakest coupling. We confirmed that this is in fact the case, and that to measure the highest Qs, the taper loop should be brought into contact as close to the edge of the nanobeam as will still produce a modification in the transmission. Contact near the center of the nanobeam also produces a modification of the refractive index in the environment of the cavity mode, resulting in a shift of the wavelength of the observed resonance.

4.4 Contact angle Because the polarization of the cavity mode is always linearly polarized in the same direction, the coupling between the fiber taper and the cavity mode can also be varied by changing the angle between the fiber taper loop and the axis of the nanobeam. The sample itself is mounted on a rotary stage that allows us to rotate the sample about an axis normal to the sample surface. Whereas the polarization controller only allows control over the polarization along the axis of the fiber, rotating the sample with respect to the fiber provides another degree of control over the coupling.

When the fiber is oriented parallel to the nanobeam, we expect that the field polarization can always be tuned such that it has a component parallel to the mode of the cavity where the coupling between them will be the strongest. Alternatively, when the fiber taper is contacted in a configuration perpendicular with respect to the nanobeam, we would expect that the field never has a component parallel to the cavity mode, and hence coupling between the two will be minimal.

We found that in the parallel configuration, the coupling was indeed the strongest, and the Q the lowest. As we tuned the angle between the nanobeam and the fiber away from parallel, the Q improved, but at angles close to the

Original Paper

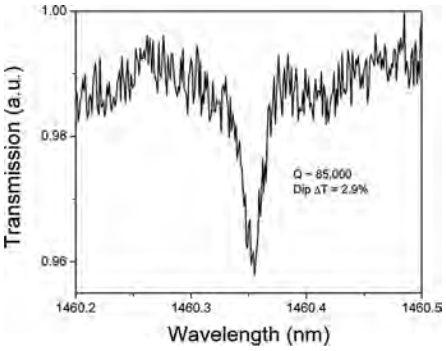

Figure 5 Fiber loop transmission spectrum of high-Q cavity mode, at 45°, edge contact, with $Q = 85\,000$.

perpendicular configuration, there was not enough coupling to observe a change in the transmitted signal.

4.5 Results The highest Qs were observed with an angle of the fiber taper between 20 and 60° with respect to the nanobeam axis, and contact made at the edge of the nanobeam. This configuration minimizes the contact between the loop and the nanobeam, but still supports a polarization component corresponding to the cavity mode. The highest Q measured in our system was 85 000, which with a computed mode volume of $0.27(\lambda/n)^3$, yields Q/V of 315 000, which we believe to be the highest Q/V reported in nanobeams on substrate. The group of De La Rue [17] reported a Q of 147 000 with a computed mode volume of $0.85(\lambda/n)^3$, yielding Q/V of 173 000. Figure 5 shows the transmission spectrum of our highest Q cavity mode.

5 Comparison to resonant scattering Another method commonly used for measuring the Qs of semiconductor nanobeam cavities is a cross-polarized resonant scattering technique [8, 9], shown in Fig. 3b. Whereas the fiber taper measurement introduces an additional loss mechanism to the cavity, and hence lowers the Q, the resonant scattering technique does not affect the Q of the cavity, and hence provides a more accurate measurement of the intrinsic Q. We compared the two techniques and found that the Qs measured by resonant scattering were higher than those measured on the same cavity by fiber taper loop. However, the resonant scattering technique also suffers from some drawbacks. First, in the spectral region of our cavity modes and within the range of our tunable laser, 1460–1580 nm, there is a number of absorption lines due to atmospheric nitrogen, which also appear as dips in the detected signal similar to the cavity modes of the nanobeams. If one of these lines is spectrally coincident with the mode of a cavity, it is not possible to distinguish the dip of the cavity mode from the dip due to nitrogen absorption. This was unfortunately the case with our highest Q cavity of 85 000 that was measured with the fiber taper. In order to overcome this difficulty, the cavity mode would have to be tuned away from the nitrogen resonance, for instance by heating or by condensation of xenon or nitrogen gas [18]. Second, the resonant scattering method is known to exhibit asymmetric lineshapes. This is attributed to a Fano interference between the resonantly scattered light and the coherent background, and requires that a Fano lineshape be fit to the data in order to determine the cavity Q. Galli et al. have reported [19] that the asymmetry of the lineshape can be changed by changing the spot size of the incident laser beam.

In addition to these considerations, the two methods also differ in ease of setup and use. The fiber taper loop is very robust and easy to use once it is set up; however, the fabrication of the fiber taper loop itself requires special equipment and experience. The resonant scattering method can be set up with standard optical laboratory components and instruments, but it is extremely sensitive to alignment and hence more difficult to use. Both methods are useful at room temperature as well as at cryogenic temperatures, but the fiber loop measurement would require substantial modification to most cryostats for low temperature measurements. The resonant scattering measurement does not require components inside the cryostat.

6 2D GaAs slab nanocavities While nanocavities in silicon achieve very high Qs, GaAs remains the system of choice for quantum optics experiments because of the ease of incorporating active emitters, such as InAs QDs, which has so far remained elusive for Si. The majority of our research focuses on the GaAs/InAs 2D photonic crystal slab system for the purpose of quantum optics experiments. However, in spite of extensive efforts by the cavity QED community aimed at reaching high Qs at shorter wavelengths in GaAs PC nanocavities, the results have been disappointing compared to what has been achieved at longer wavelengths in GaAs [20] and Si.

In the course of work toward optimizing the growth and fabrication of such GaAs 2D nanocavities, AFM of the sample surface was used extensively for characterizing the quality of the growth. We found, that even on samples where AFM showed a smooth surface, TEM images revealed that the top of the AlGaAs sacrificial layer could be very rough, with the roughness larger along one crystal axis. Changing certain MBE growth parameters reduced the roughness, but this did not result in a noticeable increase in Q [7], indicating that other loss mechanisms are still holding down the Qs. With future improvements in fabrication, we expect the smoothness of the AlGaAs layer to be significant.

Investigations of the sample surfaces by AFM and SEM also revealed debris on the surface of the samples that we believed to be an artifact of the HF acid wet etch. A 140 s dip in a KOH solution removed the debris, confirming that it was most likely a hydroxide of aluminum generated during the wet etch. The measured Qs of the cavities did improve noticeably following the removal of this debris, by an average of 50% on 10 different nanocavities, and the intensity of the photoluminescence also increased [7].

physica status solidi b

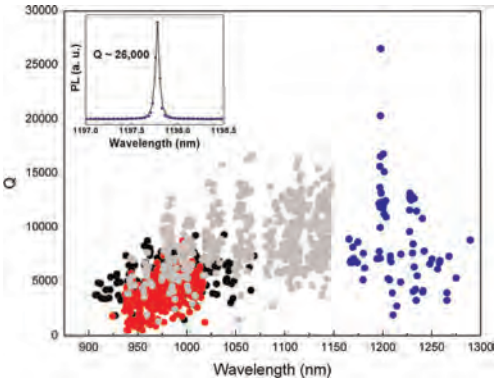

Figure 6 (online color at: www.pss-b.com) Scatter plot of *Q*s from four different samples: QD24-3 (black), QD25-3 (red), A0961-3 (gray), and QD58-1 (blue).

Such improvements in growth and fabrication have yielded modest improvements in the *Q*s we have been able to achieve. Nevertheless, we still consistently observe that even our best samples show lower *Q*s as wavelength decreases. Figure 6 shows *Q* versus wavelength data for several 100 nanocavities from four of our best samples covering a broad wavelength range from 900 to 1300 nm. The data show a decisive decrease in *Q* in the shorter wavelength region. The highest *Q* measured was 26 000, and the PL spectrum for this nanocavity is shown in the inset to Fig. 6.

7 Conclusion We have succeeded in measuring the *Q*s of photonic crystal nanobeam cavities using a fiber taper loop, and have observed *Q*s as high as 85 000, which yields the highest *Q*/*V* ratio reported in these devices on substrate. We have observed that the results of this technique depend on strength of contact between the fiber and the nanobeam, incident field polarization, contact position on the nanobeam, and angle between the fiber loop and the nanobeam. We compared our results to the cross polarized resonant scattering method, and found that the fiber loop does lower the *Q*s, but that the effect can be minimized and high *Q*s can still be measured by choosing the above parameters appropriately.

Acknowledgements The USA authors would like to acknowledge support (EEC-0812072) from the National Science Foundation (NSF) through the Engineering Research Center for Integrated Access Networks (CIAN). The Tucson group also acknowledges support from NSF Atomic Molecular and Optical Physics (AMOP) and Electronics, Photonics, and Device Technologies (EPDT), AFOSR, and Arizona Technology & Research Initiative Funding (TRIF). The Caltech authors gratefully acknowledge critical support and infrastructure provided for this work by the Kavli Nanoscience Institute at Caltech. H. M. G. thanks the Alexander von Humboldt Foundation for a Renewed Research Stay. A. H. appreciates the generous support of the ARCS Foundation.

References

[1] T. Yoshie, A. Scherer, J. Hendrickson, G. Khitrova, H. M. Gibbs, G. Rupper, C. Ell, O. B. Shchekin, and D. G. Deppe, Nature **432**, 200–203 (2004).
[2] D. Englund, D. Fattal, E. Waks, G. Solomon, B. Zhang, T. Nakaoka, Y. Arakawa, Y. Yamamoto, and J. Vuckovic, Phys. Rev. Lett. **95**, 013904 (2005).
[3] D. Press, S. Gotzinger, S. Reitzenstein, C. Hofman, A. Loffler, M. Kamp, A. Forchel, and Y. Yamamoto, Phys. Rev. Lett. **98**, 117402 (2007).
[4] J. Hendrickson, B. C. Richards, J. Sweet, S. Mosor, C. Christenson, D. Lam, G. Khitrova, H. M. Gibbs, T. Yoshie, A. Scherer, O. B. Shchekin, and D. G. Deppe, Phys. Rev. B **72**, 193303 (2005).
[5] G. Khitrova, H. M. Gibbs, M. Kira, S. W. Koch, and A. Scherer, Nature Phys. **2**, 81–90 (2006).
[6] U. K. Khankhoje, S.-H. Kim, B. C. Richards, J. Hendrickson, J. Sweet, J. D. Olitzky, G. Khitrova, H. M. Gibbs, and A. Scherer, Nanotechnology **21**, 065202 (2010).
[7] J. Sweet, B. C. Richards, J. D. Olitzky, J. Hendrickson, G. Khitrova, H. M. Gibbs, D. Litvinov, D. Gerthsen, D. Z. Hu, D. M. Schaadt, M. Wegener, U. Khankhoje, and A. Scherer, Photon. Nanostruct. Fundam. Appl. **8**, 1–6 (2010).
[8] M. W. McCutcheon, G. W. Rieger, I. W. Cheung, J. F. Young, D. Dalacu, S. Frédérick, P. J. Poole, G. C. Aers, and R. L. Williams, Appl. Phys. Lett. **87**, 221110 (2005).
[9] D. Englund, A. Faraon, I. Fushman, N. Stoltz, P. Petroff, and J. Vučković, Nature **450**, 857–861 (2007).
[10] K. Srinivasan, P. E. Barclay, M. Borselli, and O. Painter, Phys. Rev. B **70**, 081306(R). (2004).
[11] I.-K. Hwang, G.-H. Kim, and Y.-H. Lee, IEEE J. Quantum Electron. **42**, 131–136 (2006).
[12] B. C. Richards, J. Hendrickson, J. D. Olitzky, R. Gibson, M. Gehl, K. Kieu, U. K. Khankhoje, A. Homyk, A. Scherer, J.-Y. Kim, Y.-H. Lee, G. Khitrova, and H. M. Gibbs, Opt. Express **18**, 20558–20564 (2010).
[13] P. Deotare, M. McCutcheon, I. Frank, M. Khan, and M. Loncăr, Appl. Phys. Lett. **94**, 121106 (2009).
[14] C. Sauvan, P. Lalanne, and J. Hugonin, Phys. Rev. B **71**, 1–4 (2005).
[15] E. Kuramochi, H. Taniyama, T. Tanabe, K. Kawasaki, Y.-G. Roh, and M. Notomi, Opt. Express **18**, 15859–15869 (2010).
[16] A. Oskooi, D. Roundy, M. Ibanescu, P. Bermel, J. Joannopoulos, and S. Johnson, Comput. Phys. Commun. **181**, 687702 (2010).
[17] A. R. M. Zain, N. P. Johnson, M. Sorel, and R. M. De La Rue, Opt. Express **16**, 12084–12089 (2008).
[18] S. Mosor, J. Hendrickson, B. C. Richards, J. Sweet, G. Khitrova, H. M. Gibbs, T. Yoshie, A. Scherer, O. B. Shchekin, and D. G. Deppe, Appl. Phys. Lett. **87**, 141105 (2005).
[19] M. Galli, S. L. Portalupi, M. Belotti, L. C. Andreani, L. O'Gaolain, and T. F. Krauss, Appl. Phys. Lett. **94**, 071101 (2009).
[20] S. Combrié, A. De Rossi, Q. V. Tran, and H. Benisty, Appl. Phys. Lett. **87**, 141105 (2005).

Appendix C

InAs quantum dot site-selective growth on GaAs substrates

J. Hendrickson, M. Helfrich, M. Gehl, D. Hu, D. Schaadt, S. Linden, M. Wegener, B. Richards, H. Gibbs, G. Khitrova

Physica Status Solidi C, Vol. 8, No. 4, pp. 1242-1245 (April, 2011)

Phys. Status Solidi C **8**, No. 4, 1242–1245 (2011) / **DOI** 10.1002/pssc.201000850

physica status solidi c
www.pss-c.com
current topics in solid state physics

InAs quantum dot site-selective growth on GaAs substrates

Joshua Hendrickson[*,1], Mathieu Helfrich[2,3], Michael Gehl[1], Dongzhi Hu[3], Daniel Schaadt[2,3], Stefan Linden[4], Martin Wegener[2,3], Benjamin Richards[1], Hyatt Gibbs[1], and Galina Khitrova[1]

[1] College of Optical Sciences, University of Arizona, 1630 E. University Blvd, Tucson, AZ 85721, USA
[2] Institute of Applied Physics, Karlsruhe Institute of Technology (KIT), Wolfgang-Gaede-Straße 1, 76131 Karlsruhe, Germany
[3] DFG-Center for Functional Nanostructures (CFN), Karlsruhe Institute of Technology (KIT), Wolfgang-Gaede-Straße 1, 76131 Karlsruhe, Germany
[4] Institute of Physics, University of Bonn, Nußallee 12, 53115 Bonn, Germany

Received 13 August 2010, revised 14 October 2010, accepted 15 October 2010
Published online 1 February 2011

Keywords quantum dot, MBE, deterministic growth, annealing

* Corresponding author: e-mail jhendrickson@optics.arizona.edu

Photoluminescence (PL) spectra and AFM measurements of InAs quantum dots grown in a site-selective manner on pre-patterned GaAs substrates are presented. A number of processing steps are described including a Ga-assisted deoxidation step to remove native oxides from the sample surface. Furthermore, post growth annealing is shown to be a promising technique for improving the quantum dot density and likelihood of single site-selective nucleation. Morphological transitions are shown to occur during the annealing process with two initial quantum dots in a given nucleation site transforming into one slightly larger quantum dot. Density measurements performed by AFM combined with PL spectroscopic measurements show that we have achieved optically active, site-selective dot growth, and additionally allow us to calculate that our site-selective dots are on average 30% as efficient as unpatterned dots.

1 Introduction Semiconductor quantum dots have been shown to exhibit a number of interesting and useful properties such as photon antibunching [1], resonance fluorescence [2], and generation of entangled photon pairs [3]. This makes them an increasingly popular choice of emitter for single photon sources and quantum information/quantum cryptography devices. Through the coupling of semiconductor quantum dots to various types of cavities even the strong coupling regime of cavity quantum electrodynamics can be reached [4-6]. However, the inherent randomness in the spatial distribution of self-assembled quantum dots grown in the Stranski-Krastanov growth mode makes it difficult to align quantum dots to cavities, waveguides, or any other structures. Often one may simply rely on luck to obtain the correct spatial positioning. Some groups have devised methods of locating a particular quantum dot and then fabricating a device around it [7-9]; however, these are not very scalable methods. To circumvent such problems we have been working towards the deterministic, site-selective growth of quantum dots [10] on pre-patterned substrates.

The method we have chosen for producing site-selective nucleation of semiconductor quantum dots is through the creation of small nanoholes on the substrate surface. Using electron beam lithography and wet chemical etching, arrays of nanoholes having average diameters of 60 nm and AFM measured depths of 20 nm are produced. After cleaning the samples chemically they are reintroduced into the MBE chamber where they undergo a Ga-assisted deoxidation process [11] for the removal of native oxides. Next, the growth of InAs quantum dots occurs followed by an *in-situ* annealing step to help reduce defects, control dot size and density, and increase the probability of single dot nucleation at each pre-defined location. Finally the sample may or may not be capped with GaAs depending upon whether photoluminescence measurements or atomic force microscopy measurements are to be taken.

2 Experimental details

2.1 Nanohole fabrication The fabrication of the nanoholes which will later serve as the nucleation sites

Contributed Article

during quantum dot growth is carried out by first spin coating a layer of PMMA/MA (polymethyl methacrylate/methacrylate) onto a GaAs substrate. Several square arrays of spots with various lattice spacing are then written into the resist by electron beam lithography (Raith e-line, 30 keV). After developing the resist the sample is placed in a solution of H_2SO_4:H_2O_2:H_2O (1:8:800) for 30 s in order to wet chemically etch holes of depth 20 nm into the substrate.

2.2 Sample cleaning The first step in the cleaning process is to remove the remaining resist. This is accomplished through a series of solvent baths including acetone, methanol, and isopropyl alcohol. The sample is then placed into the load lock chamber of a Riber Compact 21T molecular beam epitaxy system where it is held for 1 hour at 130°C in order to desorb any volatile surface contamination. The final cleaning step involves the removal of surface oxides by an *in-situ* Ga-assisted deoxidation process where the sample is heated up to 480 °C and then exposed to a low Ga flux of 1 ML/s. The exposure of Ga is cycled repeatedly for 30 seconds on and 30 seconds off with the As shutter always closed, giving the converted Ga_2O time to desorb from the sample surface. Once the total amount of Ga provided reaches 8 ML the cycling is stopped and the sample temperature is increased to 550 °C and annealed for 2 minutes under As_4 atmosphere to thermally desorb any remaining oxide compounds.

2.3 Quantum dot growth The InAs quantum dot growth process begins with the growth of a 16 nm GaAs buffer layer at 500 °C followed by 1.7 ML of InAs. Using III/V beam equivalent pressure ratios of 1:10 and 1:100, the GaAs and InAs growth rates were determined to be 0.3 ML/s and 0.07 ML/s, respectively. An *in-situ* annealing step is performed immediately after quantum dot growth with the sample being kept at growth temperature for 2:30 min. Afterwards the sample is either rapidly cooled down to room temperature or capped with 80 nm of GaAs. Uncapped samples are used in atomic force microscopy (AFM) measurements in order to determine quantum dot size, density, and distribution while the capped samples are used in photoluminescence measurements in order to discern their optical quality.

3 Results and discussion

3.1 AFM measurements The electron beam lithography and wet chemical etching are able to reliably produce nanoholes with diameters in the range of about 60 nm. Fig. 1 shows an AFM image of the nanoholes, before quantum dot growth. The holes actually appear to be more rectangular then circular due to selective etching of the [111] GaAs sidewall and elongation along the [011] direction. Average hole size was measured as 58.4±6.1 nm.

In Fig. 2 AFM images are shown for two samples where all growth and fabrication parameters were kept constant with the exception of the annealing step. Quantum dot growth is preferentially located at each nucleation site for both samples. The unannealed sample shows a predominance of double dot nucleation at each site. This double dot growth feature is expected to arise from the change in nanohole shape during buffer layer growth [12]. As the buffer layer thickness increases the holes become both wider and shallower and may eventually split into two separate holes, thus increasing the probability of double dot nucleation. The average diameter of the unannealed dots is 49.1±4.4 nm, and the average height is 7.4±0.9 nm.

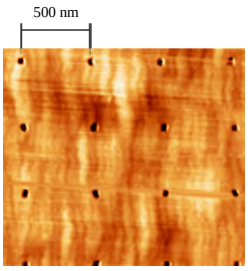

Figure 1 AFM image of nanoholes, before quantum dot growth.

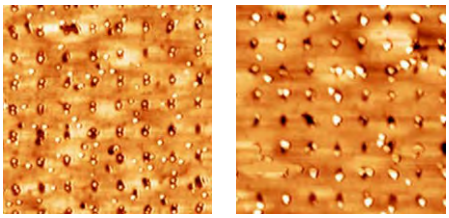

Figure 2 AFM images comparing as grown (left) sample A1083 with annealed (right) sample A1085.

Upon performing the 2:30 minute *in-situ* annealing step, a morphological change in the quantum dots occurs with formerly double dots now transforming into single dots as a consequence of the migration of adatoms. The size of the annealed dots has become larger than those grown without the annealing step, with an average diameter of 82.6±9.5 nm. The size should be controllable by increasing the annealing time which should result in a loss of material resulting in smaller quantum dot size. It is also of interest to note that the number of between-hole quantum dots is decreased from ~45% down to ~30% during the annealing process. This implies that deterministic, site-selectively grown quantum dots are more stable than between-hole quantum dots; indium is preferentially removed from dots between holes and redistributed to the site-selective quantum dots.

There are a number of steps within the process of growing site-selective quantum dots that can adversely

physica status solidi c

affect the outcome. Remnant resist and surface oxide can result in defect holes appearing within the nanohole array. Quantum dot growth must be optimized, along with annealing time, in order to decrease the probability of quantum dot growth between holes. This optimization procedure is still in progress.

3.2 Photoluminescence measurements In addition to growing quantum dots of the correct size and locating them where one wishes, it is also important that the quantum dots are of high enough optical quality to be useful as an emitter. In order to assess the optical quality of the quantum dots, photoluminescence (PL) measurements are performed. The samples of interest are placed into a continuous flow liquid helium cryostat and cooled down to 10 K. A pair of x-y nanopositioners is located within the cryostat, allowing for access to different regions of the sample such as patterned areas with different lattice spacing or unpatterned areas for making comparison measurements. The samples are pumped above band by a HeNe laser beam at 632.8 nm, and the quantum dot emission is collected in reflection geometry using a 100x objective. The PL is then dispersed with a 1.26 m spectrometer and detected with a liquid nitrogen cooled silicon CCD.

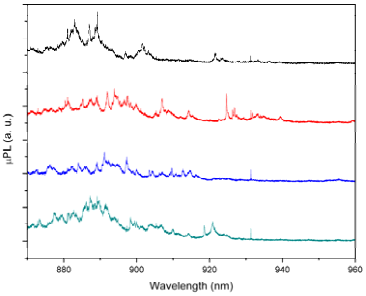

Figure 3 Spectra at four different locations in the unpatterned area of sample A1078 (vertically offset for clarity).

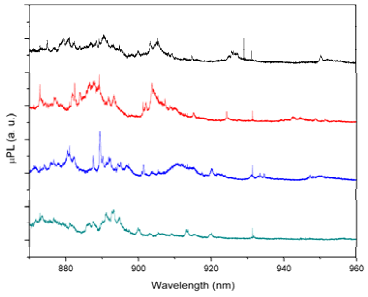

Figure 4 Spectra at four different locations in the patterned area of sample A1078 (vertically offset for clarity).

PL spectra taken at four different locations within the unpatterned (patterned area) of a sample containing a lattice spacing of 250 nm are presented in Fig. 3 (Fig 4). Single quantum dot emission lines can be observed in the spectra with linewidths as narrow as 180 μeV. The spatial resolution of the PL detection is about 1 μm, so it is not possible to distinguish a dot grown in a hole from one grown between holes. Nonetheless, there is statistical evidence that quantum dots grown in holes are emitting PL. Two AFM 5 μm by 5 μm scans of uncapped sample A1083 revealed 746 and 696 quantum dots in an unpatterned region; similarly, on a nearby patterned region with pitch 250 nm, 441 and 484 dots were found between holes and 577 and 576 inside holes. PL data were taken on capped sample A1078 with dots otherwise grown identically as shown in Figs. 3 and 4; integrating the spectra (accounting for detector spectral response) yields $5.15{\cdot}10^5$ counts/mW from the unpatterned region and $4.54{\cdot}10^5$ counts/mW from the patterned region. If quantum dots between holes emit as efficiently as dots in the unpatterned region, then one would expect between-hole dots to emit a PL signal in the ratio of the average number of quantum dots times the unpatterned region PL: $[\{(441 + 484)/2\}/\{(746 + 696)/2\}](5.15{\cdot}10^5$ counts/mW) $= 3.3{\cdot}10^5$ counts/mW. Since the PL coming from the patterned region ($4.54{\times}10^5$ counts/mW) exceeds this number by 38%, the extra light must come from quantum dots grown in the holes.

One can extract an effective quantum efficiency η_{in} (η_{bet}) for quantum dots in holes (between holes) in the patterned region as follows. We also took data as above on the same sample for 500 nm pitch, finding an average number of quantum dots between holes of $N_{bet} = 771.5$, in holes of $N_{in} = 36.5$, and integrated PL spectrum of $PL_{500} = 5.57{\cdot}10^5$ counts/mW. Using $C{\cdot}PL_{500} = \eta_{bet}N_{bet} + \eta_{in}N_{in}$, where C is a proportionality constant, and a similar formula for PL_{250}, we calculate $\eta_{in}/\eta_{bet} = 0.306$. Then from one of these equations and one for the unpatterned region, namely $C{\cdot}PL_{unpatt} = \eta_{unpatt}N_{unpatt}$, one finds $\eta_{bet}/\eta_{unpatt} = 0.996$. These results show that the effective quantum efficiency for dots grown between holes in the patterned region is essentially the same as for dots grown in the unpatterned region, and that the average effective quantum efficiency for dots grown in holes is 30.6% that for dots grown between holes. This method gives us a quantitative measure to evaluate changes we make in electron-beam lithography, etching, cleaning, buffer and quantum dot growth, etc. in an effort to reach our goal of $\eta_{in} = 1$.

These are preliminary results that will be repeated and optimized to increase the ratio of dots in holes to between-hole dots, to increase the PL quantum efficiency, and to reduce the size of the dots as discussed below. However, these results are highly encouraging that dots grown in pre-etched holes are of high enough quality to emit light.

In addition to being of high optical quality it is also of importance that the quantum dots be truly quantum in

Contributed Article

nature; i.e. their photon statistics should display antibunching. The annealing process used here resulted in quantum dots with diameters in the range of 70-90 nm. It is questionable whether or not the second order correlation function for quantum dots of this size will show antibunching. While we have not performed this measurement yet it will be pursued in the future. Furthermore, adjustments in both the annealing process [13] and the amount of deposited InAs should allow for reduction in quantum dot size.

4 Conclusion In conclusion, the site-selective growth of arrays of optically active quantum dots has been demonstrated. An *in-situ* annealing process has been utilized, transforming most double quantum dots into single quantum dots through migration of adatoms and quantum dot ripening, therefore reducing the dot density. Annealing also reduces the number of between-hole quantum dots while maintaining or improving the number of site-selective quantum dots. This implies the site-selective dots are quite stable. Finally, photoluminescence measurements, though not yet spatially resolving an individual site-selective quantum dot, demonstrate statistically that light is emitted by at least some of the site-selective dots.

Acknowledgements The Tucson group would like to acknowledge financial support from the National Science Foundation through the Engineering Research Center for Integrated Access Networks (EEC-0812072), Atomic Molecular and Optical Physics, and Electronics, Photonics and Device Technologies, as well as AFOSR and Arizona Technology & Research Initiative Funding. The Karlsruhe researchers acknowledge support from the Deutsche Forschungsgemeinschaft (DFG) and the State of Baden-Württemberg through the DFG-Center for Functional Nanostructures (CFN) within subproject A2.6.

References

[1] C. Santori, M. Pelton, G. Solomon, Y. Dale, and Y. Yamamoto, Phys. Rev. Lett. **86**, 1502 (2001).
[2] A. Muller et al.,Phys. Rev. Lett. **99**, 187402 (2007).
[3] N. Akopian et al., Phys. Rev. Lett. **96**, 130501 (2006).
[4] T. Yoshie et al., Nature **432**, 200 (2004).
[5] J. P. Reithmaier et al., Nature **432**, 197 (2004).
[6] A. Badolato et al., Science **308**, 1158 (2005).
[7] G. Khitrova, H. M. Gibbs, M. Kira, S. W. Koch, and A. Scherer, Nat. Phys. **2**, 81 (2006).
[8] A. Dousse et al., Phys. Rev. Lett. **101**, 267404 (2008).
[9] S. M. Thon et al., Appl. Phys. Lett. **94**, 111115 (2009).
[10] O. G. Schmidt et al., Surf. Sc. **514**, 10 (2002).
[11] P. Atkinson, S. Kiravittaya, M. Benyoucef, A. Rastelli, and O. G. Schmidt, Appl. Phys. Lett. **93**, 101908 (2008).
[12] S. Kiravittaya, H. Heidemeyer, and O. G. Schmidt, In(Ga)As Quantum Dot Crystals on Patterned GaAs(001) Substrates, in: Lateral Alignment of Epitaxial Quantum Dots, edited by O. G. Schmidt (Springer, 2007).
[13] D. Z. Hu, A. Trampert, and D. M. Schaadt, J. Cryst. Growth **312**, 447 (2010).

Appendix D

Growth and annealing of InAs quantum dots on pre-structured GaAs substrates

M. Helfrich, D. Z. Hu, J. Hendrickson, M. Gehl, D. Rülke, R. Gröger, D. Litvinov, S. Linden, M. Wegener, D. Gerthsen, T. Schimmel, M. Hetterich, H. Kalt, G. Khitrova, H. M. Gibbs, D. M. Schaadt

Journal of Crystal Growth, Vol. 323, No. 1, pp. 187-190 (May, 2011)

Journal of Crystal Growth 323 (2011) 187–190

Contents lists available at ScienceDirect

Journal of Crystal Growth

journal homepage: www.elsevier.com/locate/jcrysgro

Growth and annealing of InAs quantum dots on pre-structured GaAs substrates

M. Helfrich [a], D.Z. Hu [a], J. Hendrickson [b], M. Gehl [b], D. Rülke [a], R. Gröger [c], D. Litvinov [d], S. Linden [e], M. Wegener [a], D. Gerthsen [d], T. Schimmel [c], M. Hetterich [a], H. Kalt [a], G. Khitrova [b], H.M. Gibbs [b], D.M. Schaadt [a,*]

[a] DFG-Center for Functional Nanostructures (CFN) and Institut für Angewandte Physik, Karlsruhe Institute of Technology (KIT), 76131 Karlsruhe, Germany
[b] College of Optical Sciences, University of Arizona, Tucson, AZ 85721, USA
[c] Institute of Nanotechnology (INT) and Institut für Angewandte Physik, Karlsruhe Institute of Technology (KIT), 76131 Karlsruhe, Germany
[d] Laboratorium für Elektronenmikroskopie (LEM), Karlsruhe Institute of Technology (KIT), 76131 Karlsruhe, Germany
[e] Physikalisches Institut, University of Bonn, 53115 Bonn, Germany

ARTICLE INFO

Available online 10 December 2010

Keywords:
A1. Quantum dots
A1. Site-selective growth
A1. Patterning
A1. *In situ* annealing
A3. Molecular beam epitaxy

ABSTRACT

In this study, we investigated the effect of *in situ* annealing on InAs quantum dots site-selectively grown on pre-structured GaAs substrates. A morphological transition is observed with original double dots merging into one single dot during annealing. This is accompanied by a reduction of quantum dots originally nucleating between defined sites. The photoluminescence intensity of annealed site-selective quantum dots is compared to annealed self-assembled dots with linewidths of single dot emission of about 170 and 81 μeV, respectively. UV-ozone cleaning is used to optimize the sample cleaning prior to quantum dot growth.

1. Introduction

Semiconductor quantum dots (QDs) have attracted a lot of attention due to their unique properties during the past two decades. Not only do they exhibit a delta-function-like density of states, which makes them interesting for laser applications, but moreover they can generate entangled photon pairs and act as single photon sources and are thus promising candidates for quantum information schemes [1,2]. Early on, QDs were grown by self-assembly [3]. Properties, such as dot sizes or dot densities, can be altered by choosing the proper growth parameters [4]. However, this alone does not provide any control over quantum dot positions, since self-assembly is inherently a random process. With regard to quantum information applications it is essential to have an ability to define arbitrary device architectures, i.e. to control the location of each individual QD with the prospect of scalability. But not solely applications generate a desire to control QD nucleation sites. Experiments with single QDs to study their physical properties, especially coupling to cavities, require physical access to single dots, which is generally accompanied by a tedious search for the right dot.

Techniques to precisely position QDs have therefore been elaborated in the past. Top-down techniques such as electron beam lithography (EBL), local oxidation or mechanical nano-indentation have proven to be viable in order to define QD nucleation sites [5–7]. Common to those approaches is the creation of small holes on the substrate surface, which leads to selective QD nucleation at the desired locations. Pre-structuring is commonly performed *ex situ* and usually involves several process steps. Besides intended surface manipulation, contamination can occur. Therefore, great care has to be taken with regard to surface cleanliness prior to regrowth in order to inhibit unintended QD nucleation caused by defects. In addition, the optical properties are very sensitive to defects as well, so that site-selective QDs exhibit inferior optical quality compared to self-assembled ones. The main reason is attributed to a change of morphology at the hole site. The defects originate from the regrowth interface [8]. This obstacle is often circumvented by growing QD stacks consisting of a QD seed layer and a spacer layer as large as possible [9]. Reducing the dot density and controlling the occupation number of QDs per site was, however, not improved that way.

A different approach to access the aforementioned quantities makes use of the fact that QDs undergo morphological changes during annealing. At lower temperatures they tend to ripen whereas they dissolve at higher temperatures [10,11]. By choosing the right annealing conditions it should therefore be possible to control, to some extent, the final QD size as well as the QD distribution and the occupation number per site. Annealing studies on unstructured substrates have already confirmed an increase in QD size uniformity [12,13].

* Corresponding author. Tel.: +49 721 608 3893; fax: +49 721 608 4950.
E-mail address: daniel.schaadt@kit.edu (D.M. Schaadt).

0022-0248/$ - see front matter © 2010 Elsevier B.V. All rights reserved.
doi:10.1016/j.jcrysgro.2010.11.162

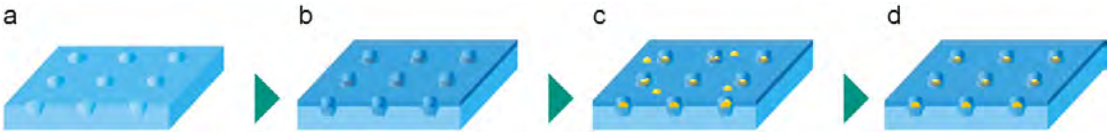

Fig. 1. Concept for improved site-selective quantum dot growth. In the first step a GaAs substrate is pre-structured by lithographic techniques to define nano-holes (a). The native oxide is removed and a thin GaAs buffer layer is grown on top of the pre-structured surface (b). This is followed by InAs QD growth (c). *In situ* annealing is then used to control the QD distribution and the occupation number of QDs per site (d).

We introduce a new concept for optimized site-selective QD growth, which is schematically shown in Fig. 1. Site-selectivity is achieved by lithographically defining nano-holes. *In situ* annealing is then used to improve the QD distribution and the occupation number of QDs per site. Therefore, in this study, we investigated the effect of *in situ* annealing on InAs QDs site-selectively grown on pre-structured GaAs substrates. In addition, the sample preparation process was optimized in order to account for unintended QD nucleation.

2. Experimental

The samples were grown by molecular beam epitaxy (MBE) in a Riber Compact 21T with the samples being continuously rotated. Epi-ready (1 0 0) GaAs wafers were used as substrates and surface-patterning was performed on top of a 90 nm GaAs epitaxial layer. Conventional electron-beam lithography was used to define 50–70 nm wide holes in a PMMA/MA (polymethyl methacrylate/methacrylate) co-polymer resist on the surface. The holes were arranged on square grids with varying lattice constants. They were etched 30 nm deep into the substrate by wet chemical etching (WCE) using H_2SO_4:H_2O_2:H_2O. The resist was removed and the samples were cleaned in a series of solvent baths before being heated up to 130 °C for 1 h in the load lock chamber of the MBE system in order to get rid of volatile surface contamination.

The surface oxide was removed *in situ* by Ga-assisted deoxidation [14]. Therefore, the samples were heated up to 480 °C and exposed to a low Ga-flux of ~1 ML/min. Every 30 s of Ga-exposure was followed by a pause of 30 s such that the converted Ga_2O more easily desorbs from the surface. A total amount of 8 ML of Ga was provided before the substrate temperature was increased to 550 °C and the samples were annealed for 2 min under As_4-atmosphere. A 16 nm GaAs buffer layer (BL) was then grown at 500 °C followed by deposition of InAs at the same temperature. The growth rates for GaAs and InAs were determined as 0.3 and 0.07 ML/s with III/V beam equivalent pressure (BEP) ratios of 1:10 and 1:100, respectively. *In situ* annealing was performed right after QD growth. The samples were kept at growth temperature for different time periods and either rapidly cooled down to room temperature by switching off the substrate heater or capped with 80 nm GaAs. The uncapped samples were characterized by atomic force microscopy (AFM) whereas the capped samples allowed for transmission electron microscopy analysis and micro-photoluminescence (μ−PL) measurements, which were performed at 20 K with a He:Ne laser using a Si charge coupled device detector. The laser spot size was about 1 μm.

3. Results and discussion

3.1. In situ annealing of site-selective QDs

Site-selective QDs were annealed and compared to as grown site-selective ones. Fig. 2 shows a set of QD samples with both containing 1.7 ML of InAs. The as grown sample shows

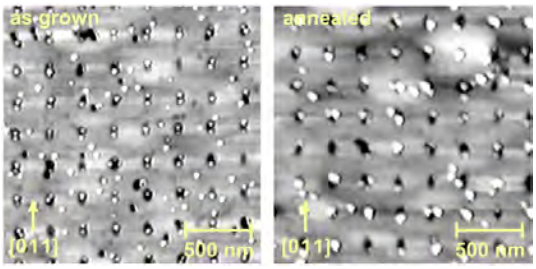

Fig. 2. Atomic force microscopy images of site-selective InAs QDs (1.7 ML) as grown (left) and annealed for 2:30 min (right). The gray scale is 18 nm in both cases.

predominant double dot nucleation per site. This fact is probably related to a change in hole morphology during GaAs BL growth [15]. QDs nucleating on interstitial sites (sites between holes) are found since the supplied amount of InAs is above the critical thickness for QD formation on pre-structured substrates.

After annealing the sample for 2:30 min, the number of interstitial QDs is reduced and, moreover, a morphological change of the site-selective QDs is observed. Original double dots merge into single dots. By facilitating In-adatom migration the annealing step causes the material to redistribute. The volume of the newly formed single dots is larger than the combined volume of the original double dots. This is related to the reduction of interstitial dots. The site-selective QDs appear to be more stable than the interstitial dots and ripen by collecting material from surrounding interstitial dots. This observation is best described by a kinetic model with the ripening process being limited by attachment and detachment of atoms on the dot surface [16].

The optical quality of annealed QDs was analyzed by μ−PL spectroscopy. The spectra shown in Fig. 3 were obtained from self-assembled (*blue*) and site-selective (*green*) QDs. Both samples contain 1.9 ML InAs and were annealed for 2:30 min. The intensity of the QD emission in the pre-structured sample is reduced compared to the self-assembled QDs and not all emission lines seem to fully emerge. As seen from two individual peaks (both show maximum intensity of each spectrum), the maximum intensities differ by a factor of 2. The linewidth of these QD emission peaks is 170 and 81 μeV (each full width at half maximum, FWHM) for the site-selective and self-assembled QDs sample, respectively.

μ−PL data on conventional self-assembled QDs show linewidths down to a few μeV [17]. However, these values stem from resonant excitation experiments at 2 K. Only limited μ−PL data of annealed self-assembled QDs is presently available [18] so that it is difficult to compare the possibly large linewidth of 81 μeV. Similarly, μ−PL data of as grown site-selective QDs has been published, with linewidths down to 460 μeV [9] or even 106 μeV [19], but these works deal with QD stacks and the measurements are related to the topmost QD layer. The best value of emission for a single as grown QD layer is reported to be about 500 μeV [8].

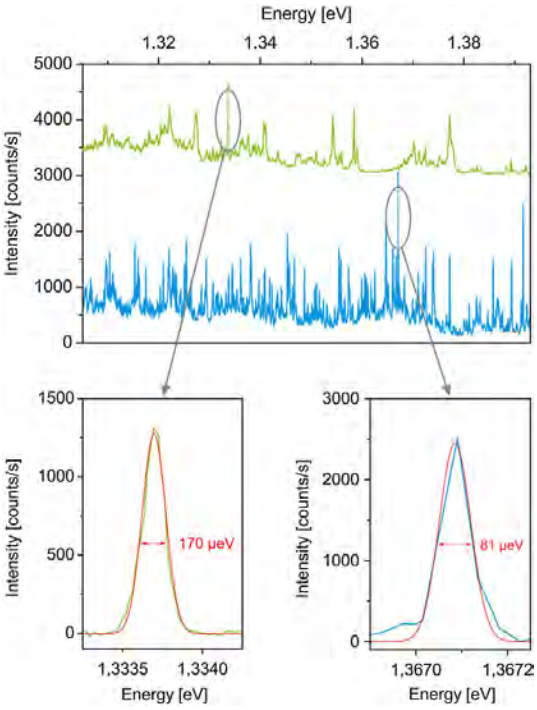

Fig. 3. Micro photoluminescence spectra of self-assembled (bottom) and site-selective (top) QDs. A total amount of 1.9 ML InAs was grown followed by 2:30 min annealing. The upper spectrum is offset by 3000 counts/s. Single emission peaks were extracted from the spectra showing linewidths of site-selective (left) and self-assembeld (right) QDs. The single peaks are background corrected data fitted with a Gaussian.

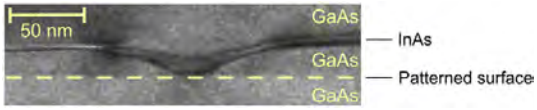

Fig. 4. Transmission electron microscopy image of an overgrown defect hole. The regrowth interface is indicated by the dashed line.

With regard to the fact that site-selective QDs in all cases exhibit inferior luminescence compared to self-assembled ones, our data is in agreement with other works. It has to be pointed out, though, that it is not possible to discriminate between emission coming from site-selective QDs and the one emerging from interstitial QDs. This obstacle will be addressed in follow-up experiments. Nevertheless, in comparison with previous data (not shown here) we see evidence that at least half of the site-selective QDs are optically active. A rough analysis of the above spectra yields 100 peaks with an average FWHM of 570 ± 270 μeV for the pre-structured sample and 170 peaks with an average FWHM of 280 ± 110 μeV for the self-assembled sample.

3.2. Sample preparation procedure: problems and optimization

Besides pre-defined holes additional defect holes are observed in the pre-structured area, as can be seen in Fig. 2. An overgrown defect hole is found in the TEM image of Fig. 4. Local contamination of the pre-structured surface hindered proper regrowth of the GaAs BL. However, InAs nucleates at this particular location allowing for a smooth overgrowth of the defect hole. Such unintended holes can act as nucleation sites and therefore interfere with the attempt to deterministically position QDs.

Two factors can account for the occurrence of such defect holes. First, incomplete removal of the native oxide could leave residual oxide compounds on the surface, which affect the proper GaAs regrowth. Second, insufficient surface cleaning after the lithography process could cause local organic contamination of the sample, which also impacts the GaAs growth. Incomplete deoxidation is rather unlikely since the defect holes are not randomly distributed. Some local areas are found with a high defect density whereas other areas seem very clean. In addition, by controlling the surface evolution during deoxidation by means of reflection high energy electron diffraction (RHEED), it is made sure that enough Ga is provided to completely remove the native oxide. Focus was therefore laid on analyzing and optimizing the cleaning procedure prior to regrowth.

Cleaning samples after EBL comprises several steps. After removing the resist the samples were cleaned with different solvents (trichlorethylene, acetone, isopropyl alcohol, methanol) in a heated ultrasonic bath. Finally, the samples were rinsed in bi-distilled water. Critical steps of the cleaning procedure are depicted in Fig. 5. The sample in Fig. 5(a) was cleaned in a series of solvent baths without ultrasonic aid. A lot of contamination is observed from the AFM image (large particles appearing white). The cleaning is improved by performing the whole procedure in an ultrasonic

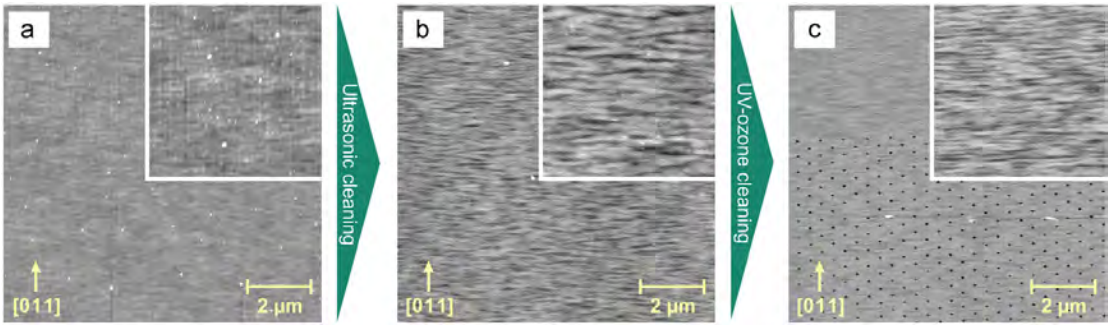

Fig. 5. Atomic force microscopy images of samples at different stages of the cleaning procedure: after cleaning with solvents (a), using a heated ultrasonic bath (b) and after UV-ozone cleaning (c). The pre-structured area is visible in (c). All samples were prepared in the same way. The insets are 3μm × 3μm. The gray scale is for the full size 20, 27, 58 nm and for the inset 13, 6, 4 nm in (a), (b), (c), respectively.

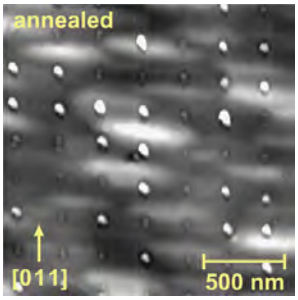

Fig. 6. Atomic force microscopy image of site-selective QDs. A total amount of 2.6 ML of InAs was provided followed by a 7:30 min annealing. The gray scale is 30 nm.

bath. However, small amounts of organic contamination remain on the surface, see Fig. 5(b). In order to also remove these, a UV-ozone cleaning is introduced [20]. The UV light creating and destroying ozone at the same time constantly provides atomic oxygen that reacts with organic molecules on the sample surface. Simpler, volatile compounds are formed that readily desorb. The effect is displayed in Fig. 5(c) where essentially all contamination has disappeared.

The success of the optimized sample preparation is confirmed by Fig. 6, which depicts a sample with site-selective QDs that were annealed for 7:30 min. A total amount of 2.6 ML InAs were grown prior to annealing. No defect holes are observed in the pre-structured area. In addition, no interstitial dots are found, which is ascribed to the elongated annealing time. The same morphological transition as described in the previous section is observed once more.

4. Conclusion

In conclusion, we have introduced a new concept for optimized growth of site-selective quantum dots. *In situ* annealing was used to control the QD distribution and the occupation number of QDs per site. A morphological transition was observed with originally two dots merging into a single dot. In photoluminescence measurements we found linewidths of annealed site-selective QDs and self-assembled QDs of 170 and 81 μeV. The cleaning process prior to regrowth was optimized by making use of a UV-ozone process. As a result, the samples are essentially free of organic contamination.

Acknowledgments

The Karlsruhe researchers acknowledge financial support from the Deutsche Forschungsgemeinschaft (DFG) and the State of Baden-Württemberg through the DFG-Center for Functional Nanostructures (CFN) within subproject A2.6. The Tucson group would like to acknowledge support (EEC-0812072) from the National Science Foundation (NSF) through the Engineering Research Center for Integrated Access Networks (CIAN) and Atomic Molecular and Optical Physics (AMOP) and Electronics, Photonics and Device Technologies (EPDT), as well as AFOSR, and Arizona Technology & Research Initiative Funding (TRIF).

References

[1] P. Michler, A. Kiraz, C. Becher, W.V. Schoenfeld, P.M. Petroff, L. Zhang, E. Hu, A. Imamoğlu, A quantum dot single-photon turnstile device, Science 290 (2000) 2282–2285.
[2] N. Akopian, N.H. Lindner, E. Poem, Y. Berlatzky, J. Avron, D. Gershoni, B.D. Gérardot, P.M. Petroff, Entangled photon pairs from semiconductor quantum dots, Phys. Rev. Lett. 96 (2006) 130501–130504.
[3] D. Leonard, K. Pond, P.M. Petroff, Critical layer thickness for self-assembled InAs islands on GaAs, Phys. Rev. B 50 (1994) 11687–11692.
[4] N.N. Ledentsov, V.A. Shchukin, D. Bimberg, V.M. Ustinov, N.A. Cherkashin, Yu.G. Musikhin, B.V. Volovik, G.E. Cirlin, Zh.I. Alferov, Reversibility of the island shape, volume and density in Stranski-Krastanow growth, Semicond. Sci. Technol. 16 (2001) 502–506.
[5] S. Jeppesen, S. Miller, S. Hessman, B. Kowalski, I. Maximov, L. Samuelson, Assembling strained InAs islands on patterned GaAs substrates with chemical beam epitaxy, Appl. Phys. Lett. 68 (1996) 2228–2230.
[6] O.G. Schmidt, S. Kiravittaya, Y. Nakamura, H. Heidemeyer, R. Songmuang, C. Müller, N.Y. Jin-Phillipp, K. Eberl, H. Wawra, S. Christiansen, H. Gräbeldinger, H. Schweizer, Self-assembled semiconductor nanostructures: climbing up the ladder of order, Surf. Sci. 514 (2002) 10–18.
[7] P. Atkinson, M.B. Ward, S.P. Bremner, D. Anderson, T. Farrow, G.A.C. Jones, A.J. Shields, D.A. Ritchie, Site control of InAs quantum dot nucleation by ex situ electron-beam lithographic patterning of GaAs substrates, Physica E 32 (2006) 21–24.
[8] P. Atkinson, O.G. Schmidt, S.P. Bremner, D.A. Ritchie, Formation and ordering of epitaxial quantum dots, C. R. Phys. 9 (2008) 788–803.
[9] T.J. Pfau, A. Gushterov, J.P. Reithmaier, I. Cestier, G. Eisenstein, E. Linder, D. Gershoni, Site-controlled InAs quantum dots grown on a 55 nm thick GaAs buffer layer, Appl. Phys. Lett. 95 (2009) 243106–243108.
[10] H. Lee, R.R. Lowe-Webb, W. Yang, P.C. Sercel, Formation of InAs/GaAs quantum dots by molecular beam epitaxy: reversibility of the islanding transition, Appl. Phys. Lett. 71 (1997) 2325–2327.
[11] C. Heyn, Stability of InAs quantum dots, Phys. Rev. B 66 (2002) 075307–075310.
[12] D.M. Schaadt, S. Krauss, R. Koch, K.H. Ploog, Stress evolution during growth of bilayer self-assembled InAs/GaAs quantum dots, Appl. Phys. A 83 (2006) 267–269.
[13] D.Z. Hu, A. Trampert, D.M. Schaadt, Morphology and stress evolution of InAs QD grown and annealed in-situ at high temperature, J. Cryst. Growth 312 (2010) 447–451.
[14] P. Atkinson, S. Kiravittaya, M. Benyoucef, A. Rastelli, O.G. Schmidt, Site-controlled growth and luminescence of InAs quantum dots using *in situ* Ga-assisted deoxidation of patterned substrates, Appl. Phys. Lett. 93 (2008) 101908–101910.
[15] S. Kiravittaya, H. Heidemeyer, O.G. Schmidt, In(Ga)As quantum dot crystals on patterned GaAs (0 0 1) substrates, in: O.G. Schmidt (Ed.), Lateral Alignment of Epitaxial Quantum Dots, Springer, Berlin, 2007, pp. 489–511.
[16] D.Z. Hu, D.M. Schaadt, K.H. Ploog, Stress development during annealing of self-assembled InAs/GaAs quantum dots measured in situ with a cantilever beam setup, J. Cryst. Growth 293 (2006) 546–549.
[17] M. Bayer, A. Forchel, Temperature dependence of the exciton homogeneous linewidth in $In_{0.60}Ga_{0.40}As$/GaAs self-assembled quantum dots, Phys. Rev. B 65 (2002) 041308.
[18] D.Z. Hu, Stress evolution during growth of InAs on GaAs measured by an in-situ cantilever beam setup, Dissertation, Humboldt-Universität zu Berlin 〈http://nbn-resolving.de/urn:nbn:de:kobv:11-10077303〉, 2007.
[19] C. Schneider, A. Huggenberger, T.S. Sünner, T. Heindel, M. Strauß, S. Göpfert, P. Weinmann, S. Reitzenstein, L. Worschech, M. Kamp, S. Höfling, A. Forchel, Single site-controlled In(Ga)As/GaAs quantum dots: growth, properties and device integration, Nanotechnology 20 (2009) 434012.
[20] S.I. Ingrey, Surface Processing of III–V Semiconductors, in: P.H. Holloway, G.E. McGuire (Eds.), Handbook of Compound Semiconductors, Noyes Publications, Park Ridge, NJ, 1995, pp. 251–284.

Appendix E

Effect of atomic layer deposition on the quality factor of silicon nanobeam cavities

M. Gehl, R. Gibson, J. Hendrickson, A. Homyk, A. Säynätjoki, T. Alasaarela, L. Karvonen, A. Tervonen, S. Honkanen, S. Zandbergen, B. C. Richards, J. D. Olitzky, A. Scherer, G. Khitrova, H. M. Gibbs, J.-Y. Kim, Y.-H. Lee

Journal of the Optical Society of America B, Vol. 29, No. 2, pp. A55-A59 (February, 2012)

Effect of atomic layer deposition on the quality factor of silicon nanobeam cavities

Michael Gehl,[1,*] Ricky Gibson,[1] Joshua Hendrickson,[2] Andrew Homyk,[3] Antti Säynätjoki,[4] Tapani Alasaarela,[4] Lasse Karvonen,[4] Ari Tervonen,[4] Seppo Honkanen,[4] Sander Zandbergen,[1] Benjamin C. Richards,[5] J. D. Olitzky,[1] Axel Scherer,[3] Galina Khitrova,[1] Hyatt M. Gibbs,[1] Ju-Young Kim,[6] and Yong-Hee Lee[6]

[1]*College of Optical Sciences, University of Arizona, 1630 East University Boulevard, Tucson, Arizona 85721, USA*
[2]*Air Force Research Laboratory, Sensors Directorate, 2241 Avionics Circle, Building 600, Wright Patterson Air Force Base, Ohio 45433, USA*
[3]*Electrical Engineering and Kavli Nanoscience Institute, California Institute of Technology, MC 200-36, 1200 East California Boulevard, Pasadena, California 91125, USA*
[4]*Department of Micro- and Nanosciences, Aalto University School of Electrical Engineering, P.O. Box 13500, 00076 Aalto, Finland*
[5]*Advanced Concepts Team, Emcore Corporation, 10420 Research Road, Albuquerque, New Mexico 87123, USA*
[6]*Department of Physics, Korea Advanced Institute of Science and Technology, Daejeon 305-701, Korea*
**Corresponding author: mgehl@optics.arizona.edu*

Received October 4, 2011; revised December 12, 2011; accepted December 12, 2011; posted December 12, 2011 (Doc. ID 155915); published January 25, 2012

In this work we study the effect of thin-film deposition on the quality factor (Q) of silicon nanobeam cavities. We observe an average increase in the Q of $38 \pm 31\%$ in one sample and investigate the dependence of this increase on the initial nanobeam hole sizes. We note that this process can be used to modify cavities that have larger than optimal hole sizes following fabrication. Additionally, the technique allows the tuning of the cavity mode wavelength and the incorporation of new materials, without significantly degrading Q.

OCIS codes: 350.4238, 310.1860, 310.6860.

1. MOTIVATION

Photonic crystal (PC) cavities provide exciting platforms for photonics applications in addition to fundamental cavity quantum electrodynamics (cQED) experiments. The ability to fabricate cavities with small mode volumes (V) and large Qs leads to large enhancements in light–matter interactions. By placing active emitters such as quantum dots (QDs) into the cavity, it is easy to observe Purcell enhancement of spontaneous emission with only modest Qs. Increasing the Q further leads to the quantum regime of strong coupling, in which energy is able to coherently transfer between the emitter and cavity multiple times before decaying. This regime leads to exciting new physics, such as the Jaynes–Cummings ladder, deterministic single-photon sources, and photon blockades [1–3].

In addition to a high Q and low V, it is important that the cavity and emitter be near resonance with each other. Previous work has shown the ability to reversibly tune cavity resonances by 5 nm using the condensation of gases at low temperatures [4]. Additionally, tuning of 2D photonic crystal systems has been shown using atomic layer deposition (ALD) of hafnium oxide [5] and titanium oxide [6] and plasma-enhanced chemical vapor deposition of silicon nitride [7]. In this work, we observe a shift in cavity resonance of 20 to 29 nm, with a high tuning precision as a result of the multiple-cycle deposition process.

Finally, it is important that one can incorporate an active medium with the cavity. While this can be achieved with QDs and quantum wells in III–V systems, it presents more of a challenge for silicon photonics. In this work, we show the ability to deposit new material on top of a silicon PC cavity with a minimal effect on the Q. This opens up the possibility of incorporating active materials through similar methods. For example, one can dope Al_2O_3 with layers of erbium during the deposition process [8].

2. NANOBEAM CAVITIES

One PC cavity geometry that is becoming popular is the 1D nanobeam, shown in Fig. 1. This design consists of a strip waveguide with an array of etched holes. The holes begin with uniform radius and spacing, creating a Bragg mirror region. The hole radius and spacing are then tapered down to a cavity region where the mode is confined, before tapering back up to another mirror region. The holes confine the light along one dimension, while it is confined by index guiding along the other two. The substrate can be etched from underneath the cavity, leaving it suspended, or in the case of this work, the cavity can remain on the substrate for increased durability. Simulations of unsuspended cavities predict Qs as high as 366,000 with a mode volume of $0.552(\lambda/n)^3$. Experimentally, unsuspended silicon nanobeam cavities have already been measured with Qs of 360,000 [9].

In this work, nanobeams are fabricated on silicon-on-insulator wafers, consisting of a 220 nm silicon layer on top of a 2 μm SiO_2 layer. The structure is defined using electron beam lithography and formed using inductively coupled

Fig. 1. (Color online) Schematic of the 1D nanobeam cavity with overlay of normalized electric field energy density.

plasma etching. Each nanobeam is characterized by a lattice constant "a," which is the distance between the center of the holes in the mirror region. The value of a varies from 390 to 455 nm in 5 nm steps, shifting the cavity mode through the range of our measurement ability. In the taper region, the lattice constant varies from $0.98a$ to $0.86a$, while in the cavity region, the lattice constant is $0.84a$. The nominal hole radius is 0.3 times the local lattice constant.

3. CHARACTERIZATION BY MEASUREMENT OF THE CAVITY QUALITY FACTOR *Q*

In order to characterize the Q of silicon nanobeam cavities, we use the tapered microfiber probe technique [10,11]. In this technique, an optical fiber is heated and stretched, such that it adiabatically tapers to a region with a diameter on the order of 1 μm. This region of the fiber is then carefully positioned across the nanobeam cavity. A tunable narrowband laser source is coupled into one end of the fiber, and the transmitted power is detected at the other end. As the laser source is tuned into resonance with the cavity, some of the power is coupled into the cavity mode, resulting in a measurable dip in transmission through the fiber.

As a result of the tapered microfiber probe, the cavity experiences an additional amount of loss. This causes an increase in the measured resonance linewidth and thus a decrease in the measured Q compared to the intrinsic Q of the cavity. This effect was studied in [10], which found that by positioning the probe near the edge of the nanobeam, coupling to the cavity is minimized, leading to a measured Q closer to the intrinsic Q. For this study, all Qs are measured at the edge of the nanobeam cavity. Because of the positioning uncertainty of the probe, which leads to slight changes in the coupling and hence the measured Q, five measurements are taken of each cavity; the maximum value is used for all comparisons.

To determine the intrinsic Q of a cavity, we use the crossed polarizer resonant scattering technique [10,12]. This is a free space method in which a tunable laser source is focused onto the cavity with a microscope objective. The incident light is polarized at 45° with respect to the polarization of the cavity mode. The reflected light is passed through a polarizer at 90° relative to the incident light. Light that simply reflects from the substrate will be blocked by the crossed polarizer. Light that couples into the cavity will scatter out with the polarization of the cavity mode, a portion of which will be able to pass through the final polarizer and be detected. Because of the increased difficulty and low signal-to-noise ratio of this measurement, this technique is used only to determine the intrinsic Q of the best cavities.

4. ATOMIC LAYER DEPOSITION

Atomic layer deposition is a thin-film deposition process that works through the sequential application of two or more gas phase chemicals. The growth takes place as a chemical reaction at the sample surfaces. The reaction is self-limiting, allowing accurate control of film thickness simply by counting the number of cycles.

Because of the nature of this deposition technique, the resulting film is conformal and grows along the surface normal [13]. This effect has already been utilized to grow microlens arrays [14] and planarized optical gratings [15] and to tune photonic crystal waveguides [7,16]. The conformal film also reduces surface roughness, and ALD-grown Al_2O_3 and TiO_2 films have been found to significantly reduce propagation losses in silicon strip and slot waveguides [13,17]. Because the geometry of the silicon nanobeam cavity is a modified silicon strip waveguide, we believe that this process could lead to decreased losses and higher Qs in these structures.

For this work, we investigated the thin-film growth of both TiO_2 and Al_2O_3 on nanobeam cavities by ALD. TiO_2 is deposited at 120 °C using a process with titanium tetrachloride ($TiCl_4$) and water as precursors [18]. Al_2O_3 is deposited at 200 °C using a process with trimethylaluminum ($Al_2(CH_3)_6$) and water as precursors [19]. Figure 2 shows scanning electron micrograph (SEM) images of a cavity before and after the deposition of 20 nm of Al_2O_3, showing a clear reduction in hole size due to the thin film.

5. EXPERIMENTAL RESULTS

For initial tests, two nanobeam samples were fabricated using the same design parameters. They were first characterized using the tapered microfiber technique. While imaging the

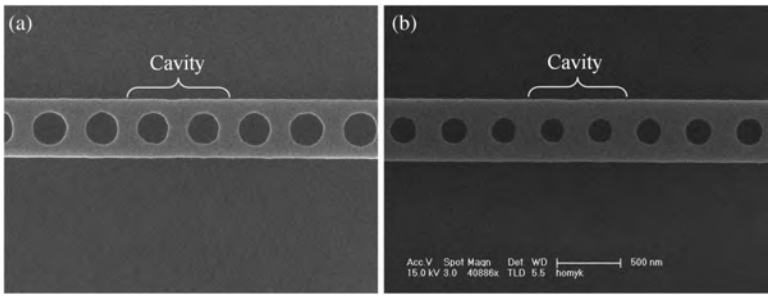

Fig. 2. SEM images of the cavity region of a silicon nanobeam (a) before and (b) after deposition of 20 nm Al_2O_3 by ALD.

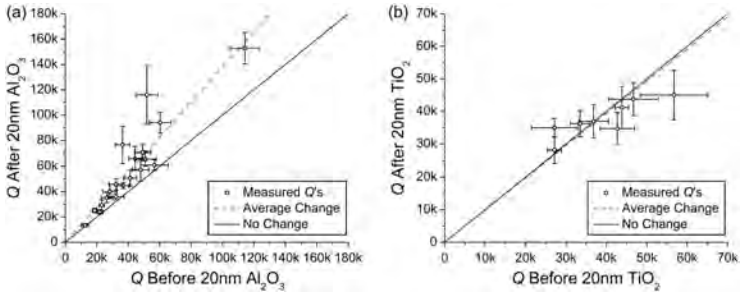

Fig. 3. (Color online) Q of several cavities after ALD plotted against the Q measured before ALD, for 20 nm of (a) Al_2O_3 and (b) TiO_2. The solid line has a slope of 1 and represents no change in the Q, while the dotted line represents the average change of 38% for Al_2O_3 and −1.3% for TiO_2.

cavities, it was noticed that there was residual mask material remaining from fabrication. This material was removed using a 10 min O_2 plasma etch. The cavities were recharacterized, and it was noted that the cavity wavelength decreased by 6.5 nm on average, but there was no significant change in cavity Q. One sample was then coated with 20 nm of TiO_2 (index 2.27 at $\lambda = 1.55$ μm), while the other was coated with 20 nm of Al_2O_3 (index 1.62 at $\lambda = 1.55$ μm). The samples were characterized again, following the same procedure. The TiO_2 (Al_2O_3) coated sample showed a shift in cavity mode of $59.2 \pm 0.7(30.3 \pm 0.8)$ nm on average. The results of the Q measurements are plotted in Fig. 3. While one TiO_2 coated cavity showed an increase in Q of 29%, the average change in Q over all cavities was $-1.3 \pm 16\%$. Every Al_2O_3 coated cavity showed an increase in Q, with an average increase of $38 \pm 31\%$ and a maximum increase of 124%. The large standard deviation for this sample mostly results from 2 of the 19 cavities, which showed an increase of more than 100%. Figure 4 shows a measurement of a cavity from the Al_2O_3-coated sample before and after deposition. This measurement was performed using the crossed polarizer resonant scattering technique, so the measured Q is that of the intrinsic Q. This shows the cavity Q to have increased from 107,000 to 212,000.

While the deposition of 20 nm of Al_2O_2 on that particular sample resulted in a clear increase in the cavity Q, from these initial tests it is not clear what factors contributed to this increase. The fact that the sample coated with TiO_2 did not show the same increases suggests that the effect is not exclusively due to a decrease in surface roughness. Finite-difference time-domain (FDTD) simulations of the silicon nanobeam Q [Fig. 5(a)] indicate that the Q is highly dependent on the hole radius, with a peak Q near a radius of 0.3 times the lattice constant. To account for the decrease in hole radius as a result of the ALD coating, a third sample was fabricated with an added offset to the hole radius. For each lattice constant, 13 cavities were defined with offsets ranging from −30 to +30 nm in 5 nm steps. Four arrays of these cavities were fabricated with varying electron beam dosage, but only two arrays provided useful cavities.

This sample was characterized, coated with 20 nm of Al_2O_2, and then recharacterized. Fifty-three of the 60 cavities that were characterized on this third sample showed increases in the Q, with the average increase being $20 \pm 19\%$. Figure 5(b) shows a plot of the measured Q prior to ALD coating as a function of hole radius offset. There is a trend toward higher Qs for cavities with smaller holes. Unlike the simulation, there is not a clear peak in the Q. This suggests that our range of hole sizes did not cover the designed range. Looking at the percent increase in the Q as a function of the hole radius offset (Fig. 6), there is also a clear trend toward a greater increase for cavities with larger holes. Following ALD, these cavities have hole sizes closer to those of the cavities that showed the highest Qs prior to ALD. This is consistent with the idea that the increase in Q is due to the shift of hole size closer to the optimal (highest Q) design.

Figure 7 shows a plot of the shift in the cavity mode wavelength as a result of the deposition of 20 nm of Al_2O_3, along with FDTD simulation results. While the wavelength shift showed very little dependence on the lattice constant, it showed a strong dependence on the initial hole radius offset.

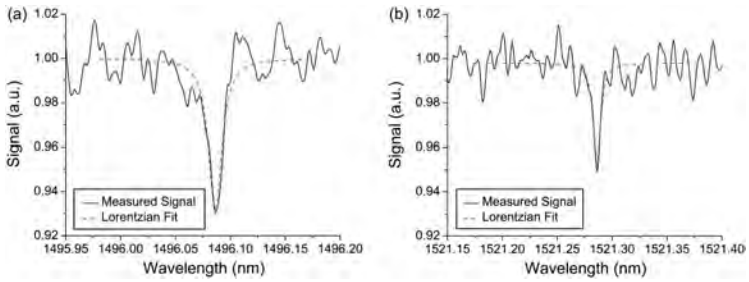

Fig. 4. (Color online) Crossed polarizer resonant scattering measurement of a cavity (a) before and (b) after being coated with 20 nm of Al_2O_3, yielding a measured Q of 107,000 before and 212,000 after. The before data were collected prior to the O_2 plasma etch, which removed the mask residue and shifted the cavity peak to shorter wavelength by 6.5 nm.

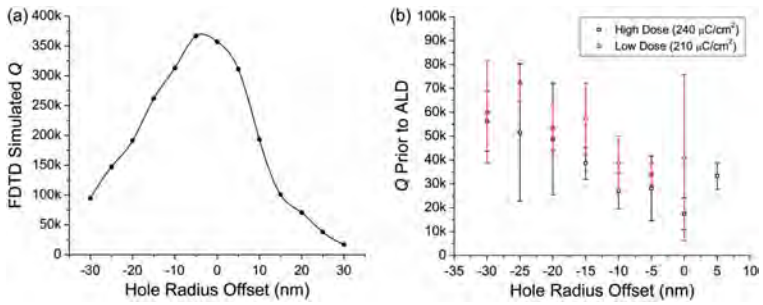

Fig. 5. (Color online) (a) FDTD simulation of the Q prior to ALD coating, showing the expected peak around 0 nm offset. The 0 nm offset corresponds to a hole radius of 0.3 times the lattice constant. (b) Plot of the average measured Q of several cavities prior to ALD coating versus the hole radius offset, showing a trend of higher Q for cavities with smaller holes (more negative offset). Dose refers to the dosage used during electron beam lithography.

The shift also showed some dependence on the dosage used during electron beam lithography. This is likely due to the dependence of the hole size and beam width on electron beam dose. The higher dose array, which should have larger holes due to the increased exposure of the mask, showed wavelength shifts in the range of 21.6 ± 0.2 nm for the smallest holes to 28.0 ± 0.1 nm for the largest holes. The lower dose array showed wavelength shifts in the range of 20.2 ± 0.2 nm for the smallest holes to 27.1 ± 0.4 nm for the largest. The FDTD simulations predict a similar range of wavelength shift. The tuning precision is very high because it is determined by the growth rate of the thin film, which can be very slow. For the ALD technique used in this work, the growth rate was around 0.1 nm/cycle, with a cycle time of 3.45 s. This results in a wavelength shift on the order of 0.1–0.15 nm/cycle.

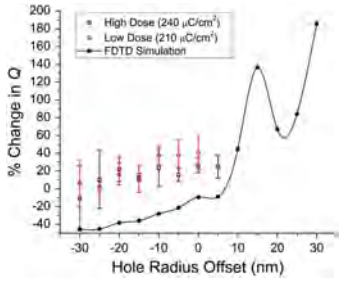

Fig. 6. (Color online) Plot of the average percent change in the Q of the cavities from Fig. 4 versus the initial hole radius offset, showing a trend of greater increase for cavities that began with larger holes (more positive offset). The FDTD results are plotted for comparison.

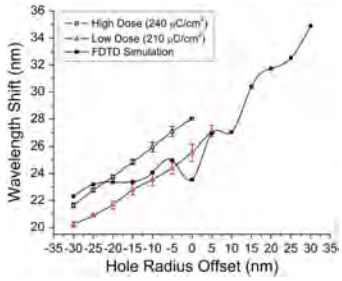

Fig. 7. (Color online) Plot of the average shift in wavelength of the cavity mode following ALD versus the hole radius offset, along with the FDTD simulation results.

In order to investigate the effect of the Al_2O_3 coating on the mode volume, we use numerical methods. FDTD simulations reveal a nearly linear relationship between the mode volume and hole radius offset. The mode volume increases from $0.410(\lambda/n)^3$ for a +30 nm offset, to $0.658(\lambda/n)^3$ for a –30 nm offset. At the same time, the increase in mode volume as a result of depositing 20 nm of Al_2O_3 shows little dependence on the hole radius offset, fluctuating in the range of a 2.06% to 6.45% increase.

6. CONCLUSIONS

We have shown that ALD can be a valuable tool for tuning the resonant wavelength and Q of 1D silicon nanobeam cavities postfabrication. The low index and low deposition rate of Al_2O_3 allows for very precise control of the wavelength shift. The initial size of the cavity holes also plays an important role in the resonance shift. Cavities with smaller holes to begin with will have modes that are more confined to the silicon and therefore will see less of an effect from the additional dielectric material.

Initial results show that a 20 nm coating of Al_2O_3 can increase the Q of 1D silicon nanobeam cavities by $38 \pm 31\%$. While the exact nature of this change in the Q is not fully understood, both simulation and experiment show that the Q is significantly affected by the size of the cavity holes. Therefore, it is likely that the changing hole size resulting from the Al_2O_3 deposition is responsible for much of the change in the Q observed in this work. There still remains much to be done to determine the contribution of other effects to the change in the Q. The conformal nature of the ALD film will lead to decreased surface roughness and decreased scattering losses at the Al_2O_3–air interface; however, the large index mismatch of Al_2O_3 and silicon means that scattering at this interface will still be significant. Additionally, the thin film could be causing surface passivation, leading to decreased absorption by surface states. Finally, the film may be affecting the mode profile, pulling the field away from the oxide layer and decreasing losses into the substrate. Repeating these experiments with

various materials and film thicknesses will reveal more detail on these separate effects.

In summary, the ability to deposit Al_2O_3 onto silicon nanobeams without significantly degrading the Q or increasing V is important for the field of silicon photonics and cQED. In addition to being able to tune the cavity resonance, the ability to incorporate new materials, such as erbium, will allow the fabrication of active devices from silicon PC cavities.

ACKNOWLEDGMENTS

M. Gehl acknowledges support by the Department of Defense (DoD) through the National Defense Science & Engineering Graduate Fellowship (NDSEG) program. S. Zandbergen acknowledges partial support from Arizona Technology & Research Initiative Funding (TRIF). J. Hendrickson acknowledges support from the Air Force Office of Scientific Research (AFOSR)—LRIR 10RY04COR (Gernot Pomrenke, program manager). A. Homyk appreciates the generous support of the ARCS Foundation. A. Säynätjoki was supported by Academy of Finland grant 134087 and a travel grant by the Finnish Foundation for Technology Promotion. The Caltech and UofA groups thank NSF ERC CIAN (EEC-0812072) for support. The UofA group acknowledges support from the AFOSR (FA9550-10-1-0003) and NSF EPMD (ECCS-1101341).

REFERENCES

1. P. R. Berman, *Cavity Quantum Electrodynamics* (Academic, 1994).
2. K. Vahala, *Optical Microcavities* (World Scientific, 2004).
3. G. Khitrova, H. M. Gibbs, M. Kira, S. W. Koch, and A. Scherer, "Vacuum Rabi splitting in semiconductors," Nat. Phys. **2**, 81–90 (2006).
4. S. Moser, J. Hendrickson, B. C. Richards, J. Sweet, G. Khitrova, H. M. Gibbs, T. Yoshie, A. Scherer, O. B. Shchekin, and D. G. Deppe, "Scanning a photonic crystal slab nanocavity by condensation of xenon," Appl. Phys. Lett. **87**, 052101 (2005).
5. X. Yang, C. J. Chen, C. A. Husko, and C. W. Wong, "Digital resonance tuning of high-Q/V_m silicon photonic crystal nanocavities by atomic layer deposition," Appl. Phys. Lett. **91**, 161114 (2007).
6. S. Schartner, S. Kalchmair, A. M. Andrews, P. Klang, W. Schrenk, and G. Strasser, "Post-fabrication fine-tuning of photonic crystal quantum well infrared photodetectors," Appl. Phys. Lett. **94**, 231117 (2009).
7. E. Graugnard, D. P. Gaillot, S. N. Dunham, C. W. Neff, T. Yamashita, and C. J. Summers, "Photonic band tuning in two-dimensional photonic crystal slab waveguides by atomic layer deposition," Appl. Phys. Lett. **89**, 181108 (2006).
8. K. Solehmainen, M. Kapulainen, P. Heimala, and K. Polamo, "Erbium-doped waveguides fabricated with atomic layer deposition method," IEEE Photon. Technol. Lett. **16**, 194–196 (2004).
9. E. Kuramochi, H. Taniyama, T. Tanabe, K. Kawasaki, Y.-G. Roh, and M. Notomi, "Ultrahigh-Q one-dimensional photonic crystal nanocavities with modulated mode-gap barriers on SiO_2 claddings and on air claddings," Opt. Express **18**, 15859–15869 (2010).
10. B. C. Richards, J. Hendrickson, J. D. Olitzky, R. Gibson, M. Gehl, K. Kieu, U. K. Khankhoje, A. Homyk, A. Scherer, J.-Y. Kim, Y.-H. Lee, G. Khitrova, and H. M. Gibbs, "Characterization of 1D photonic crystal nanobeam cavities using curved microfiber," Opt. Express **18**, 20558–20564 (2010).
11. I.-K. Hwang, S.-K. Kim, J.-K. Yang, S.-H. Kim, S.-H. Lee, and Y.-H. Lee, "Curved-microfiber photon coupling for photonic crystal light emitter," Appl. Phys. Lett. **87**, 131107 (2005).
12. M. W. McCutcheon, G. W. Rieger, I. W. Cheung, J. F. Young, D. Dalacu, S. Frédérick, P. J. Poole, G. C. Aers, and R. L. Williams, "Resonant scattering and second-harmonic spectroscopy of planar photonic crystal microcavities," Appl. Phys. Lett. **87**, 221110 (2005).
13. T. Alasaarela, D. Korn, L. Alloatti, A. Säynätjoki, A. Tervonen, R. Palmer, J. Leuthold, W. Freude, and S. Honkanen, "Reduced propagation loss in silicon strip and slot waveguides coated by atomic layer deposition," Opt. Express **19**, 11529–11538 (2011).
14. J. J. Wang, A. Nikolov, and Q. Wu, "Nano- and microlens arrays grown using atomic-layer deposition," IEEE Photon. Technol. Lett. **18**, 2650–2652 (2006).
15. J. J. Wang, X. Deng, R. Varghese, and A. Nikolov, "Filling high aspect-ratio nano-structures by atomic layer deposition and its applications in nano-optic devices and integrations," J. Vac. Sci. **23**, 3209–3213 (2005).
16. D. Gaillot, E. Graugnard, J. Blair, and C. Summers, "Dispersion control in two-dimensional superlattice photonic crystal slab waveguides by atomic layer deposition," Appl. Phys. Lett. **91**, 181123 (2007).
17. A. Säynätjoki, L. Karvonen, T. Alasaarela, X. Tu, T. Y. Liow, M. Hiltunen, A. Tervonen, G. Q. Lo, and S. Honkanen, "Low-loss silicon slot waveguides and couplers fabricated with optical lithography and atomic layer deposition," Opt. Express **19**, 26275–26282 (2011).
18. T. Alasaarela, T. Saastamoinen, J. Hiltunen, A. Säynätjoki, A. Tervonen, P. Stenberg, M. Kuittinen, and S. Honkanen, "Atomic layer deposited titanium dioxide and its application in resonant waveguide grating," Appl. Opt. **49**, 4321–4325 (2010).
19. R. L. Puurunen, "Surface chemistry of atomic layer deposition: A case study for the trimethylaluminum/water process," J. Appl. Phys. **97**, 121301 (2005).

Appendix F

Spectroscopic studies of resonant coupling of silver optical antenna arrays to a near-surface quantum well

M. Gehl, S. Zandbergen, R. Gibson, M. Béchu, N. Nader, J. Hendrickson, J. Sears, P. Keiffer, M. Wegener, G. Khitrova

Journal of Optics, Vol. 16, No. 11, pp. 114016 (November, 2014)

IOP Publishing Journal of Optics
J. Opt. **16** (2014) 114016 (11pp) doi:10.1088/2040-8978/16/11/114016

Invited Article

Spectroscopic studies of resonant coupling of silver optical antenna arrays to a near-surface quantum well

Michael Gehl[1], Sander Zandbergen[1], Ricky Gibson[1], Muriel Béchu[2], Nima Nader[1,3,4], Joshua Hendrickson[3], Jasmine Sears[1], Patrick Keiffer[1], Martin Wegener[2] and Galina Khitrova[1]

[1] College of Optical Sciences, University of Arizona, Tucson, AZ-85721 USA
[2] Institut für Angewandte Physik, Institut für Nanotechnologie, Karlsruhe Institute of Technology (KIT), D-76128 Karlsruhe, Germany
[3] Air Force Research Laboratory, Sensors Directorate, Wright Patterson AFB, OH-45433, USA
[4] Solid State Scientific Corporation, 12 Simon St. Nashua, NH-03060, USA

E-mail: mgehl@optics.arizona.edu

Received 6 June 2014, revised 19 August 2014
Accepted for publication 20 August 2014
Published 3 November 2014

Abstract

The coupling of radiation emitted on semiconductor inter-band transitions to resonant optical-antenna arrays allows for enhanced light–matter interaction via the Purcell effect. Semiconductor optical gain also potentially allows for loss reduction in metamaterials. Here we extend our previous work on optically pumped individual near-surface InGaAs quantum wells coupled to silver split-ring-resonator arrays to wire and square-antenna arrays. By comparing the transient pump-probe experimental results with the predictions of a simple model, we find that the effective coupling is strongest for the split rings, even though the split rings have the weakest dipole moment. The effect of the latter must thus be overcompensated by a smaller effective mode volume of the split rings. Furthermore, we also present a systematic variation of the pump-pulse energy, which was fixed in our previous experiments.

Keywords: metamaterials, semiconductor/metal coupling, transient pump-probe

(Some figures may appear in colour only in the online journal)

1. Introduction

Optical antennas, similar to radiowave antennas, allow for the coupling of freely propagating electro-magnetic waves to sub-wavelength localized modes. While radiowave antennas have been around since the late 1800's, the first mention of something resembling an optical antenna didn't appear until 1928, in letters between Edward Synge and Albert Einstein [1]. Optical antennas didn't become experimentally feasible until the mid 1980's [2]. Over the past decade research based on optical antennas has grown quickly, with applications covering high resolution microscopy, single-photon sources, photo-voltaics, optical switching, metamaterials and more [3–10]. This research has also led to many interesting theoretical questions on the nature of electro-magnetic fields confined by metallic nano-structures [11–13].

In the field of meta-materials one is interested in arrays of individual antennas, arranged on a sub-wavelength scale in order to produce macroscopic properties different than those of the bulk materials from which they are fabricated. Progress in this field has reached the point where individual metal nano-structures resonate at optical frequencies [3]. The resonant coupling of arrays of metallic nano-structures to a semiconductor quantum well represents a very curious problem involving the fundamental physics of a rather complex metal/semiconductor hybrid system. In the past the coupling

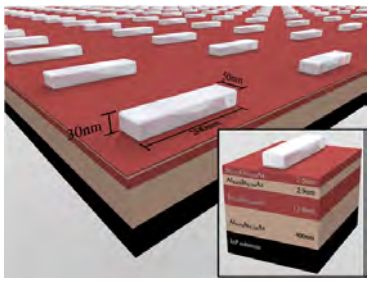

Figure 1. Diagram of an array of silver wire antennas fabricated on top of a near-surface quantum well. (Inset) Close up of the quantum well structure.

of arrays of split-ring shaped antennas to a semiconductor quantum well was demonstrated [14]. If one wants to shift to shorter wavelength, fabrication is less of a problem with simpler shapes such as wires and squares. It also is already known that a larger dipole moment (cross section) is achieved from individual wire and square shaped antennas, as compared to the split-ring shape [15]. It is therefore natural to study arrays of wire and square antennas coupled to a quantum well in to order see if this would lead to a larger coupling effect. Clearly interactions between individual antennas within the array can severely alter the behavior of the array from that of the individual antenna itself [16].

In this work we study the properties of silver optical antennas fabricated in arrays displaced by approximately 5.4 nm from a semiconductor quantum well, as pictured in figure 1 for an array of wire shaped antennas. We are concerned primarily with the effective coupling of the antenna array to the quantum well and use a simple toy-model [17] based on near-field coupling to explain the experimental observations. Using a transient frequency resolved pump-probe experiment we measure the differential transmission of the system, revealing the expected signs of coupling [14]. We explore several areas of interest, including the effects of high pump power which causes the quantum well to act as a continuum of states rather than a single resonance. In this regime our simple toy model is no longer valid and new features of the coupling are observed. Finally, we compare the optical properties and effective coupling of three distinct optical antenna shapes: wire, square and split-ring.

2. Methods

2.1. Quantum well

The semiconductor quantum well structure used in this work is grown using molecular beam epitaxy (MBE). The semiconductor structure is pictured in the inset of figure 1, and is grown lattice matched to an indium phosphide substrate. The quantum well is a 13.8 nm layer of $In_{0.532}Ga_{0.468}As$ surrounded by $In_{0.534}Al_{0.466}As$ barriers. The top barrier of the quantum well is approximately 2.9 nm thick, and a layer of $In_{0.532}Ga_{0.468}As$ approximately 2.5 nm thick is deposited to

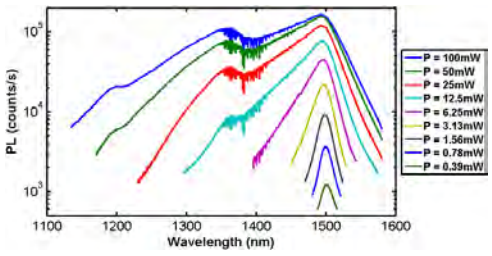

Figure 2. Power dependent low temperature photoluminescence spectra of the near-surface quantum well. Each curve corresponds to a pump power of approximately twice that of the curve below it.

act as a protective cap layer to prevent oxidation of the $In_{0.534}Al_{0.466}As$ barrier. This results in a distance of only 5.4 nm between the quantum well and the surface of the sample. It has been reported that surface states of a semiconductor can be extremely detrimental to quantum wells and dots [18]. As the quantum well gets closer to the surface non-radiative recombination increases quickly, leading to decreased photoluminescence (PL) and spectral broadening and shifting. At the same time, it has been shown that the coupling between a quantum well and a plasmonic system occurs through near-field interactions, which fall off quickly as a function of separation [19]. It is therefore necessary to make a compromise between the coupling strength and the quality of the quantum well. The distance of 5.4 nm has proven to be a very good compromise, maintaining a bright quantum well resonance with a FWHM of about 15 nm, while still coupling to the plasmonic structure. Two quantum well samples were used for this work; HSG64 was used for the pump power dependence measurements while A107 was used for comparison of antenna shapes.

The quantum well is designed to have a resonance wavelength near 1500 nm, which is verified using low temperature PL measurements. The quantum well is held at 10 K and pumped using 120 fs pulses at a wavelength of 810 nm from a Ti : Sapphire laser, with an 80 MHz repetition rate. Figure 2 shows the observed PL of this quantum well for various average pump powers. For low pump power we clearly see the lowest level of the quantum well at a wavelength 1500 nm. As the power is increased the PL broadens asymmetrically to higher energies (shorter wavelengths) and we begin to see signs of transitions from higher energy levels at wavelengths of 1360 nm and 1200 nm.

2.2. Optical antennas

Fabrication of the silver antenna array structures is accomplished using a standard lift-off procedure. Beginning with the quantum well structure, the sample is coated with a thin layer (∼200 nm) of poly(methyl methacrylate) (PMMA). The antenna pattern is written into this layer using an electron beam lithography system, and developed. The sample is then coated with 30 nm of high purity silver using electron beam deposition. Finally the PMMA is dissolved, resulting in the lift-off of the excess silver, leaving behind arrays of silver

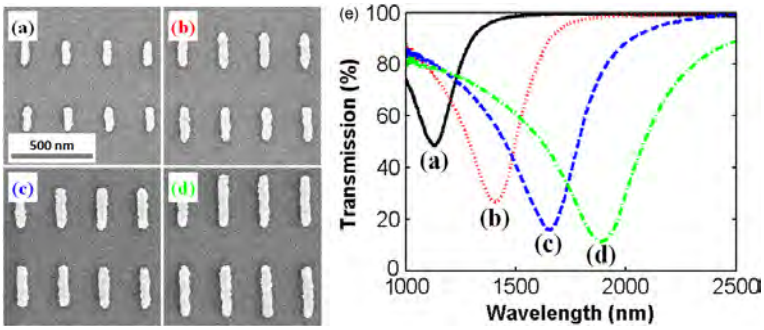

Figure 3. (a–d) SEM images of four silver wire antenna arrays with increasing lengths and (e) the FTIR transmission spectra corresponding to the four SEM images showing the shift in resonance wavelength.

antennas. For this work the antennas are patterned into square arrays with a size of 100 μm × 100 μm. In order to maximize the measured signal the density of antennas was made relatively high. Wire antennas were spaced on a rectangular grid with 250 nm spacing along the direction perpendicular to the wire, and 250 nm plus the length of the wire antenna (190–220 nm) spacing along the direction parallel to the wire. An example of this is shown in figure 3. To increase the density further, wire antennas were also fabricated with 250 nm spacing along both directions and alternating rows were shifted by 125 nm in order to avoid contact between the antennas. The dimensions of split-ring shaped antennas are such that a spacing of 250 nm on a square lattice was easily achievable. The dimensions of square antennas, however, required that the spacing be increased. For the array used in this study the spacing was 410 nm in order to avoid contact between antennas.

Completed antenna arrays are initially characterized using scanning electron microscopy (SEM) and room temperature Fourier transform infrared (FTIR) spectroscopy. We observe that the resonance shifts slightly when the samples are cooled to 10 K, however, room temperature measurements allow us to quickly find arrays which are suitable for study at low temperatures. For theoretical fits shown later in the paper we use low temperature transmission measurements. Figure 3 shows several SEM images of completed wire antenna arrays and the corresponding FTIR transmission spectrum showing the deep transmission dip of the plasmonic resonances. The resonance of the antenna array is strongly related to the size and spacing of the individual antennas. Since we are interested in high density antennas we tuned the antenna resonances by changing the dimensions of individual antennas during fabrication. This is illustrated in figure 3 which shows SEM images of four arrays with increasing antenna length and the corresponding shift in resonance. It is important to note that the transmission is measured with the electric field polarized linearly parallel to the long axis of the wire antennas. The orthogonal polarization does not couple to the dipole moment of the wire antenna, and shows nearly 100% transmission. This also applies to split-ring shaped antennas, shown later in this paper. For this shape the electric field is polarized along the opening of the 'U' of the split-ring in order to excite the fundamental mode. For perfectly square antennas the polarization would not make a difference, however, due to imperfections in fabrication these antennas are never perfectly square and tend to have a small shift of the resonance when the polarization is rotated.

2.3. Toy model

The system of a silver optical antenna array coupled to a quantum well can be understood to some extent by employing a simple model [17], in which the quantum well is modeled by a fermionic two-level system, and the antenna array is modeled as a bosonic two-level system. This model has been shown to provide good qualitative agreement for arrays of split-ring shaped antennas coupled to a quantum well [14]. The general physics behind this model assumes that the coupling between the two systems takes place via the near-field generated by the dipole moment of each. To account for the near-field the driving electric field for the quantum well is modified by the macroscopic polarization of the antenna array multiplied by a phenomenological coupling constant, L, and similarly the driving field for the antenna array is modified by the macroscopic polarization of the quantum well multiplied by the same constant. The transition amplitudes are calculated using steady state solutions of the optical Bloch equations. From this the linear optical spectra of the coupled system can be calculated. The final model includes ten parameters: density (N), dipole moment (d), resonance frequency (Ω) and damping constant (γ) for both the quantum well and the antenna array, along with the coupling constant (L) and the quantum well inversion which we control with a filling factor (f), which ranges from 0 to 1. Using independent measurements of the quantum well and the antenna array, we can fix all of the parameters except for f and L. For comparison to our pump-probe measurements we assume that the quantum well is inverted ($f = 1$) with the pump present and relaxed ($f = 0$) when the pump is blocked. This leaves only the coupling constant L as a free parameter which we can vary to fit our measurements of the coupled antenna/quantum well system.

2.4. Pump-probe spectroscopy

In order to experimentally investigate the unique properties of the coupled antenna/quantum well system we use a transient pump-probe spectroscopy technique. The sample is held at 10 K in a continuous flow helium cryostat and pumped using a 120 fs pulse at a wavelength of 810 nm from a mode-locked Ti : Sapphire laser. A portion of the Ti : Sapphire laser is also used to pump an optical parametric oscillator which produces a second pulse tunable in the wavelength range of 1360 nm–1580 nm and serves as a probe. Both pulses are combined collinearly and focused onto the sample. Using a telescope for each beam, the relative beam width, and hence the relative spot size on the sample is controlled. The pump spot size is about 20 μm while the probe spot size is on the order of 10 μm, ensuring that the area of the sample being probed is uniformly pumped. The power of the probe beam is held at 15 μW, while the pump power is tunable from very low powers (<100 μW) up to 120 mW average power. The pump beam is chopped at 400 Hz before the sample, and any residual pump is filtered out behind the sample by an interference filter. The transmitted probe is incident on an amplified InGaAs detector and the signal is measured using a lock-in amplifier referenced to the 400 Hz chopper. By normalizing this signal to the absolute transmission of the probe with no pump present we retrieve the differential transmission signal ($\Delta T/T$). Using a delay line to vary the time between the pump and probe pulses we can see the decay characteristics of the sample. This technique is very sensitive to small changes (down to 0.01%) in the transmission of the sample resulting from the incident pump beam.

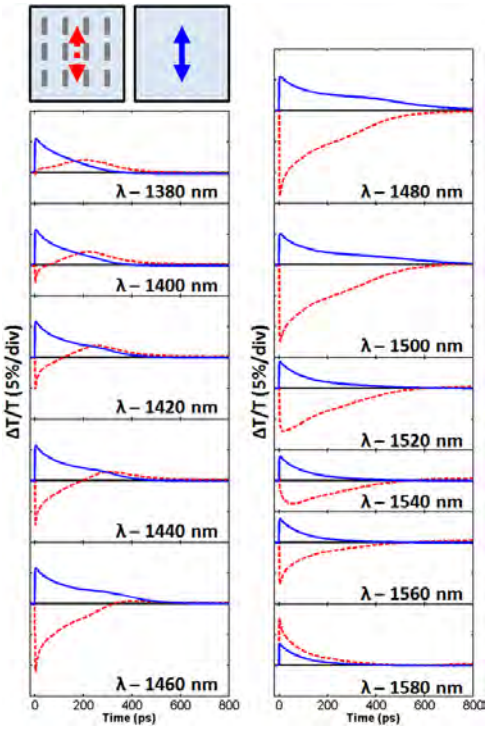

Figure 4. Transient pump-probe data collected from both the quantum well alone (solid blue) and from a resonant silver wire antenna array coupled to the quantum well (dashed red), for a pump power of 120 mW and probe wavelength ranging from 1380 nm to 1580 nm.

3. Results

3.1. High pump power differential transmission

Initial investigations were done using wire shaped antennas and the full 120 mW of available pump power. Figure 4 shows the transient response observed from an array resonant with the quantum well. An SEM image of this array and the low temperature transmission spectrum are shown in figure 5. In figure 4 the solid blue curves show the response of the quantum well alone measured approximately 100 μm away from the antenna array. The dashed red curves show the response measured on the array. Each set of curves corresponds to a different probe wavelength, as the probe was tuned from 1380 nm to 1580 nm in 20 nm step sizes. These initial results revealed several exciting features, including a very large negative signal of −13.9% at a wavelength of 1480 nm. While this negative signal has been observed before and can be explained in terms of the toy model, the magnitude of this signal is larger than previously observed in this type of system [14]. Additionally, the data reveal unique decay characteristics which cannot be described by a single exponential decay. This was observed not only on array but also from the quantum well by itself. Another interesting feature is the change of signs of the signal. For several wavelengths

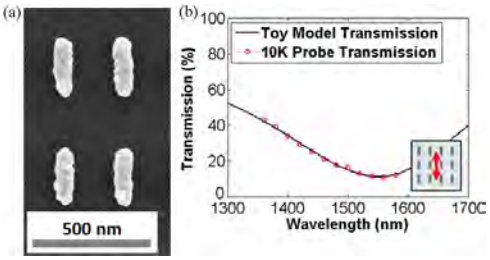

Figure 5. (a) SEM image of the silver wire antenna array measured in figures 4, 6, 8 and 9 and (b) low temperature transmission spectrum of this array.

(1380 nm–1440 nm) the on array signal is initially negative, but becomes positive at longer delay times before returning back to zero. A final notable feature is observed at a probe wavelength of 1540 nm. While all other probe wavelengths show very fast rise (fall) times on the order of 2–3 ps, for the

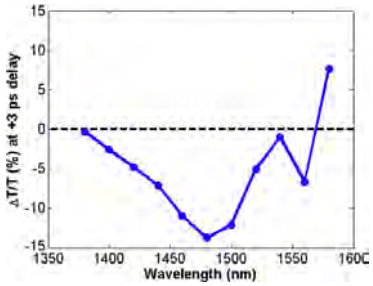

Figure 6. Pump-probe differential transmission spectrum for a pump power of 120 mW and a delay time of +3 ps.

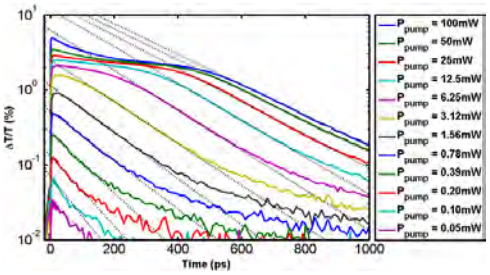

Figure 7. Transient pump-probe measurement of the quantum well without silver wire antennas for pump powers ranging from 50 μW to 100 mW. The data are plotted on a logarithmic scale along with exponential fits (dashed lines). Each curve corresponds to a pump power of approximately twice that of the curve below it.

wavelength of 1540 nm, the data show a rather slow fall, which reaches a minimum value after 60 ps.

Another way to view this data is to look at a specific delay time and plot the data as a function of wavelength as shown in figure 6. In this case the delay time is chosen to be +3 ps where we see the largest response for most wavelengths. This reveals another unique feature. Similar to previously reported data, the signal shows a strong negative response near resonance; however, we also see a second narrower and smaller dip in the data near 1560 nm which cannot be qualitatively explained by the toy model.

3.2. Bare quantum well

While the response of the coupled antenna/quantum well system shows many unique features, it was also noted that the response of the quantum well alone was rather unique. Not only did it show a complex decay characteristic, but it also had a rather large magnitude of nearly 5%. For a typical quantum well in this material system one would expect around 2% change resulting from bleaching of the absorption and from gain. This suggests that the additional signal is due to a change in reflection, most likely resulting from a change in refractive index due to the high carrier concentration generated by the large pump power. To verify this result we did several tests, the first being to measure a similar semiconductor structure, without the quantum well. This was measured and did in fact reveal a signal with a magnitude of approximately 3% and a nearly exponential decay on the time scale of 260 ps. We also investigated the dependence of the quantum well response on the pump power. Figure 7 shows the results of this measurement, where each curve is measured with a pump power of about one half of the pump power of the curve above it, starting from 100 mW at top and ending with 50 μW at bottom, and the probe wavelength is held constant at 1480 nm, corresponding to the peak of the quantum well resonance. The data are plotted on a logarithmic scale and the final portion of each decay is fit to a single exponential, with decay constants ranging from 82 ps at 100 μW pump power to 212 ps at 100 mW pump power. For low pump powers we see that a single exponential is sufficient to fit the data. This continues as the pump power increased to about 3.12 mW, where we see a shoulder begin to appear before the exponential decay, and likely signals the saturation of the lowest level of the quantum well. Indeed, if we look back at figure 2, showing the PL of the same quantum well, we see the second level of the quantum well begins to appear for powers above 3.12 mW. Also, consistent with this idea is the fact that this shoulder appears near a signal magnitude of about 2%, the value we expect to get from the quantum well alone. As the pump power is increased further, this shoulder lengthens in time, until a power of about 25 mW, at which point a second component appears, causing the signal to increase to nearly 5%. We attribute this additional component to the changing refractive index of the bulk material resulting from the high carrier concentration, which was also observed in the sample without a quantum well as mentioned above.

3.3. Low power differential transmission

With this in mind we decided to revisit the array we had previously measured and look at the response when the quantum well is pumped with only 4 mW, which should be just enough power to invert the lowest energy resonance of the quantum well. In figure 8 we see this data plotted similar to the data in figure 4, where the solid blue curves show the response of the quantum well by itself and the dashed red curves show the response of the quantum well coupled to the wire antenna array. From this data we see a smaller magnitude of the negative signal of about −3.8%. Also for most wavelengths we see a nearly exponential decay and the initial rise (fall) time is consistent, reaching a maximum or minimum signal at +20 ps delay. For the wavelengths of 1440 nm and 1460 nm we still see a flip in the sign of the signal. In order to compare this to previous work, we can use the toy model explained previously. To do this we first look at a single delay time corresponding to the maximum signal, when hot carriers have relaxed to the lowest energy level of the quantum well and the system can be approximated as steady state, which occurs around +20 ps. When we plot this time slice as a function of probe wavelength we get the plot seen in figure 9.

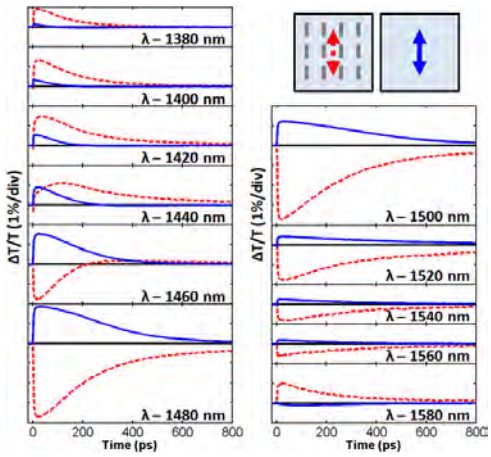

Figure 8. Transient pump-probe data collected from both the quantum well alone (solid blue) and from a resonant silver wire antenna array coupled to the quantum well (dashed red), for a pump power of 4 mW and probe wavelength ranging from 1380 nm to 1580 nm.

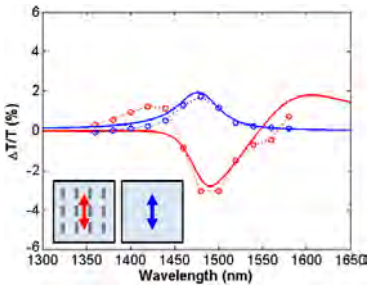

Figure 9. Pump-probe differential transmission spectra collected for a pump power of 4 mW and a delay of +20 ps. The blue circles show the measured signal from the quantum well alone, while the red circles show the measured signal on the silver wire antenna array. The solid blue and dashed red curves show the best fit to the simple model.

Here again the blue data are the response of the quantum well and the red data are the response of the coupled system. The open circles are the experimental data, while the curves are the best fit to the toy model. All but one parameter in this model can be set from independent measurements of the quantum well and wire antenna array, leaving one free parameter, representing the strength of the coupling (L), which is varied to obtain this fit. The parameters for the quantum well were: resonance frequency of $2\pi \times 203$ THz, damping frequency of $2\pi \times 4.0$ THz, dipole moment of 5.8×10^{-29} Cm and density of 2.1×10^{24} m^{-3}. The parameters for the wire antenna array were: resonance frequency of $2\pi \times 191$ THz, damping frequency of $2\pi \times 10$ THz, dipole moment of 9.9×10^{-26} Cm and density of 3.7×10^{20} m^{-3}. The best fit of the coupled data was found for a coupling constant of 0.51×10^{10} m F^{-1}. From this fit we see there is extremely good qualitative agreement with this model, confirming that for low excitation power the quantum well does indeed behave like a two-level system.

It is also important to check the polarization dependence of the pump-probe measurement. Since the wire antennas can only be excited by light polarized parallel to the long axis, we would expect that if we rotate the polarization of the probe light to be perpendicular to the long axis we would probe only the quantum well. An example of this can be seen in figure 10, where a wire antenna array is measured with a pump power of 4 mW and a probe wavelength of 1480 nm. In figure 10(a) we probe both the quantum well by itself (solid blue) and the quantum well coupled to the wire antenna array (dashed red), however, the polarization of the probe is such that it does not interact with the wire antennas. We see a similar magnitude and decay of the transient response for both measurements in this case. In figure 10(b), when the polarization is rotated 90° such that it will interact with the wire antennas, we see the same response from the quantum well (solid blue), but now we see a much different behavior from the quantum well coupled to the wire antenna array (dashed red) as we expected.

3.4. PL

It's also very interesting to look at the low temperature PL, providing complimentary information to the differential transmission measurements. To measure the PL we use the same experimental setup that is used for transient pump-probe measurements in order to maintain the same pumping conditions (power, spot size, etc). The probe beam is blocked and a flip mirror is used to divert the PL to a 0.5 m spectrometer with a 600 line mm^{-1} grating. The spectra are captured with a liquid nitrogen cooled 512×1 pixel InGaAs array.

Using this method we can study the resonant changes in PL associated with the antenna arrays. Figure 11 shows an example of the resonant enhancement in PL that we observe from a wire antenna array (solid blue), when the quantum well is pumped with 100 mW average power. Also plotted for reference is the extinction cross section of the wire antenna array as measured by room temperature FTIR (dashed red). To measure the enhancement of the PL an analyzing polarizer is placed before the spectrometer such that we can separate PL emitted with polarization both parallel and perpendicular to the long axis of the wire antennas. The solid blue curve in figure 11 is the ratio of parallel polarized PL to perpendicular polarized PL. Additionally, it is normalized by the same ratio of PL collected from the quantum well alone in order to remove any polarization sensitivity of the measurement optics. From this we can see a clear peak associated with the plasmonic resonance, with a maximum enhancement of 2.3.

3.5. Antenna comparison

As a result of the skin depth of metal being on the same scale as the dimensions of optical antennas, the exact shape of the

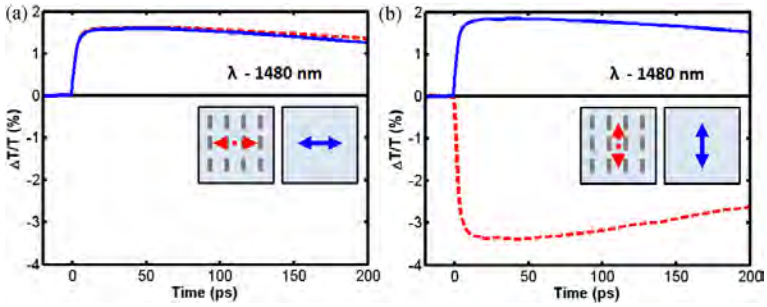

Figure 10. Polarization dependence of the pump-probe measurement. When probed with horizontal polarization (a) the response is very similar both on (dashed red curve) and off (solid blue curve) of the silver wire antenna array since the antennas do not couple to this polarization. When probed with vertical polarization (b) the response on array (dashed red curve) is quite different than the response from the quantum well alone (solid blue curve), showing the clear signs of coupling between the quantum well and wire antennas.

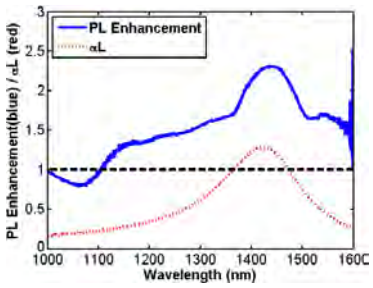

Figure 11. Resonant photoluminescence enhancement (solid blue), measured by taking the ratio of PL emitted with polarization parallel to the axis of the wire antennas to the PL emitted with polarization perpendicular to the axis of the wire antennas. The dashed red curve shows the extinction cross section of the same array measured by room temperature FTIR.

antenna has a strong influence on its properties such as resonant frequency, dipole moment and damping. One would also expect the strength of the coupling to depend on the antenna shape. To study this aspect we fabricated arrays of silver optical antennas with three different shapes on the same quantum well. This quantum well (A107) had the same structure as the previously discussed quantum well, however, was grown in a different MBE chamber and had approximately twice the PL intensity of the first quantum well. The size of the antennas was adjusted such that all three had resonance wavelengths near 1500 nm. Wire shaped antennas were fabricated in a staggered pattern in order to increase density ($N = 5.3 \times 10^{24}\ m^{-3}$) which leads to a stronger differential transmission signal. Split-ring shaped antennas were fabricated with the same density; however, due to the size, square shaped antennas were limited to a lower density ($N = 2.0 \times 10^{24}\ m^{-3}$). Figure 12 shows SEM images of these three antenna shapes along with measured transmission data. These transmission data were measured at 10 K using the probe of the pump-probe experiment, and the toy model has been fit to it in order to retrieve the properties of the antennas, summarized in table 1. From this we find that the split-ring shaped antennas have the smallest dipole moment, while the square antennas have a dipole moment more than twice that of the wire or split-ring shapes. From previous measurements on individual antennas [15] we expected the cross section (and therefore the dipole moment) of square antennas to be larger than that of wire and split-ring antennas. Surprisingly, we find all three to have similar damping terms, with the split-ring shape having the largest damping and the squares having the smallest. This was not expected from measurements of individual antennas; however, at such a high density of antennas, the interaction of individual antennas likely has a larger effect on the damping than the shape of the antennas [16].

For each array differential transmission data were collected on the array and also from a region directly next to it with no antennas with an average pump power of 4 mW. These data are plotted in figure 13. In this figure the data collected from the quantum well alone are once again shown in blue while the data from the coupled system are shown in red. Since all three arrays were fabricated during the same process on the same quantum well, the behavior of the quantum well (solid blue) was very similar for all three and the average parameters for the quantum well are summarized in table 1. Finally, with these parameters fixed we can vary the coupling parameter (L) in order to best match the differential transmission signal of the coupled system. These fits are shown by the dashed red curves in figure 13, and the effective coupling parameter (L) is summarized in table 1. We also include in table 1 an effective coupling frequency [17] which accounts for the dipole moment and density of the two systems.

$$V_{\mathrm{eff}} = \hbar^{-1} d_{\mathrm{array}} d_{\mathrm{QW}} L \sqrt{N_{\mathrm{array}} N_{\mathrm{QW}}}$$

From these fits we find that the split-ring antennas show the greatest coupling, both in terms of the coupling parameter (L) and the effective coupling frequency (V_{eff}). Surprisingly,

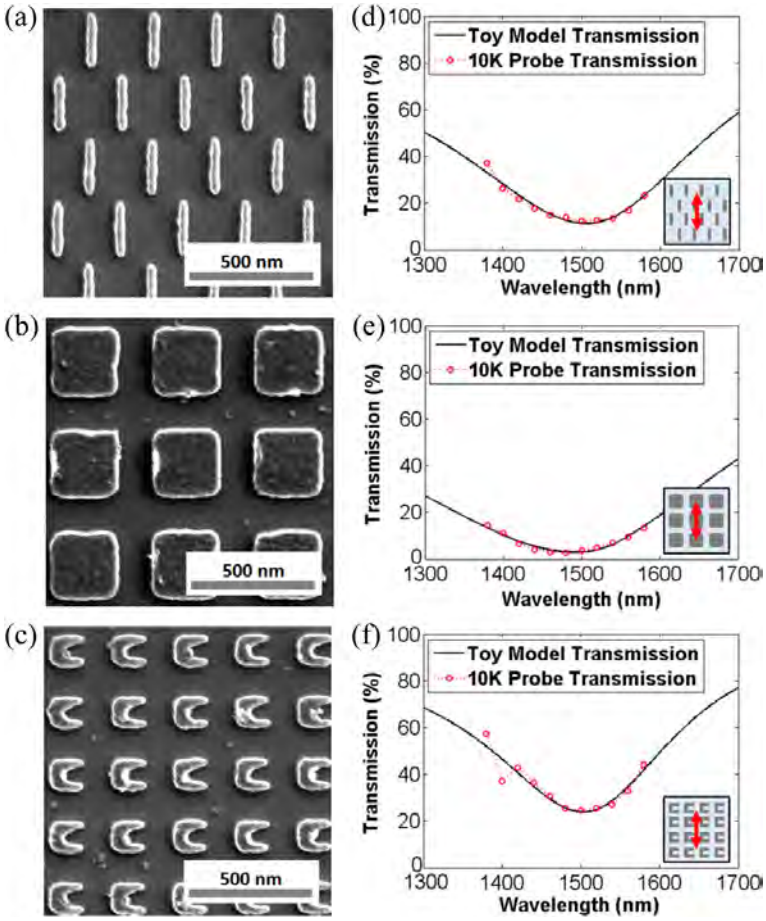

Figure 12. SEM images of wire (a), square (b), and split-ring (c) shaped silver antennas, along with the corresponding transmission data (d–f) as measured by the probe beam of the pump-probe experiment.

Table 1. Summary of toy model parameters from fit to experimental data.

	Quantum well	Wire antennas	Square antennas	Split-ring antennas
ω	$2\pi \times 204$ THz	$2\pi \times 197$ THz	$2\pi \times 198$ THz	$2\pi \times 198$ THz
γ	$2\pi \times 8.6$ THz	$2\pi \times 9.4$ THz	$2\pi \times 7.7$ THz	$2\pi \times 9.7$ THz
d	8.7×10^{-29} Cm	7.8×10^{-26} Cm	17×10^{-26} Cm	5.8×10^{-26} Cm
N	2.1×10^{24} m^{-3}	5.33×10^{20} m^{-3}	1.98×10^{20} m^{-3}	5.33×10^{20} m^{-3}
L	—	0.38×10^{10} m F^{-1}	0.18×10^{10} m F^{-1}	0.56×10^{10} m F^{-1}
V_{eff}	—	8.4 THz	5.0 THz	9.1 THz

the square antennas which had the largest dipole moment show the smallest coupling. Looking at the data in figure 13 we see that the coupled system fit for this antenna was the poorest, with the magnitude of the measured signal reaching −4.3% at a wavelength of 1460 nm, while the fit only reaches a value of −2.2%. However, if we manually vary the coupling parameter in our fit to match the magnitude of the measured differential signal we find only a slight increase of the coupling parameter to 0.24×10^{10} m F^{-1}, still much smaller than that of the split-ring or wire antenna.

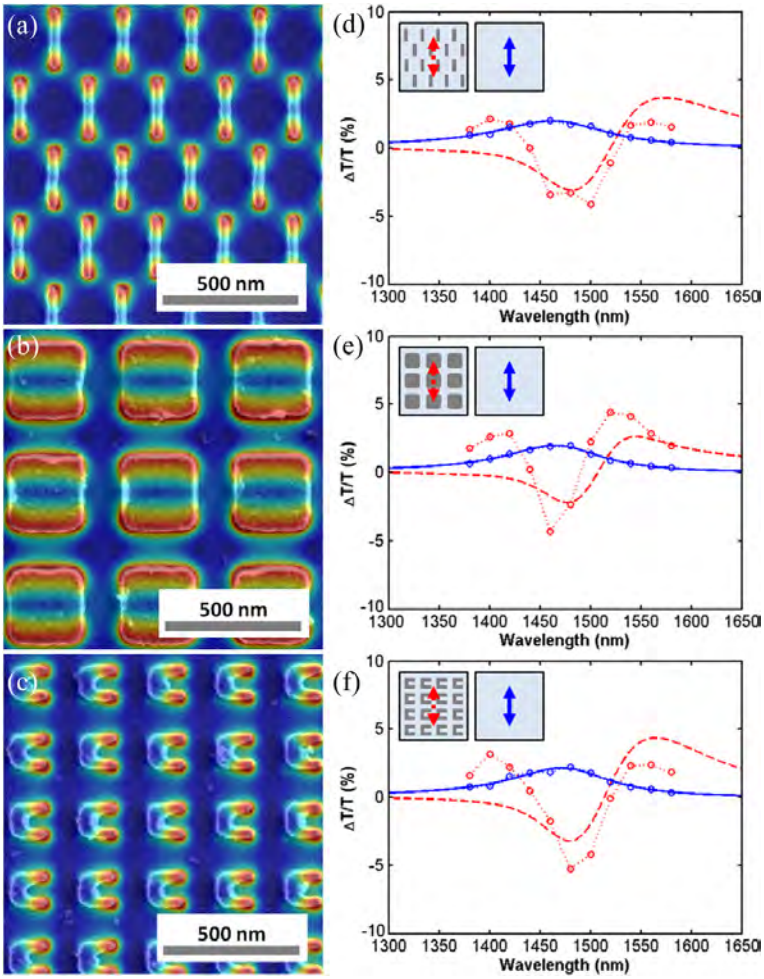

Figure 13. Normalized electric field distribution in the plane of the quantum well as simulated by FDTD overlaid on SEM images of (a) wire, (b) square and (c) split-ring antenna arrays along with differential transmission measurements both on (red) and off (blue) of the (d) wire, (e) square and (f) split-ring antenna arrays. Measured data are plotted with circles while the best toy model fit is plotted as solid blue and dashed red lines.

4. Discussion and conclusion

In conclusion, we have experimentally studied the coupling of silver optical antennas to a semiconductor quantum well 5.4 nm below the surface. We study the properties of the near-surface quantum well alone, finding a saturation of the first energy level at an average pump power of 4 mW. With this information we study the coupled antenna/quantum well above and below saturation. Below saturation we find that the observed data can be fit by a toy model which reveals the effective coupling of the system. Above saturation we observe large differential transmission signals, but the data analysis is complicated by the changing refractive index of the substrate. At high pump powers we observed two decay time constants, one which we attribute to the decay of the lowest energy level and one which likely corresponds to the decay of carriers in the bulk.

Low temperature PL measurements reveal resonant enhancement from the antenna arrays. This enhancement is observed in the PL emitted with light polarized along the long axis of wire antennas relative to PL emitted with polarization in the orthogonal direction. This measure shows a clear peak

enhancement of 2.3 centered near the measured transmission resonance of the antenna.

Finally, we investigate the effect of the antenna shape on the effective coupling parameter. We fabricate arrays of wire, square and split-ring shaped antennas on the same semiconductor quantum well. We measure the low temperature transmission of each array and find that the dipole moment of the square antenna is more than twice as large as that of the wire or split-ring shape. We also note that the damping of the arrays is similar for all antenna shapes. We attribute this to increased damping due to the interaction of the densely packed antennas which is greater than the effect of the antenna shape alone. Pumping with an average power of 4 mW in order to stay below saturation, we measure the differential transmission of arrays of each shape. Although the magnitude of the differential transmission signal is similar for all three antennas, we find that the effective coupling is smallest for the square shape. At first this observation seems surprising given that the quantum well and antennas interact through their dipole moments and the square antenna clearly has a larger dipole moment. However, a closer look at the toy model reveals an explanation for this. The effect of the coupling on each system is included through a term which is the product of the coupling parameter (L) and the macroscopic polarization of the other system. In these terms the dipole moment factors only into the macroscopic polarization. The coupling parameter (L) depends only on the geometry of the system, *i.e.* the local density of optical states (LDOS) at the location of the two-level system. This will depend not only on the separation of the two-level system from the antenna, as shown in [19], but also on the mode distribution. Assuming only one antenna mode at the frequency of interest, we would expect the LDOS to decrease as the mode volume increases. Based on the size of the antennas alone we can see that the mode of the square antenna will be much larger than that of the split-ring or wire antennas. From this reasoning, we can expect there to be a lower LDOS at the quantum well and a lower coupling parameter (L). This trend is also seen in FDTD simulations like those shown in figure 13. Looking in the plane of the quantum well, the ratio of the peak electric field to the average electric field over a unit cell is on the order of four for dipole and split-ring antennas, but only about two for square antennas showing that the field of the square antenna is less localized. In order to account for the dipole moment and density we must consider the effective coupling frequency (V_{eff}). Even by this comparison the split-ring shaped antenna has a higher effective coupling frequency than the wire or square shapes. The larger dipole moment of the square antenna is not enough to compensate for the smaller coupling parameter (L) and the lower density (N_{array}).

Acknowledgements

This work was funded by the Air Force Office of Scientific Research (AFOSR, Dr Gernot Pomrenke, Grant FA9550-13-1-0003), the National Science Foundation Atomic, Molecular and Optical Physics (NSF-AMOP 1205031) and the National Science Foundation Engineering Research Center for Integrated Access Networks (ERC-CIAN, Award EEC-0812072). We thank KIT, the State of Baden-Württemberg, and Deutsche Forschungsgemeinschaft (DFG) for support through the Karlsruhe School of Optics and Photonics (KSOP) and the DFG-Center for Functional Nanostructures (CFN) via subproject A1.5. MG would like to acknowledge the support of the Department of Defense through the National Defense Science and Engineering Graduate (NDSEG) Fellowship Program. SZ would like to acknowledge the support of the Department of Energy (DOE) through the Office of Science Graduate Fellowship (SCGF) made possible in part by the American Recovery and Reinvestment Act of 2009, administered by ORISE-ORAU under contract no. DE-AC05-06OR23100. JH would like to acknowledge support from the Air Force Office of Scientific Research (AFOSR, Program Manager—Dr Gernot Pomrenke, Contract 12RY05COR). JS would like to acknowledge the support of Arizona Technology and Research Initiative Funding (TRIF).

References

[1] Novotny L 2007 The history of near-field optics *Progress in Optics* ed E Wolf (New York: Elsevier) vol 50 pp 137–84
[2] Fischer U C and Pohl D W 1989 Observation on single-particle plasmons by near-field optical microscopy *Phys. Rev. Lett.* **62** 458–61
[3] Biagioni P, Huang J-S and Hecht B 2012 Nanoantennas for visible and infrared radiation *Rep. Prog. Phys.* **75** 024402
[4] Farahani J N, Eisler H J, Pohl D W, Pavius M, Flückiger P, Gasser P and Hecht B 2007 Bow–tie optical antenna probes for single-emitter scanning near-field optical microscopy *Nanotechnology* **18** 125506
[5] Akimov A V, Mukherjee A, Yu C L, Change D E, Zibrov A S, Hemmer P R, Park H and Lukin M D 2007 Generation of single optical plasmons in metallic nanowires coupled to quantum dots *Nature* **450** 402
[6] Curto A G, Volpe G, Taminiau T H, Kreuzer M P, Quidant R and van Hulst N F 2010 Unidirectional emission of a quantum dot coupled to a nanoantenna *Science* **329** 930
[7] Cao L, Fan P, Vasudev A P, White J S, Yu Z, Cai W, Schuller J A, Fan S and Brongersma M L 2010 Semiconductor nanowire optical antenna solar absorbers *Nano Lett.* **10** 439
[8] Fang X, Tsend M L, Ou J-U, MacDonald K F, Tsai D P and Zheludev N I 2014 Ultrafast all-optical switching via coherent modulation of metamaterial absorption *Appl. Phys. Lett.* **104** 141102
[9] Hess O, Pendry J B, Maier S A, Oulton R F, Hamm J M and Tsakmakidis K L 2012 Active nanoplasmonic metamaterials *Nat. Mater.* **11** 574–84
[10] Kumar N 2013 Spontaneous emission rate enhancement using optical antennas *PhD Dissertation* Electrical Engineering and Computer Sciences, UC Berkeley, Berkeley, CA
[11] Greffet J-J, Laroche M and Marquier F 2010 Impedance of a nanoantenna and a single quantum emitter *Phys. Rev. Lett.* **105** 117701
[12] Maier S A 2006 Plasmonic field enhancement and SERS in the effective mode volume picture *Opt. Express* **14** 1957
[13] Koenderink A F 2010 On the use of Purcell factors for plasmon antennas *Opt. Lett.* **35** 4208

[14] Meinzer N, Ruther M, Linden S, Soukoulis C M, Khitrova G, Hendrickson J, Olitzky J D, Gibbs H M and Wegener M 2010 Arrays of Ag split-ring resonators coupled to InGaAs single-quantum-well gain *Opt. Express* **18** 24140–51

[15] Husnik M, Niegemann J, Busch K and Wegener M 2013 Quantitative spectroscopy on individual wire, slot, bow–tie, rectangular, and square-shaped optical antennas *Opt. Lett.* **38** 4597

[16] Decker M, Feth N, Soukoulis C M, Linden S and Wegener M 2011 Retarded long-range interaction in split-ring-resonator square arrays *Phys. Rev.* B **84** 085416

[17] Wegener M, García-Pomar J L, Soukoulis C M, Meinzer N, Ruther M and Linden S 2008 Toy model for plasmonic metamaterial resonances coupled to two-level system gain *Opt. Express* **16** 19785–98

[18] Dreybrodt J, Forchel A and Reithmaier J P 1993 Optical properties of $Ga_{0.8}In_{0.2}As$/GaAs surface quantum wells *Phys. Rev.* B **48** 14741–4

[19] Meinzer N, König M, Ruther M, Linden S, Khitrova G, Gibbs H M, Busch K and Wegener M 2011 Distance-dependence of the coupling between split-ring resonators and single-quantum-well gain *Appl. Phys. Lett.* **99** 111104

Appendix G

Molecular beam epitaxy grown indium self-assembled plasmonic nanostructures

R. Gibson, M. Gehl, J. Sears, S. Zandbergen, N. Nader, P. Keiffer, J. Hendrickson, A. Arnoult, G. Khitrova

Journal of Crystal Growth, Vol. 425, pp. 307-311 (September, 2015)

Journal of Crystal Growth 425 (2015) 307–311

Contents lists available at ScienceDirect

Journal of Crystal Growth

journal homepage: www.elsevier.com/locate/jcrysgro

Molecular beam epitaxy grown indium self-assembled plasmonic nanostructures

Ricky Gibson [a,*], Michael Gehl [a], Jasmine Sears [a], Sander Zandbergen [a], Nima Nader [a,b,c], Patrick Keiffer [a], Joshua Hendrickson [b], Alexandre Arnoult [d], Galina Khitrova [a]

[a] College of Optical Sciences, University of Arizona, 1630 E University Blvd., Tucson, AZ 85721, USA
[b] Air Force Research Laboratory, Sensors Directorate, 2241 Avionics Circle, Wright-Patterson AFB, OH 45433, USA
[c] Solid State Scientific Corporation, 12 Simon St. Nashua, NH 03060, USA
[d] LAAS-CNRS, 7 Avenue du Colonel Roche, 31000, Toulouse, France

ARTICLE INFO

Available online 21 February 2015

Keywords:
A1. Nanostructures
A3. Molecular beam epitaxy
B1. Metals
B2. Semiconducting III–V materials

ABSTRACT

We describe molecular beam epitaxy (MBE) growth conditions for self-assembled indium nanostructures, or islands, which allow for the tuning of the density and size of the indium nanostructures. How the plasmonic resonance of indium nanostructures is affected by the island density, size, distribution in sizes, and indium purity of the nanostructures is explored. These self-assembled nanostructures provide a platform for integration of resonant and non-resonant plasmonic structures within a few nm of quantum wells (QWs) or quantum dots (QDs) in a single process. A 4 × increase in peak photoluminescence intensity is demonstrated for near-surface QDs resonantly coupled to indium nanostructures.

1. Introduction

The field of plasmonic nanostructures, where small volume structures can enhance electromagnetic fields that can be coupled to semiconductor quantum confined gain medium, is an expanding area of research. It has been shown that MBE grown silver films have improved optical constants, i.e. closer to intrinsic values, over e-beam or physical vapor deposited silver films [1]. This gives a possibility for improvements in the quality of plasmonic nanostructures or nano-antennas. It has also been shown that MBE can be used to grow site-controlled structures out of silver [2] and self-assembled structures with silver [3] and indium [4]. MBE growth allows for higher quality metallic nanostructures due to the improved optical constants and the self-assembly creates a clean interface between the metallic nanostructure and semiconductor underneath. In the self-assembled case there is also no need for fabrication or post-processing for optical experiments, eliminating possible sources of impurities and contamination. By tuning the sizes of these nanostructures the resonant wavelength can be tuned [5] to be in resonance with QWs [6,7] or QDs [8] just a few nanometers beneath the metallic structures. Growing these resonant indium islands in the same process as the semiconductor growth with MBE now opens up the possibility of encapsulating [9] the islands with more semiconductor material, including gain material. This would allow for larger coupling effects and possibly compensating metamaterial losses.

Here we present MBE growth conditions for indium islands, which allow for the tuning of the density, to well below 1 μm^{-2}, and size, from ~100 nm up to ~1.5 μm, of the indium islands. The larger island diameters are a result of a slow indium growth in the 1 ML/hr range, allowing for migration of the indium atoms throughout the growth.

2. Materials and methods

All samples have been grown on (100) GaAs wafers. The indium island samples have been grown in two different machines. The first is a Riber 32P where the sources are mounted on the rear vertical wall of the MBE growth chamber and aimed at the substrate which is mounted 25° from vertical, and 13° away from the most uniform growth position. In this chamber we have utilized 500 μm thick, double-side polished, two inch wafers cleaved into quarters for sample growth. These quarter wafers are held in three inch molybdenum substrate mounts (molyblocks) for quarter wafers with two tabs along the perpendicular sides. The other chamber used is a Riber 412 where the sources are mounted on the bottom of the MBE growth chamber and aimed at the substrate which is mounted horizontally in a five inch platen and the substrate is centered in the platen. In this chamber the growth is done on

* Corresponding author.
E-mail address: rgibson@optics.arizona.edu (R. Gibson).

http://dx.doi.org/10.1016/j.jcrysgro.2015.02.058
0022-0248/

350 μm thick, single-side polished, full two inch wafers which are n-doped with silicon (10^{-18} cm^{-3}). This chamber was used for all samples discussed below that have been grown with doped semiconductor layers. Both chambers utilize effusion cells with 7 N (7N5) purity indium in the Riber 32P (Riber 412).

After de-oxidizing the substrate, > 400 nm of GaAs is grown at a substrate temperature of ~580 °C. For samples grown with InGaAs QWs or InAs QDs the substrate temperature is dropped to ~485 °C for the growth of these structures. The QW or QDs are then capped with between 3 and 10 nm of GaAs grown at the same substrate temperature. For the indium island growth the substrate temperature is lowered by cutting off the current to the substrate heater. At a substrate temperature of ~300 °C the arsenic flux is cut off. Once the arsenic flux is off, the substrate heater is set at a constant current and the substrate is allowed to come to an equilibrium temperature, ~130 °C as measured with a type C thermocouple, while arsenic continues to be pumped out of the chamber. This time has been varied between 1 and 12 h. The indium island deposition then takes place with growth rates (beam equivalent pressure) between 0.27 ML/s (3.02×10^{-7} Torr) and 1 ML/hr or 0.00028 ML/s (3.97×10^{-10} Torr). In the latter case the indium cell temperature is only 60 °C above the standby temperature of the cell. The indium growth rate is given as the growth rate of InAs as calibrated from InAs QD growths.

Samples are characterized using atomic force microscopy (AFM), scanning electron microscopy (SEM), tunneling electron microscopy (TEM), energy dispersive x-ray spectroscopy (EDS), Fourier transform infrared (FTIR) transmission measurements, and photoluminescence (PL). By utilizing standard image processing techniques the sizes of the islands are extracted from AFM and SEM images.

3. Results

An interesting aspect of the indium island sample growths is the different distribution in island sizes achieved by the two different machines used. While there is expected to be small variations in substrate temperature and flux uniformity it is not expected that the indium islands grown in one chamber would have a Gaussian-like distribution in size while the other chamber would produce size distributions with a clear tail on the short side of the distribution. This is seen in Fig. 1(a) and (b) for the diameter

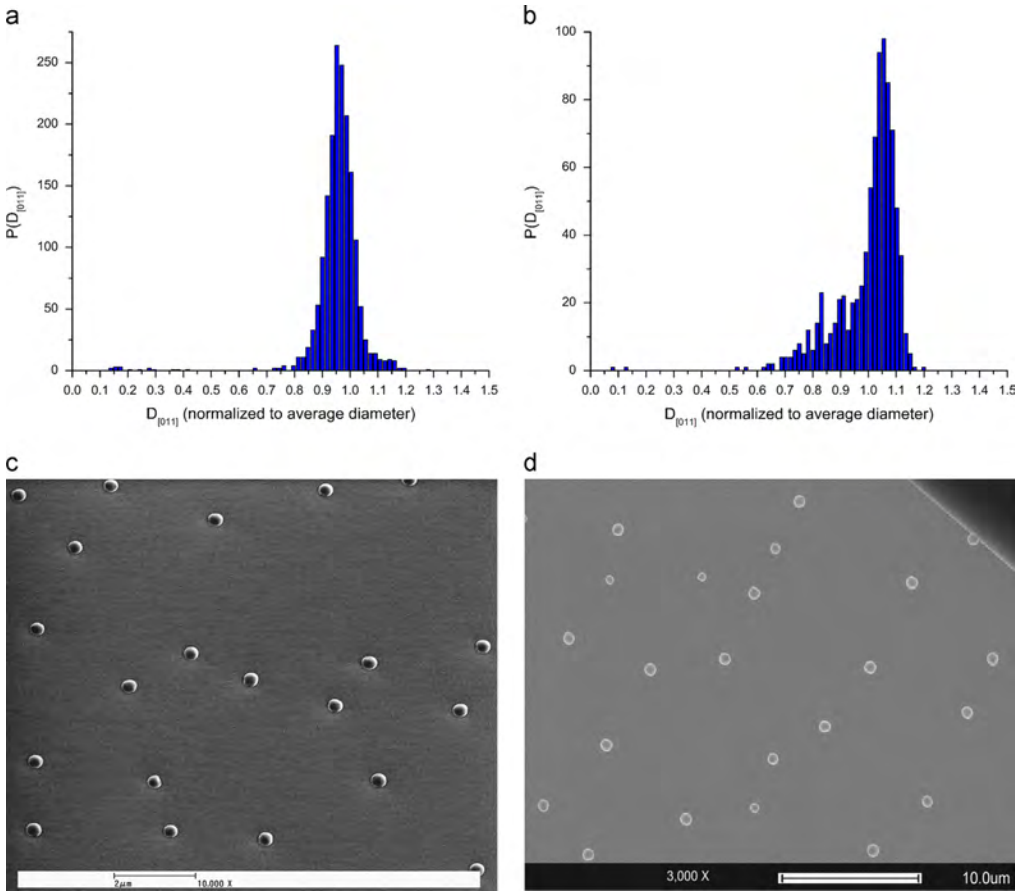

Fig. 1. Distribution of the diameter of the indium islands along the (011) crystal axis for a sample grown in the Riber 32 (a) and a sample grown in the Riber 412 (b). The distributions are scaled to their average diameter, which are 385 nm with a standard deviation of 34 nm and 834 nm with a standard deviation of 94 nm for samples shown in (a) and (b), respectively. (c) and (d) SEM images corresponding to the distributions in (a) and (b), respectively.

of the indium islands along the (011) crystal axis and can be seen along the (0–11) crystal axis as well as in the height of the indium islands, although this is not shown here. The indium island samples with the tail in the distribution are grown on silicon doped GaAs but this is not expected to affect the formation of the indium islands in such a manner. In either case the standard deviation of the distribution is ~10% of the average size for both samples. Both distributions in Fig. 1 are developed by analyzing the diameter of over 850 islands for each sample. The distribution with the tail looks similar to the asymptotic distribution of the Lifshitz–Slyozov $t^{1/3}$ growth law [10] which is familiar to the growth of II–VI QDs in a glass matrix [11]. The tailed distribution shown in Fig. 1(b) has a much narrower peak than the $t^{1/3}$ distribution but still suggests diffusion of the indium islands is taking place and the larger islands are growing at the expense of the smaller islands. From the corresponding SEM images in Fig. 1(c) and (d) it can be seen that the indium islands tend to cluster for the Gaussian-like distribution of sizes and the samples showing the tail in the distribution seem to have some degree of order where they prefer to align together perpendicular to the (011) crystal axis (major flat) shown in upper right hand corner of Fig. 1(c). This direction is also parallel to the surface roughness of the sample seen on SEM images.

As discussed in the previous section, a wide range in growth rates or beam equivalent pressures are used, roughly a factor of 1000 between the highest and the lowest. By varying the growth rate and the amount of indium deposited the indium islands size can be varied between a diameter of 120 nm and a diameter of 1.5 μm, corresponding to heights of 50 nm and 445 nm. The densities achieved have been between 10 μm^{-2} and 0.007 μm^{-2}. Fig. 2 shows plasmonic resonances, measured using FTIR, of several indium island samples along with corresponding

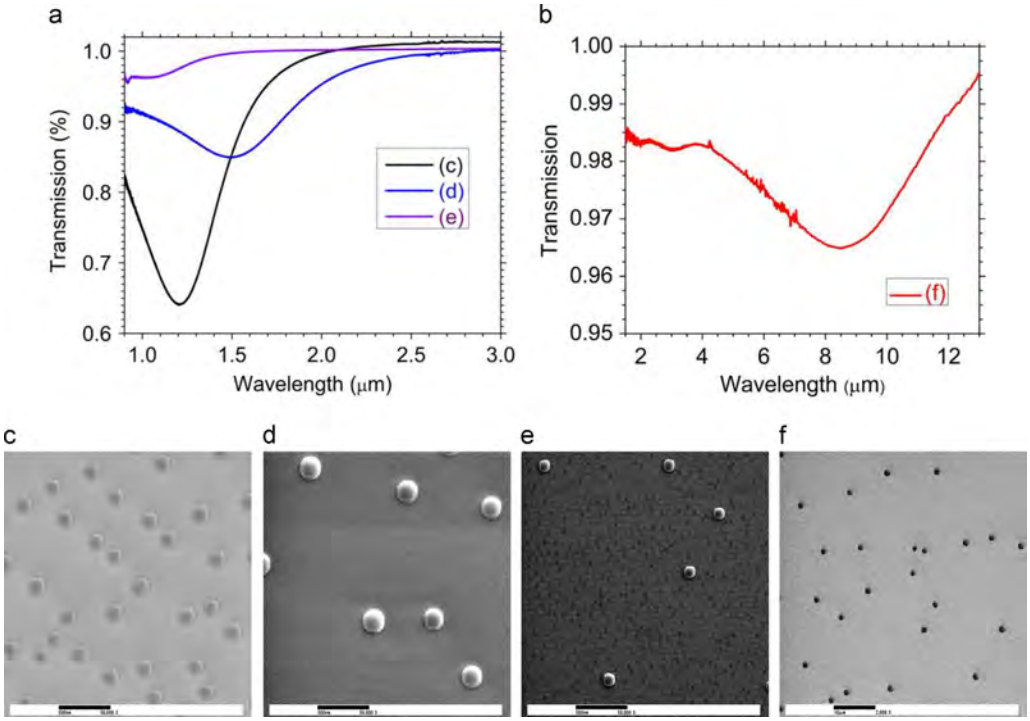

Fig. 2. (a) and (b) FTIR transmission measurements showing the plasmonic resonances of samples shown in the SEM images of (c), (d), (e), and (f). The scale bar in (c), (d), and (e) are 500 nm and in (f) is 10 μm.

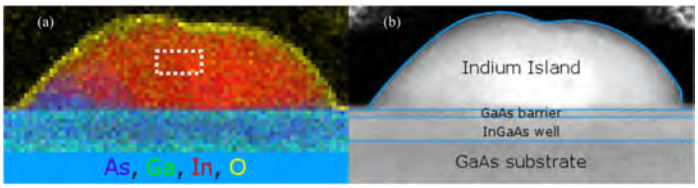

Fig. 3. (a) An EDS map of an island showing that it is predominantly indium (red) but also contains arsenic (violet), gallium (green), and oxygen (yellow). The white dashed box represents a 20 nm by 10 nm region where an indium concentration of 89.9% was measured. (b) A TEM image of the same island with the different regions of the structure outlined and labeled. (For interpretation of the references to color in this figure, the reader is referred to the web version of this article.)

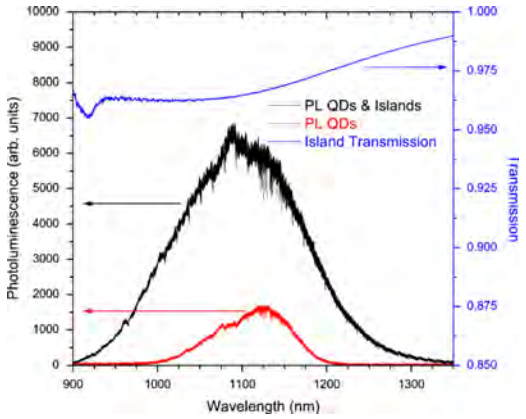

Fig. 4. PL of an indium island sample with 7 nm GaAs cap separating the InAs QDs and the indium islands (black), PL of just InAs QDs with a 7 nm GaAs cap (red), and the transmission spectra of the indium islands (blue). PL measured at 10.8 K and transmission measured at room temperature. (For interpretation of the references to color in this figure, the reader is referred to the web version of this article.)

SEM images for each sample. It is clear, that the larger islands have longer wavelength resonances and that a decrease in density of the indium islands decreases the collective transmission as measured by FTIR.

Using EDS measurements the chemical composition of several indium islands on a single sample have been determined. Before the sample is prepared for TEM and EDS measurements the sample is coated with carbon and platinum to protect the sample during processing of the TEM slice. As shown in Fig. 3(a), a color map showing the indium (red), gallium (green), arsenic (violet), and oxygen (yellow) mapping of a single island, the indium islands are predominantly indium. A TEM of the island with the sample structure outlined is shown in Fig. 3(b). In the dashed outline in the central area of the indium island in Fig. 3(a), representing a 20 nm by 10 nm section of the island, the indium concentration was measured to be 89.9% with only 5.6% gallium and 4.5% arsenic. Despite the presence of gallium and arsenic in the islands and an oxide layer covering the island the samples show a strong plasmonic resonance as shown in Fig. 2.

As described above, the indium islands can be grown in close proximity to InAs QDs where the separation between the indium islands and the QDs can be precisely controlled by the thickness of the GaAs capping layer. In Fig. 4 we show a 4× increase in the peak intensity of the ensemble PL of InAs QDs when indium islands are present. The red data in Fig. 4 is from an InAs QD with a 7 nm GaAs cap but no indium islands. The black data is from a sample with similar InAs QDs and indium islands, at an island density of $\sim 1\ \mu m^{-2}$, with a 7 nm GaAs cap separating the InAs QDs from the indium islands. For both samples the density of the QDs is $\sim 80\ \mu m^{-2}$ and the QD size is ~25 nm in diameter and ~3.5 nm tall. The shift in the PL peak to a shorter wavelength enhanced QDs is from the indium island resonance being centered at a shorter wavelength and enhancing the shorter wavelength QDs more. The PL measurements are done at a temperature of 10.8 K with above band pumping from a 632.8 nm continuous wave HeNe laser. About 1.6 mW of pump power is focused to a ~3 μm diameter spot, using a high NA 100× microscope objective. Also shown in Fig. 4 is the room temperature resonance of the indium islands, with dimension of 120 nm in diameter and 50 nm tall, as measured using an FTIR spectrometer. The resonance of the indium islands has been checked to not change between room temperature and 10 K but is not shown here.

4. Conclusion

Self-assembled plasmonic nanostructures that can be grown in the same process as III–V quantum emitters have been explored and a wide range in sizes and densities has been demonstrated. A 4× increase in the peak PL of InAs QDs separated by 7 nm from the indium islands has been observed, demonstrating that the islands improve the luminescence of QDs and can in fact interact with them. This distance is less than the observed $1/e$ point, ~8 nm, of the coupling distance previously observed between a plasmonic structure and a QW [12] suggesting this is a useful platform to study coupling effects to III–V near-surface QDs. The increase in PL can be improved further by increasing the percentage of QD emission that is coupled to the plasmon mode [13] of on an indium island by controlling the position of the QDs relative to the plasmonic nanostructures or by using metals with lower losses as the plasmonic nanostructure [2]. An added interest of this platform is the ability to integrate superconducting structures, the indium islands, with III–V quantum emitters. The high indium concentration, up to ~90%, will be beneficial for any superconducting experiments or applications.

Acknowledgments

We gratefully acknowledge the use of facilities with the LeRoy Eyring Center for Solid State Science at Arizona State University. This work was funded by the Air Force Office of Scientific Research (AFOSR, Dr. Gernot Pomrenke, Grant FA9550-13-1-0003), the National Science Foundation Atomic, Molecular and Optical Physics (NSF-AMOP 1205031) and the Engineering Research Center for Integrated Access Networks (NSF ERC-CIAN, Award EEC-0812072). MG would like to acknowledge the support of the Department of Defense through the National Defense Science and Engineering Graduate (NDSEG) Fellowship Program. JS would like to acknowledge the support of Arizona Technology and Research Initiative Funding (TRIF). SZ would like to acknowledge the support of the Department of Energy (DOE) through the Office of Science Graduate Fellowship (SCGF) made possible in part by the American Recovery and Reinvestment Act of 2009, administered by ORISE-ORAU under Contract no. DE-AC05-06OR23100. JH would like to acknowledge support from the Air Force Office of Scientific Research (AFOSR, Program Manager – Dr. Gernot Pomrenke, Contract 12RY05COR). AA would like to acknowledge support from the French technology network RENATECH.

References

[1] Y. Wu, C. Zhang, N.M. Estakhri, Y. Zhao, J. Kim, M. Zhang, X.-X. Liu, G.K. Pribil, A. Alù, C.-K. Shih, X. Li, Intrinsic optical properties and enhanced plasmonic response of epitaxial silver, Adv. Mater. 26 (35) (2014) 6106.
[2] A. Urbańczyk, R. Nötzel, Site-controlled Ag nanocrystals grown by molecular beam epitaxy—towards plasmonic integration technology, J. Appl. Phys. 112 (2012) 124302.
[3] Frank W.M. van Otten Adam Urbańczyk, Richard Nötzel, Self-aligned epitaxial metal-semiconductor hybrid nanostructures for plasmonics, Appl. Phys. Lett. 98 (24) (2011) 243110.
[4] A. Urbaczyk, G.J. Hamhuis, R. Nötzel, Coupling of single InGaAs quantum dots to the plasmon resonance of a metal nanocrystal, Appl. Phys. Lett. 97 (4) (2010) 043105.
[5] L. Novotny, Effective wavelength scaling for optical antennas, Phy. Rev. Lett. 98 (26) (2007) 266802.
[6] M. Gehl, S. Zandbergen, R. Gibson, M. Béchu, N. Nader, J. Hendrickson, J. Sears, P. Keiffer, M Wegener, G. Khitrova, Spectroscopic studies of resonant coupling of silver optical antenna arrays to a near-surface quantum well, J. Opt. 16 (11) (2014) 114016.
[7] N. Meinzer, M. Ruther, S. Linden, C.M. Soukoulis, G. Khitrova, J. Hendrickson, J.D. Olitzky, H.M. Gibbs, M. Wegener., Arrays of Ag split-ring resonators coupled to InGaAs single-quantum-well gain, Opt. Express 18 (23) (2010) 24140.

[8] A.G. Curto, T.H. Taminiau, G. Volpe, M.P. Kreuzer, R. Quidant, N.F. van Hulst., Multipolar radiation of quantum emitters with nanowire optical antennas, Nature Commun. 4 (2013) 1750.
[9] C.R. Haughn, E.H. Steenbergen, L.J. Bissell, E.Y. Chen, K.G. Eyink, J.M.O. Zide, M.F. Doty, Carrier transfer from InAs quantum dots to ErAs metal nanoparticles, Appl. Phys. Lett. 105 (10) (2014) 103108.
[10] I.M. Lifshitz, V.V. Slyozov, The kinetics of precipitation from supersaturated solid solutions, J. Phys. Chem. Solids 19 (1) (1961) 35.
[11] A.I. Ekimov, Optical properties of semiconductor quantum dots in glass matrix, Phys. Scr. 1991 (T39) (1991) 217.
[12] N. Meinzer, M. König, M. Ruther, S. Linden, G. Khitrova, H.M. Gibbs, K. Busch, M. Wegener, Distance-dependence of the coupling between split-ring resonators and single-quantum-well gain, Appl. Phys. Lett. 99 (11) (2011) 111104.
[13] A.V. Akimov, A. Mukherjee, C.L Yu, D.E. Chang, A.S. Zibrov, P.R. Hemmer, H. Park, M.D. Lukin, Generation of single optical plasmons in metallic nanowires coupled to quantum dots, Nature 450 (2007) 402.